Nanoscale Lasers with Optical Microcavities

by

Junseok Heo

A dissertation submitted in partial fulfillment
of the requirements for the degree of
Doctor of Philosophy
(Electrical Engineering)
in The University of Michigan
2011

Doctoral Committee:

Professor Pallab K. Bhattacharya, Chair
Professor L. Jay Guo
Associate Professor Kevin P. Pipe
Assistant Professor Pei-Cheng Ku

© Junseok Heo

2011

To my parents

ACKNOWLEDGEMENTS

First of all, I would like to thank my parents and the rest of my family. I thank them for their love, support and many encouragements during my life.

I would like to express my heartfelt gratitude and appreciation to my advisor Prof. Pallab Bhattacharya for his support, encouragement and guidance throughout my graduate study. I also would like to thank my other committee members, Prof. Lingjie (Jay) Guo, Prof. Kevin Pipe, and Prof. Pei-Cheng Ku for devoting their time to review this dissertation and providing valuable suggestions. Special thanks to Prof. Jian Xu at Pennsylvania State University for valuable discussions and advice.

I would like to thank Dr. Juraj Topolancik, Dr. Swapnajit Chakravarty, and Dr. Jun Yang for their help in getting me acquainted with device fabrication and characterization. I am also thankful to my past and current research group members, Dr. Wei Guo, Dr. Dipankar Saha, Dr. Guan Huang, Dr. Debashish Basu, Dr. Meng Zhang, Chi-Sen Lee, Hyun Kum, Ayan Das, Sishir Bhowmick, Animesh Banerjee, Shafat Jahangir, Saniya Deshpande, Allan Xiao, Marc Jankowski, and Thomas Frost. I would like to extend my gratitude to those graduate students with whom I have not directly collaborated but whose assistance I greatly appreciate. I thank Dr. Geonwook Yoo, Gwang Hyun Baek, Kuk-Hwan Kim, Jinyoung Hwang, Hyungwon Bacc, Hui Joon Park, Jaeyong Lee, Ling Tao, Dr. Min Kim, Dr. Luke Lee, Daeyoung Lee, Seunghyun Oh, Yonghyun Shim, Jeremy Moore, and Siddharth Gaba.

Excellent support from the Lurie nanofabrication facility staff is greatly appreciated. I would like to thank Timothy Brock, Gregory Allion, Brian Armstrong, Russ Clifford, Pilar Herrera-Fierro, Sandrine Martin, Matthew Oonk, Brian VanDerElzen, and Nadine Wang.

I thank Lisa Vogel, Melanie Caughey, Denise Oscar, Laura Jarels, Frances Doman, Deb Swartz, and Beth Stalnaker for administrative support throughout my graduate career. I wish to acknowledge the Samsung Scholarship, the Air Force Office of Scientific Research (AFOSR), the Defense Advanced Research Projects Agency (DARPA), and the National Science Foundation (NSF) for funding this research.

TABLE OF CONTENTS

DEDICATION ii

ACKNOWLEDGEMENTS iii

LIST OF FIGURES viii

LIST OF APPENDICES xv

CHAPTER

I. Introduction 1

1.1. Forward 1
1.2. Optical interconnects 2
1.3. Light emitters with microcavities 3
1.4. Thesis organization 6

II. Coherent Photoluminescence from PbSe Colloidal Quantum Dots in Silicon-Based Photonic Crystal Microcavities 10

2.1. Introduction 10
2.2. Synthesis of PbSe colloidal quantum dots 11
2.3. Design of random photonic crystal microcavity 13
2.4. Fabrication 15
2.5. Device characterization 17
2.5.1. Passive cavity characterization 17
2.5.2. The random photonic crystal microcavity with PbSe QDs 19
2.6. Discussion and conclusion 24

III. 1.5 µm PbSe Colloidal Quantum Dot Coherent Electroluminescent Devices on Silicon 25

3.1. Introduction 25
3.2. Electroluminescence from silicon-based PC microcavities with PbSe QDs 26
3.2.1. Device design 26
3.2.2. Fabrication 31

3.2.3. Device characterization..35
3.3. Coherent and directional electroluminescence from PbSe QDs embedded between DBR and metal mirrors 39
3.3.1. Device heterostructure 39
3.3.2. Fabrication 43
3.3.3. Device characterization..45
3.4. Discussion..48
3.6. Conclusion 50

IV. Monolithically Integrated GaN Nanowire Laser on Silicon......................51

4.1. Introduction..51
4.2. Growth of GaN nanowires...52
4.3. Device design..54
4.4. Fabrication 60
4.5. Device characterization...62
4.6. Conclusion 66

V. GaN Nanowire Polariton Laser 67

5.1. Introduction..67
5.2. Strong coupling...69
5.3. Device design and fabrication..71
5.4. Dispersion of polaritons...73
5.5. Nonlinear optical characteristics...76
5.5. Conclusions..83

VI. Rolled-up Microtube Laser with InAs Quantum Dots 85

6.1. Introduction..85
6.2. Design of free standing rolled-up microtube cavity 87
6.3. Surface passivation of GaAs...89
6.4. Device characterization...90
6.5. Finite difference time domain (FDTD) simulation...........................93
6.6. Theoretical calculation of threshold...95
6.6.1. Bending loss...97
6.6.2. Scattering loss at notches 99
6.6.3. Optical loss through substrate..101
6.6.4. Modal gain and threshold carrier density.................................102
6.7. Conclusion 105

VII. Conclusions and Suggestions for Future Work 106

7.1. Summary of completed work...106
7.1.1. Coherent photoluminescence from PbSe colloidal QDs in silicon-based PC microcavities 106
7.1.2. 1.5 μm PbSe colloidal QD coherent electroluminescent device on silion 107

7.1.3. Monolithically integrated GaN nanowire laser on silicon....107
7.1.4. GaN nanowire polariton laser....108
7.1.5. Rolled-up microtube laser with InAs quantum dots....108
7.2. Suggestions for future work....109
7.2.1. Electrically injected GaN nanowire polariton laser....109
7.2.2. Electrically injected microtube laser....111

APPENDICES....113

BIBLIOGRAPHY....123

LIST OF FIGURES

Figure

1.1 The future silicon processor chip with optical input/output layer featuring on-chip nanophotonic network 2

1.2 Optical mode density of a one-dimensional planar microcavity (solid line) and of homogeneous one-dimensional free space (dotted line) 5

1.3 New polariton dispersions (upper polariton and lower polariton) are formed by the strong coupling between excitons (dashed red) and photons (dashed blue line). Polaritons (green circles) accumulate in the lower polariton branch through stimulated scattering (arrows), before escaping radiatively from the bottom of the lower polariton branch 6

2.1 PbSe colloidal quantum dots are synthesized in a 25 ml three-neck flask equipped with condenser, magnetic stirrer, thermocouple, and heating mantle 11

2.2 Absorbance and photoluminescence of synthesized PbSe colloidal quantum dots with different sizes 12

2.3 The high resolution transmission electron microscopy image of a 6 nm size of PbSe colloidal quantum dot 13

2.4 Schematic representation of the band structure of the traditional (left) and disordered (right) waveguides with Γ-K line-defect. Fluctuations of the stop band edge create wells in which photons of certain energies are confined 14

2.5 Scanning electron micrograph of the fabricated Si-based two-dimensional membrane disordered photonic crystal nanocavity 16

2.6 Calculated dispersion of the defect waveguide in ideal crystal shown in the inset (hollow circles denote odd modes and solid circles denote even modes) 16

2.7 Schematic illustration of passive quality factor measurement setup 17

2.8 (a) Contour plot of the spatially-resolved spectra of a 150 μm-long disordered waveguide; (b) example of a well-localized, high-Q resonance

in the passive random photonic crystal microcavities. The probing and collection directions are indicated in the inset. 18

2.9 Scanning electron microscopy image of a cross section of the photonic crystal showing PbSe quantum dots embedded into photonic crystal microcavities. 20

2.10 Schematic illustration of micro-photoluminescence setup 21

2.11 Emission spectra of a silicon random photonic crystal microcavity with PbSe quantum dots measured at 300K at different pump powers 22

2.12 (a) Light-light characteristics, and (b) emission peak linewidth versus pump powers setup........23

3.1 Schematic of the device heterostructure fabricated on silicon-on-insulator (SOI). PbSe quantum dots with MEH-PPV are clad by PEDOT:PSS on the ITO anode and Alq3/Ca/Al cathode 26

3.2 Energy band diagram of device heterostructure with PbSe quantum dots as a gain medium. 27

3.3 (a) Scanning electron microscopy (SEM) image of the L3 defect photonic crystal (PC) microcavity in silicon. Out air holes at both edges in the defect are shifted by 0.1*a*; (b) SEM image of a cross section of PC microcavity in silicon after ITO deposition. Filling of holes with ITO is negligible 28

3.4 Distribution of the electric field (red line) along the z-direction (vertical direction) calculated by the transfer-matrix method with the refractive index profile shown (blue line). The shaded area corresponds to the overlap of confined electric field in the PC slab with the gain medium........29

3.5 (a) Three dimensional schematic of L3 defect photonic crystal microcavity; (b), (c), and (d) numerically calculated electric field profile (E_z) of the cavity mode in *x-y* plane at the center of a defect (b), *x-z* plane at the interface of ITO and PbSe QD (c), and *x-z* plane at the center of a defect (d). 31

3.6 Flow chart of device fabrication. See appendix A for photonic crystal fabrication 33

3.7 The circular active area is defined by standard optical lithography and a metal lift-off. Photonic crystals are aligned within this area and patterned by electron beam lithography and reactive ion etching. 35

3.8 The measured current-voltage characteristic of the device. A turn-on voltage is around 12 V with a series resistance after a turn-on estimated to be ~86 Ω........36

3.9 Measured room temperature electroluminescence of the control device without a photonic crystal microcavity and a gold blocking layer (a) and the device with a photonic crystal microcavity (b); (b) the resonant mode is clearly observed at λ=1669 nm with a linewidth of ~4 nm 37

3.10 (a) The measured room temperature electroluminescence of the second device, showing a resonant mode at 1571.2 nm with a linewidth of 14.3 nm; (b) measured light-current characteristics of the resonant mode in a second device showing a turn-on current of ~6 mA 38

3.11 (a) Schematic of the device heterostructure fabricated on a silicon substrate. The light emitting region consisting of ITO, PEDOT:PSS, and ZnO, is clad by Ag and the bottom DBR which is made of SiO_2 and amorphous-Si; (b) energy band diagram of the device heterostructure. Electron and hole states of PbSe quantum dots are well aligned with the work functions of ZnO and PEDOT:PSS..40

3.12 Absorption of as-synthesized ZnO nanocrystals showing a shoulder peak around 320 nm (E_g ~ 3.9 eV) 41

3.13 Measured reflectivity spectra of Ag mirror and SiO_2/a-Si DBR. Both mirrors exhibit a high reflectance of ~98 % from 1400 nm to 1700 nm 42

3.14 Numerically calculated electric field intensity (blue line) in the device with refractive index profile (green line). The maximum electric field spatially coincides with a layer of PbSe QDs, which is highlighted.................................43

3.15 A cross-sectional scanning electron microscopy image of the fabricated device. The distributed Bragg mirror consisting of SiO_2 and a-Si is clearly seen 44

3.16 Measured current density-voltage characteristics of the fabricated device on a log-log plot. The increase of the slope at 2.3 V indicates the onset of carrier injection into the QDs. The inset shows *J-V* characteristics in linear scale, which exhibiting a good rectifying behavior 45

3.17 (a) Room temperature electroluminescence spectra from the control sample without a DBR and two devices with different cavity sizes. Resonant modes are tuned by varying the cavity size. The narrowest linewidth is ~3.1 nm at λ=1563.1 nm; (b) angular emission characteristics recorded from the device with a DBR at angles ranging from 0-45 degrees with respect to the cavity axis. The Lambertian pattern is also shown for comparison....................46

3.18 Measured voltage-current density and light-current density characteristics of the device. The integrated light output increases linearly with current. The extrapolation of the linear fit indicates a turn-on voltage of ~2.4 V 48

4.1 (a) and (b) Cross-sectional SEM images of catalyst-free GaN nanowires grown by plasma-assisted MBE with different densities of ~1×10^{11} cm^{-2} on (001) Si (a) and ~1×10^{8} cm^{-2} on (111) Si (b) under the growth conditions described in the text. The vertically aligned GaN nanowires have a length of ~600 nm and a diameter of 20-50 nm 53

4.2 High resolution TEM image of a GaN nanowire with a diameter of 20 nm which exhibits no observable defects. The inset shows the diffraction pattern indicating the nanowire is a single crystal wurtzite structure with the *c*-axis along the direction of growth 54

4.3 Anisotropic band structure in the Wurtzite crystal structure. A smaller density of states in the *x*-direction results in a larger gain near the band edge with the same amount of carrier injection 55

4.4 (a) Two dimensional (2D) photonic crystal slab with air holes; (b) calculated dispersion curves of 2D photonic crystal for TM and TE light 56

4.5 Schematic representation of nanowire laser consisting of a single GaN nanowire and a two dimensional photonic crystal microcavity in the TiO_2 layer (120 nm). Spin-on-glass (380 nm) with a low refractive index (n_r=1.4) helps to reduce optical loss from the microcavity in the TiO_2 layer to the Si substrate 57

4.6 (a) Refractive index profile and calculated electric field by transfer matrix method; (b) the resonant mode of H2 defect (dotted line) and photonic band gap (shaded area); (c) calculated mode profile (E_Z) using 3D FDTD 59

4.7 An oblique view SEM image of the fabricated device. The single GaN nanowire is well-aligned in the center of the H2 defect of the photonic crystal microcavity. Due to the directional nature of TiO_2 evaporation, a small amount of TiO_2 is deposited on top of the GaN nanowire and a partially filled hollow region is created around the nanowire 60

4.8 Flow chart of device fabrication. Refer to Appendix B for photonic crystal fabrication 61

4.9 (a) Photoluminescence of the laser at pump power densities of 95 kW/cm^2 (below threshold), 143 kW/cm^2 (near threshold) and 477 kW/cm^2 (above threshold). Spectra are offset for clarity. The inset shows the lasing spectrum (blue circles), which is matched to the sum of two Gaussian peaks (green and red solid lines); (b) measured linewidth of the spectral output as a function of the pump power density. The spontaneous emission linewidth of 4.5 nm decreases sharply at threshold (~120 kW/cm^2) and attains a value of 1.5 nm above threshold 63

4.10 Calculated resonant modes with the nanowire in the center (black) and off-center by 60 nm (blue). Mode profiles of each case are shown on the right 64

4.11 (a) Variation of peak output intensity with pump power. The change in slope near threshold (~120 kW/cm^2) is clearly observed; (b) log-log plot of spectrally integrated light intensity (red circles) versus pump power density. Theoretically calculated light intensity using the rate equations is also shown for spontaneous emission factors (β) of 0.02, 0.08, and 0.15 65

5.1 Anticrossing of lower and upper polariton energy levels when tuning the cavity energy across the exciton energy 70

5.2 (a) Schematic representation of the dielectric microcavity with a single GaN nanowire of diameter 60 nm (inset) buried in the center of a λ-sized cavity; (b) photoluminescence spectrum from a single GaN nanowire measured at 25K showing free and bound exciton transitions 72

5.3 (a) Angle-resolved photoluminescence measured at room temperature; (b) polariton dispersion curves obtained from the data of (a). The solid curves indicate the calculated polariton dispersion from a coupled harmonic oscillator model...74

5.4 The calculated electric field intensity distribution of the fundamental resonance mode around the nanowire embedded in a 5 μm diameter pillar cavity. Cross-sectional profiles of the electrical field intensity along the *x*, *y* and *z* directions. The *y* direction is defined to be along the length of the nanowire. The *z* direction is in the cavity growth direction. The origin is at the center of the nanowire...76

5.5 (a) Measured polariton emission intensity at 200K as a function of incident optical excitation energy showing strong non-linearity at threshold. The inset shows the emission spectra; (b) variation of the emission linewidth and peak energy corresponding to the data in (a); (c) variation of the emission intensity with excitation energy at 300K clearly showing the two thresholds for polariton and photon lasing. The insets show the corresponding emission spectra; (d) variation of linewidth and emission energy at 300K for polariton lasing 77

5.6 (a) Photoluminescence spectra measured from the second device as a function of incident pump density at zero detection angle at 80 K; (b) corresponding variation of integrated emission intensity; (c) linewidth and blueshift with incident pump density. A threshold is observed at 63 nJ/cm^2 and a minimum full-width half maximum linewidth of 0.97 meV is measured, corresponding to a coherence time of 4.8 ps 79

5.7 Angle resolved lower polariton luminescence spectra measured at 300K (a) below and (b) above the polariton lasing threshold..82

5.8 Polariton occupancy for different $k_{||}$ states deduced from the data of Fig. 6.6 ...83

6.1 (a) and (b) Illustrations of the formation of InGaAs/GaAs microtube structures on GaAs; (c) Optical microscopy image of an InGaAs/GaAs microtube formed on GaAs 86

6.2 (a) Device heterostructure. InAs quantum dots are buried in a GaAs matrix grown on an InGaAs strained layer and AlAs sacrificial layer; (b) and (c) illustration of the formation of free-standing quantum dot microtubes on GaAs substrates 88

6.3 The photoluminescence intensity comparison between thin GaAs with and without surface passivation using an ammonium sulfide solution 89

6.4 The microscopy image of the fabricated device. The tube is separated from the GaAs substrate by 400 nm 90

6.5 (a) Room temperature photoluminescence spectrum of as-grown sample showing broad emission; (b) emission spectrum of microtube with a radius of ~3 μm and a wall thickness of ~100 nm exhibits multiple resonance peaks. The narrowest linewidth is ~1.5 nm, corresponding to a cavity quality factor of ~800 91

6.6 Measured light-light characteristics of microtube device showing a threshold at ~700 kW/cm^2 93

6.7 (a) Schematic representation of a spiral microtube structure. TM mode with an electric field parallel to the wall and a magnetic field normal to the wall is shown; (b) Distribution of the optical resonance modes simulated by FDTD method for microtube ring resonator with a diameter of 5 μm. Strong emission from the inside notch can be clearly observed 94

6.8 (a) Schematic representation of a microtube cavity; (b) the front view of a microtube cavity. A microtube cavity is approximated to a ring resonator with two different thicknesses of walls and two notches 96

6.9 A geometry of a curved waveguide representing a wall of a microcavity 97

6.10 Deviation of a propagation constant in a curved waveguide. β and β_0 represent a propagation constant in a curved waveguide and a straight waveguide, respectively 98

6.11 The radius dependent bending loss for different wall thicknesses. The bending loss shows an exponential dependence on the radius 99

6.12 (a) Schematic representation of inside and outside notches along the microtube; (b) schematic representation of an equivalent waveguide with a step discontinuity. The input guided mode at the step discontinuity partially changes to an output guided mode and the rest of them is scattered in forward and backward directions 100

6.13 Calculated scattering loss at notches when the light travels from 100 nm thick waveguide to a thicker waveguide (black) and from 150 nm thick waveguide to a thinner waveguide (red) 101

6.14 (a) Variation of calculated cavity quality factors in a ring resonator. The wall thickness is 100 nm; (b) calculated substrate loss from a Q-factor 102

6.15 (a) The bending loss and the scattering loss by varying the radius curvature. The scattering loss is a dominant loss, which determines the threshold gain; (b) the radius curvature dependent threshold gain of a microtube. It is noted that the modal gain is inversely proportional to the radius of the microtube ...103

6.16 The maximum gain versus the carrier density with the Gaussian density of state broadening due to the quantum dot size fluctuation................................104

7.1 (a) SEM image of a fabricated single GaN device with contacts; (b) current-voltage characteristic of device with a turn on voltage of ~15 V; (c) measured electroluminescence at an injection current of 4μA 110

7.2 Schematic of an electrically injected single GaN nanowire polariton laser before (a) and after (b) the deposition of top DBR..111

7.3 Schematic representation to fabricate an electrically operated rolled-up microtube. (a) ion implantation to dope only one side; (b) the microtube device after rolled-up 112

LIST OF APPENDICES

Appendix

A. Purcell factor 114

B. Fabrication of photonic crystals 117

C. Wannier-Mott exciton 121

Chapter I

Introduction

1.1 Forward

Future computing and communication systems require small weight, volume, and power dissipation, which necessitates a combination of both electronic and photonic components; electronic elements are needed for processing and control applications while photonic devices are needed for transmission and sensing. This need has fueled continued interest in the integration of electronic circuits and optoelectronic passive and active components.

For hybrid integration, silicon (Si) appears to be a convenient substrate material on which to grow silica waveguides for integrated optics, and the advanced fabrication technology is available with low cost. However, Si is an indirect bandgap material, which inherently does not emit light at useful wavelengths. This imposes more urgency and significance on developing a nanoscale coherent light source that can be integrated on Si.

Such a nanoscale coherent light source is crucial for applications such as analog and digital optical communication links as well as optical interconnects [1, 2] in complementary metal oxide semiconductor (CMOS) electronic circuits, which would eliminate crosstalk and RC signal delays and enable high-speed data transfer across a chip. Likewise, an integrated laser is necessary for "lab on a chip" technologies that rely on the monitoring of an optical signal as the basis for detection of bio-warfare agents and

other chemical and biochemical species. For example, a nanoscale laser integrated on a chip can detect cancer in single cells by noticing the difference in light scattered by the mitochondria of malignant cells [3].

1.2 Optical interconnects

Since the 1980s optical communication links have replaced electrical wires due to their ability to deliver higher data rates over longer distances. The initial impetus was the increased bandwidth requirements of interactive multimedia services, which strained the capacity of traditional wired networks. Since then, optical signals have gradually penetrated into home networks, personal computers, and consumer electronics, represented by FTTH (Fiber-to-the-Home) services and S/PDIF (Sony/Philips Digital Interconnect Format) digital audio format.

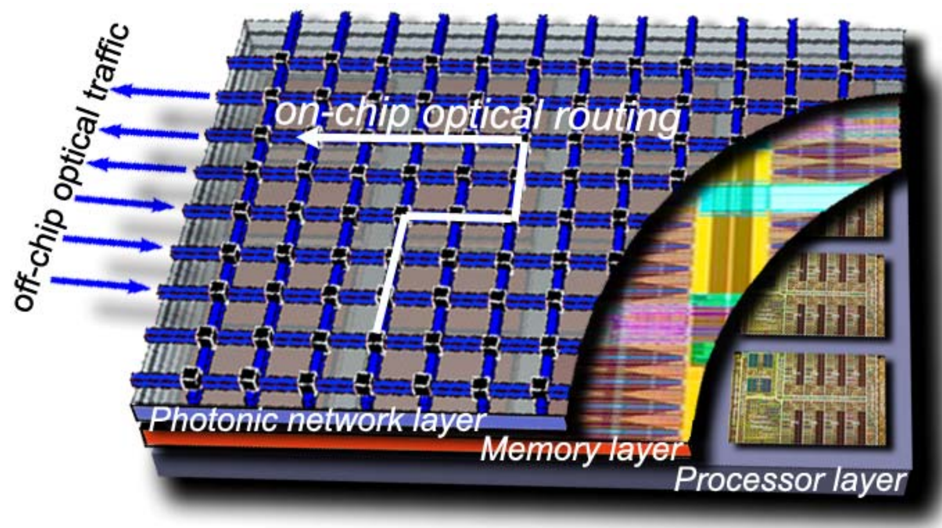

Figure 1.1 The future silicon processor chip with optical input/output layer featuring on-chip nanophotonic network (adapted from [4]).

Recently, as a consequence of device miniaturization, metal interconnections approached the limitation in integrated circuits (IC) and have become a major bottleneck to the overall performance. According to the 2010 ITRS (International Technology Roadmap for Semiconductors) report, the input/output data rates are expected to be 65 Gb/s by 2020, for which optical modulation are the only solution to achieve this bandwidth. In this context, optical interconnects are being actively investigated as a potential solution to address the limitations of electrical interconnects. For example, an IBM research center proposed a future 3D-integrated chip consisting of several layers as illustrated in Fig. 1.1. In this device, the photonic layer is responsible for providing point-to-point broad bandwidth optical links between different cores and off-chip traffic.

An essential component for optical interconnects is the optical source with high performance and low cost. Semiconductor lasers and light emitting diodes (LEDs) are deemed to be highly desirable sources by virtue of their compactness and amenability to integration into dense arrays. Since optical interconnects have been used in long distanced networks such as wide area networks (WAN, ~100 km), local area networks (LAN, ~1 km), and storage area networks (SAN, ~100 m), performance and cost requirements are the main concerns. However, as optical interconnects are being investigated as a viable technology for on-chip and off-chip interconnects, scaling, power consumption, and the ability to be integrated on Si become primary issues.

1.3 Light emitters with microcavities

A coherent light source generally consists of a gain medium and an optical cavity to provide a feedback. Due to advanced growth techniques, very small size of gain

medium such as quantum wells, quantum wires, and quantum dots have been explored and steady improvements have been made. Therefore, in order to reduce overall size of the light source and improve the photonic device performance, microcavities, where cavity size is on the order of the wavelength in the material, are indispensable. Microcavities have attracted attention due to several reasons; the possibility of ultra-small laser with low power consumption, potential of thresholdless lasing operation owing to the high efficiency coupling of spontaneous emission into a single lasing mode, and polariton lasing resulting from stimulated scattering of polaritons. Devices based on optical microcavities are already indispensable for a wide range of applications. For example, microcavities made of active III-V semiconductor materials control the laser emission spectra to enable long-distance transmission of data; they also ensure narrow spot-size laser read/write beams in compact disk (CD) and digital versatile disk (DVD) players.

The confinement of light to small volumes has important consequences on the properties of optical emission. The density of optical modes within a microcavity is strongly modified as compared to the mode density in free space surrounding the cavity. As shown in Fig. 1.2, optical mode density which is constant for all energy values in free space is significantly transformed. The cavity allows for the propagation of optical waves only at the fundamental resonance mode and its harmonics along the optical axis of the Fabry-Pérot microcavity. Photons can only be emitted from emitters, which match the photon modes in well determined directions and polarizations. Modes other than the fundamental resonance and its harmonics are not supported by the cavity, and such modes are inhibited. Theoretically, the alteration of the emission rate is usually treated

within the framework of Fermi's golden rule in which the emission rate is proportional to the product of the mode density and the matrix element of the atom-field interaction (see Appendix A. Purcell effect). This unique property of confined systems can lead to the reduction in size and power requirement of integrated optical components, to single-mode operation of light emitting devices, to the reduction of lasing threshold in semiconductor lasers, and to higher modulation speeds.

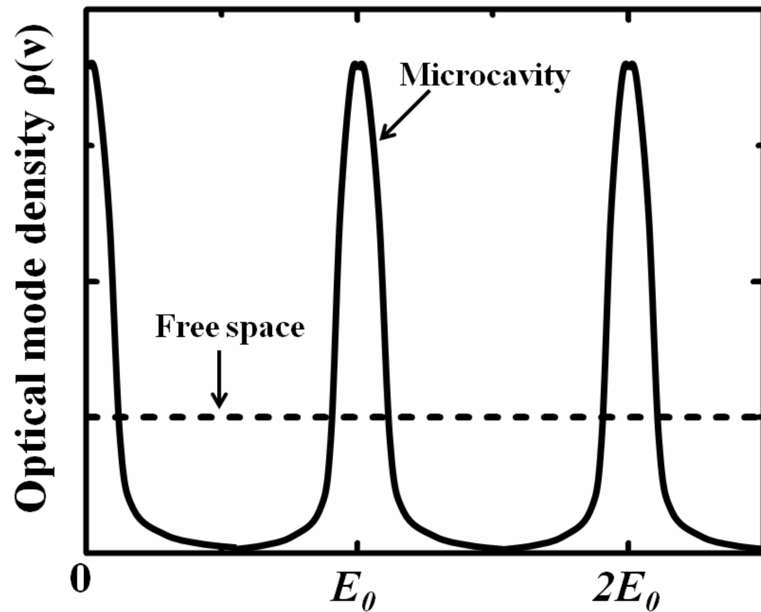

Figure 1.2 Optical mode density of a one-dimensional planar microcavity (solid line) and of homogeneous one-dimensional free space (dotted line).

Under special circumstances, an emitter embedded in a high quality factor microcavity can provide extremely low threshold lasing. When the gain medium is placed at the antinodes of the resonant field of a microcavity, excitons strongly interact with the confined optical field of the cavity. If the rate of energy exchange between the cavity field and excitons becomes much faster than the decay and decoherence rates of both the cavity photons and the excitons, which is called strong coupling, an excitation in the

system is stored in the combined system of photons and excitons. Thus, the elementary excitations of the system are no longer excitons or photons but a new type of quasiparticle called *polaritons*. Hence, the dispersion curves of photons and excitons transform into new dispersion curves of two polariton branches (upper polariton and lower polariton) as shown in Fig. 1.3. Since polaritons are bosons, the extremely low threshold lasing can result from stimulated scattering and accumulation of a quantum degenerate polariton population near the band minimum.

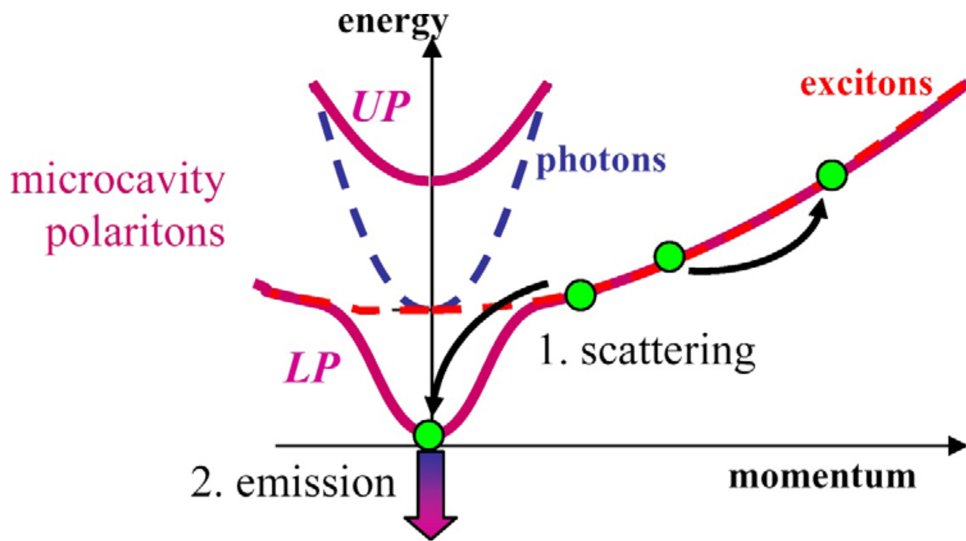

Figure 1.3 New polariton dispersions (upper polariton and lower polariton) are formed by the strong coupling between excitons (dashed red) and photons (dashed blue line). Polaritons (green circles) accumulate in the lower polariton branch through stimulated scattering (arrows), before escaping radiatively from the bottom of the lower polariton branch (adapted from [5]).

1.4 Thesis organization

The purpose of this dissertation research was to explore different nanoscale light sources with low threshold, which also can be integrated with silicon technology for future low-power optical interconnects and other application such as medical diagnosis.

Here, nanoscale lasers are defined by a confined modal volume less than a cubic wavelength in free space, which can be effectively integrated with small electronic circuits. In order to meet the requirements of a nanoscale laser, tremendous efforts have been invested into realizing a variety of microcavities, such as micropillar cavities [6], microdisks [7], photonic crystal nanocavities [8, 9], nanowire Fabry-Pérot cavities [10], and microtubes cavities [11]. In this context, different approaches to implement nanoscale lasers have been studied and demonstrated.

In chapter 2, optically injected silicon based light sources using colloidal PbSe quantum dots embedded in random photonic crystal (PC) microcavities have been investigated. These chemically synthesized colloidal quantum dots (QDs) are a promising candidate for optical interconnects and are compatible with silicon CMOS technology. By imposing shape disorder on periodic photonic crystals, extended modes propagating at the mode-edge becomes spatially confined in sections of the disordered waveguide and a self-optimized high quality microcavity is achieved. For a more compact and versatile device, electrical injection is preferred. Silicon-based electroluminescent devices with PbSe QDs embedded in PC microcavities and with distributed Bragg mirrors (DBRs) are demonstrated and described in chapter 3. QDs are immersed in a conjugated polymer matrix with suitable charge transport layers to realize electrical injection. Enhanced spontaneous emission at room temperature is demonstrated by coupling QDs to silicon photonic crystal (PC) microcavities. The oleate ligand coating PbSe QDs functions as a barrier to impede the carrier transport between QDs and the host matrix. To address this problem, chemical treatment on PbSe QDs was utilized. Electroluminescence from the

PbSe QDs sandwiched between a highly reflective DBR and a metal mirror exhibits coherent and directional light emission at ~1.5 μm.

In chapter 4, monolithically integrated GaN nanowire lasers on silicon are described. GaN nanowires have attracted the attention of many researchers in developing nanoscale lasers due to their large gain and defect free nanoscale dimensions. Although a nanowire needs to be long to be used as a Fabry-Perot cavity, a single nanowire combined with a PC microcavity has subwavelength modal volume without any restriction on the length. A clear lasing behavior was observed at room temperature and a pump threshold was estimated to be 120 kW/cm^2.

In chapter 5, ultra-low threshold polariton lasing from a single GaN nanowire embedded in dielectric DBR mirrors is described. While normal lasers require the population inversion condition, the lasing threshold of a polariton laser requires the Bose condensation to take place by quasithermal equilibrium. Because of this polariton lasers are being favored as a promising device to realize zero threshold lasing. In this device, the threshold carrier density was three orders of magnitude lower than that of photon-lasing observed in the same device, and two orders of magnitude lower than any existing room-temperature polariton devices.

In chapter 6, strain-driven rolled up microtube cavities with InAs QDs are presented. Rolled up microtubes have atomically smooth surfaces providing a high quality (Q) factor. It also has a near perfect overlap between the maximum optical field intensity and the QD layers, which ensures low lasing threshold. Theoretical study of modal gain in a microtube cavity reveals that modal gain is inversely proportional to the radius of the microtube.

Conclusions and suggestions for future work are outlined in Chapter 7.

Chapter II

Coherent Photoluminescence from PbSe Colloidal Quantum Dots in Silicon-Based Random Photonic Crystal Microcavities

2.1 Introduction

There have been a host of attempts to extract light from silicon, and to demonstrate lasing with radiative host materials embedded within or deposited on top of silicon. Nanostructured silicon emitters with various degrees of quantum confinement have also been investigated for light emission, with limited success [12, 13]. The two essential requirements for coherent emission are a gain medium with a high quantum efficiency and a resonant cavity with a high quality factor. A promising approach is to use chemically synthesized nanocrystals, such as Pb(S, Se) and CdSe colloidal quantum dots (QDs) as gain media, embedded in a high-Q silicon-based microcavity. Enhanced luminescence has been demonstrated with Pb(S, Se) QDs embedded in Si photonic crystal (PC) cavities [14, 15].

The colloidal QDs, which exhibit size-tunable luminescence with high efficiency (> 80%) in the near-infrared (IR) range, represent a technologically interesting choice of gain medium for potential applications in silicon photonics [16, 17]. In this chapter, the experimental observation of enhanced photoluminescence from PbSe QDs embedded in silicon *random* PC microcavities is presented.

2.2 Synthesis of PbSe colloidal quantum dots.

PbSe QDs were synthesized using a noncoordinating solvent technique [16, 17]. The synthesis procedure starts with the preparation of a solution of PbO and oleic acid and the subsequent heating of the solution up to an elevated temperature of 160 °C. Rapid injection of selenium-trioctylphosphine reagents into the hot solution induces the nucleation of PbSe and subsequently cooling down the reaction temperature to 135 °C allows the nuclei to grow into highly crystalline nanoparticles.

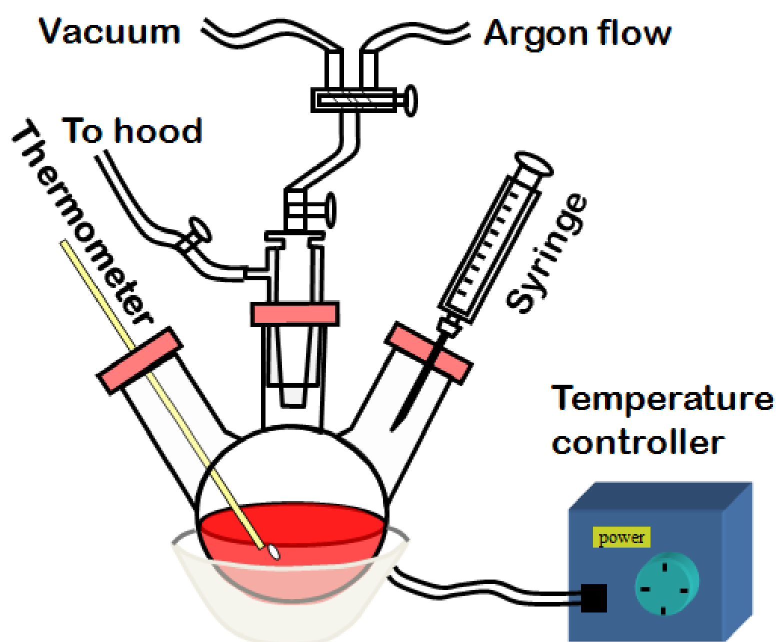

Figure 2.1 PbSe colloidal quantum dots are synthesized in a 25 ml three-neck flask equipped with condenser, magnetic stirrer, thermocouple, and heating mantle.

The size of PbSe quantum dots can be tailored by carefully controlling the growth conditions. The QD growth was monitored using visible/near infrared absorption spectroscopy in order to reach the desired particle size. Under favorable conditions of temperature, injection, and growth time, highly monodisperse PbSe quantum dots can be

produced without any further size-selective precipitation process. The resulting PbSe colloidal QDs were stabilized with a capping layer of oleate molecules coordinated to the Pb atoms. The size of the QDs was tunable by varying the growth time and 6 nm size of PbSe QDs were chosen for the emission wavelength of ~1.55 μm. After the purification process, PbSe QDs were stored in chloroform for the device fabrication.

The interband absorption and photoluminescence (PL) spectra of the synthesized PbSe QDs of three different sizes (5.1nm, 6.0nm, and 7.8nm) are plotted in Fig. 2.2. Sharp excitonic absorption features are discernable up to the second or the third order. The lowest energy excitons are peaked at 1280, 1510, and 2000 nm, respectively. Room-temperature PLs from the PbSe QDs are strong and exhibit small Stokes shifts (≤ 50 nm), indicative of the dominant band-edge emissions. The full-width-at-half-maximum (FWHM) bandwidth of the PL emission of QDs is typically less than 160 nm.

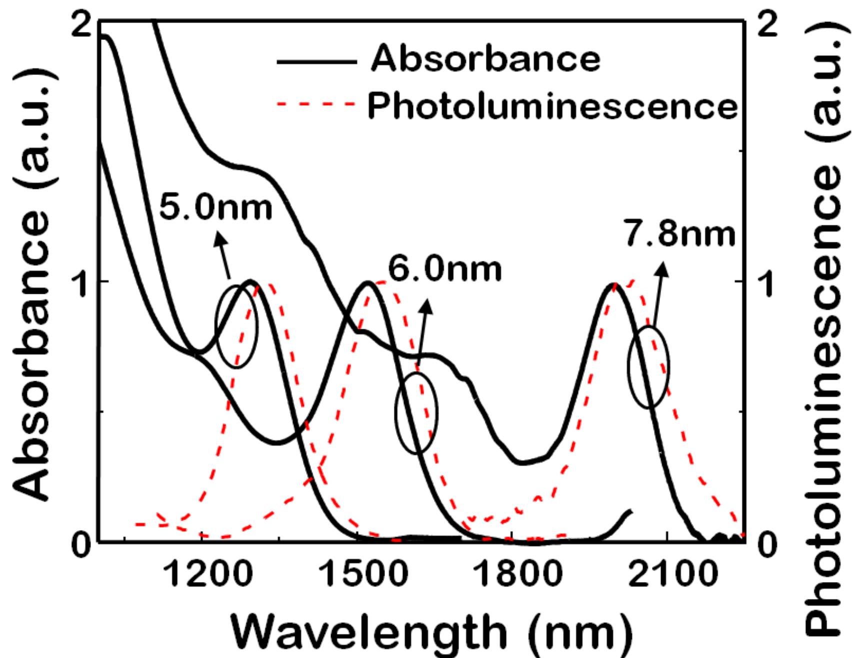

Figure 2.2 Absorbance and photoluminescence of synthesized PbSe colloidal quantum dots with different sizes.

A high-resolution transmission electron micrograph of a 6nm-PbSe nanocrystal is shown in Fig. 2.3. The well resolved regular lattice fringes indicate the single crystalline-domain in PbSe nanoparticles without detectable stacking fault and other internal defects.

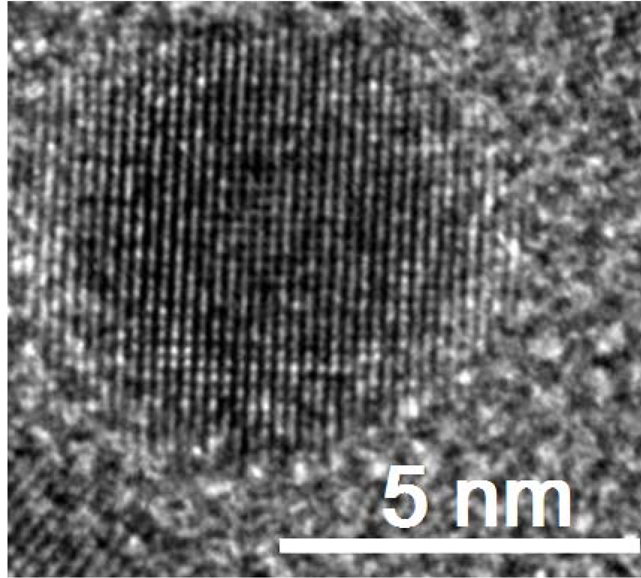

Figure 2.3 The high resolution transmission electron microscopy image of a 6 nm size of PbSe colloidal quantum dot.

2.3 Design of random photonic crystal microcavity

Photonic crystals are periodic dielectric structures, usually two-dimensional (2D) arrays of air-holes in high-refractive-index membranes, that selectively inhibit light propagation in certain bands of frequencies [18]. Destroying the periodicity of the lattice introduces small defects which act as optical cavities with high Qs wherein light can be localized by total internal and Bragg reflections. Q-factors of the order of 10^6 have been measured in engineered microcavities in 2D PCs [19]. On the other hand, Topolancik *et al.* have investigated and reported a different approach to photon localization in PCs, which relies on random structural perturbations introduced uniformly throughout the

crystal by deliberately changing the shapes and orientations of the lattice elements (air holes) [20] as shown in Fig. 2.4.

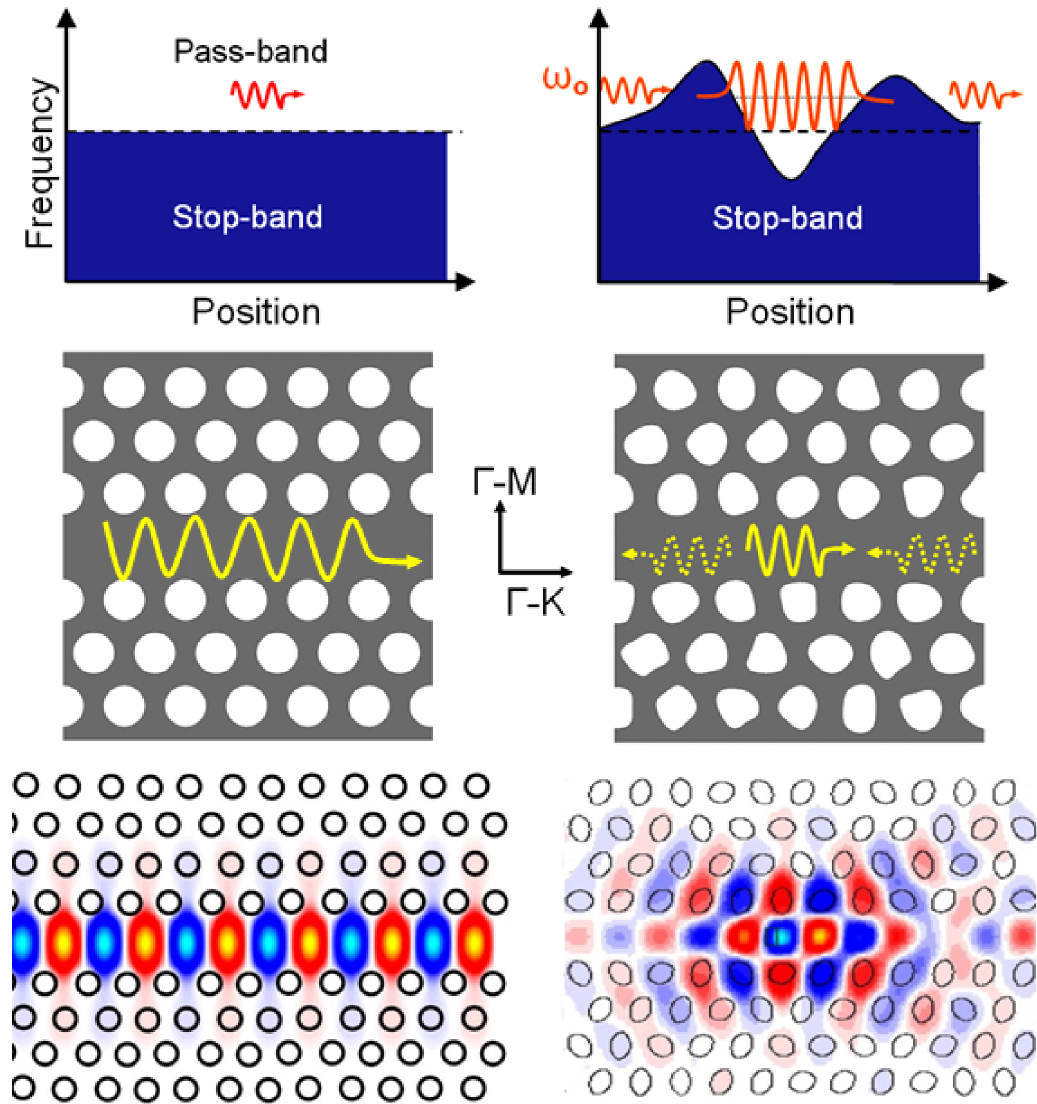

Figure 2.4 Schematic representation of the band structure of the traditional (left) and disordered (right) waveguides with Γ-K line-defect. Fluctuations of the stop band edge create wells in which photons of certain energies are confined.

By replacing circular patterns with random shapes which have the same cross-sectional area as the original circles, the underlying periodicity of the lattice is preserved and there are no point defects of scales larger than the lattice constant. This effectively

creates fluctuations of the stop-band boundary represented by peaks and troughs around the original modes edge. Hence, such random disorder superimposed onto the crystal causes backscattering which impedes propagation of Bloch-waves along line-defects defined in the 2D lattice. Extended modes that propagate with a low-group-velocity at frequencies approaching the mode-edge become spatially confined in sections of the disordered waveguide. This subtle interplay of order and disorder was predicted to give rise to Anderson localization in disordered lattices [21]. Incorporation of suitable gain media into these structures could enable self-optimized lasing from random nanocavities operating around the guided mode's cutoff — similar to what has been observed at the photonic band-edge in *crescent*-deviation disordered PCs [22]. It is worth noting that disordered waveguide structures could support self-optimized nanocavity lasers with significantly smaller modal volumes and lower thresholds than the large-area, disordered PC band-edge lasers [22].

2.4 Fabrication

The fabrication of the devices uses a simple scheme of incorporating colloidal PbSe QDs into the random PC microcavities. The disordered PCs were fabricated on silicon-on-insulator substrates using standard electron-beam lithography and reactive ion etching (see Appendix B. fabrication of photonic crystals). A line-defect waveguide is formed by equally spaced circular holes defined in a hexagonal lattice of randomly rotated squares. The top image of the fabricated structure is shown in the scanning electron micrograph (SEM) in Fig. 2.5. The thickness of the silicon slab (h=220 nm), the radius of the defect holes (r=105 nm), and the lattice constant (a=470 nm) and the fill

factor (~30%) of the bulk PC were chosen so that the cutoff of the guided mode aligns spectrally with the PL peak of colloidal PbSe QDs at 1510 nm.

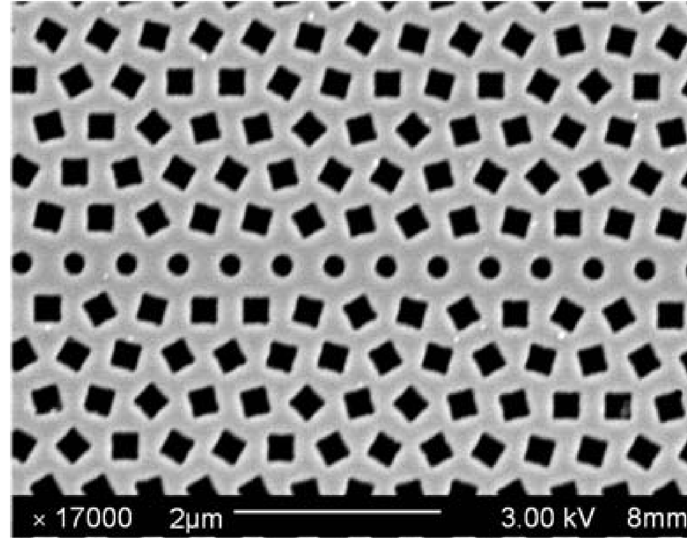

Figure 2.5 Scanning electron micrograph of the fabricated Si-based two-dimensional membrane disordered photonic crystal nanocavity.

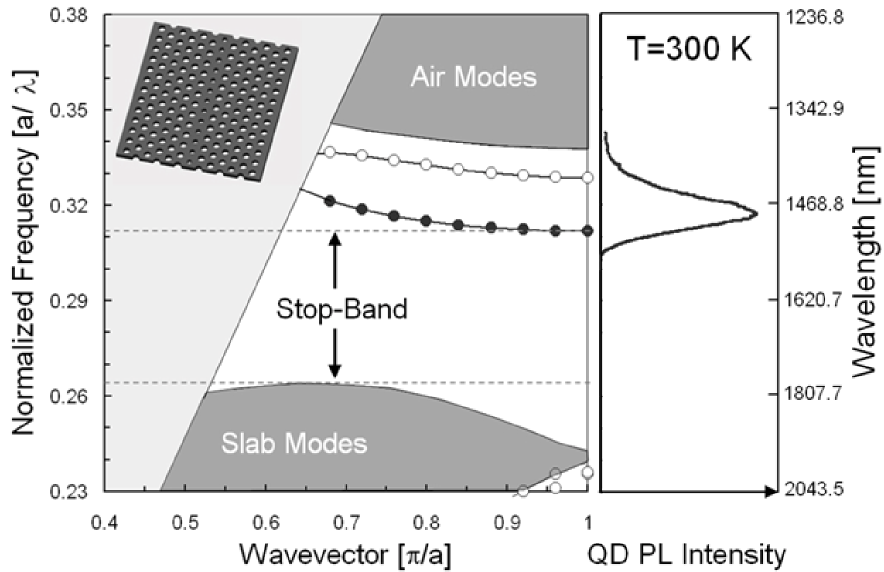

Figure 2.6 Calculated dispersion of the defect waveguide in ideal crystal shown in the inset (hollow circles denote odd modes and solid circles denote even modes).

The dispersion of the waveguide in the underlying periodic crystal calculated by plane-wave expansion method and the room temperature PL spectrum of the dots are shown in Fig. 2.6. The superimposed random scatterers which trigger mode-edge localization can be viewed as the difference between circles in the underlying (ideal) crystal and randomly oriented squares in the disordered photonic crystal.

2.5 Device characterization

2.5.1 Passive cavity characterization

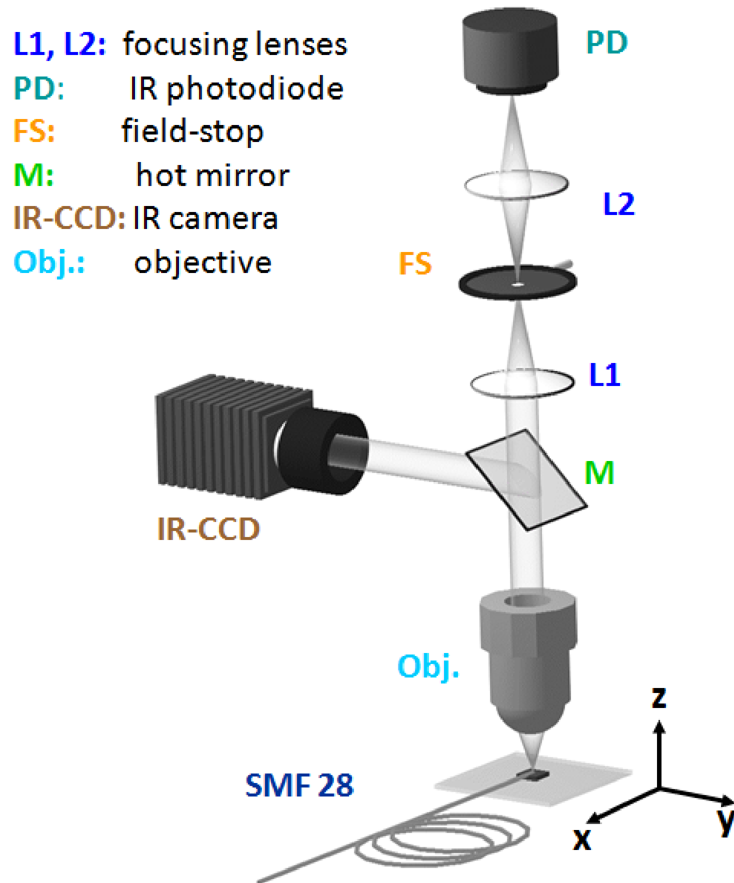

Figure 2.7 Schematic illustration of passive quality factor measurement setup.

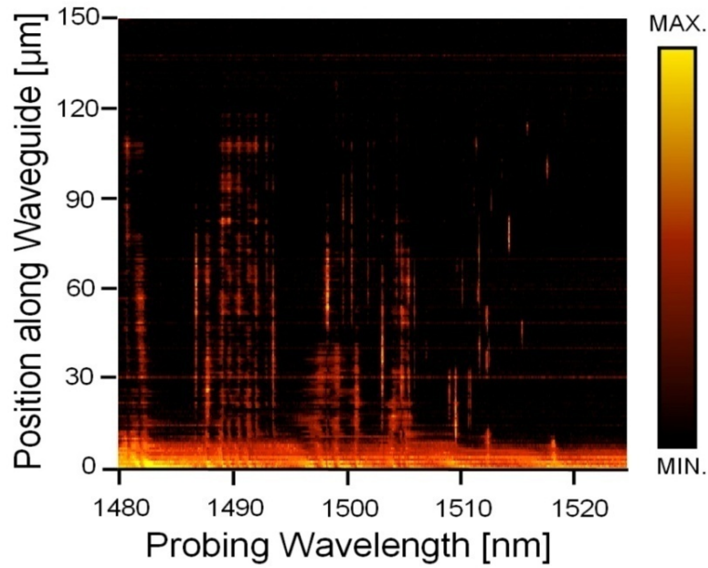

(a)

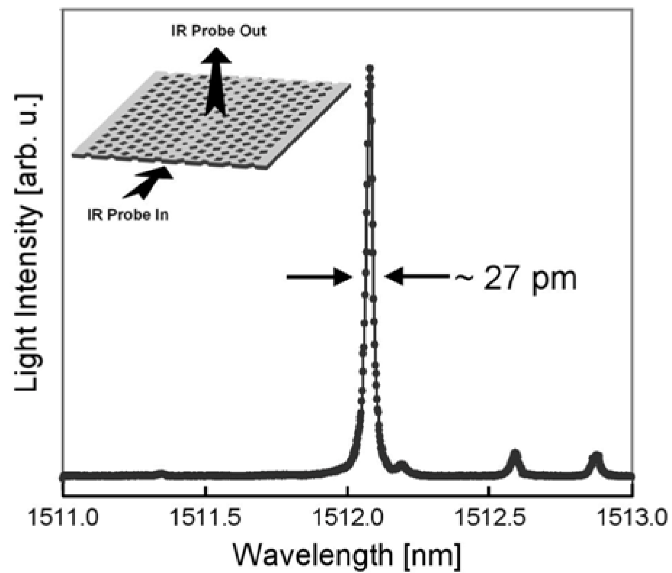

(b)

Figure 2.8 (a) Contour plot of the spatially-resolved spectra of a 150 μm-long disordered waveguide; (b) example of a well-localized, high-Q resonance in the passive random photonic crystal microcavities. The probing and collection directions are indicated in the inset.

The width of the localization band and the positions of random resonators before QD deposition were measured with a 1475-1580 nm broadly-tunable laser source which

was coupled laterally into the waveguide. As shown in Fig. 2.7, the vertically scattered light emitted from random cavities was collected with a high-resolution objective lens and recorded with either a photodiode to obtain vertically-scattered spectra from small sections of the waveguide or with an infrared (IR) camera to obtain 2D spatially resolved spectra.

Figure 2.8(a) recorded by IR camera shows an approximately 40 nm-broad band filled with confined fields with various localization lengths. Note that these are random patterns, i.e. every device has a unique spectral signature and both Q-factor and localization position may vary across the pattern and from pattern to pattern. Figure 2.8(b) shows a resolved projected spectrum collected from a 5 μm-long section of the disordered PC waveguide. The spectrum exhibits a high Q (~ 55,000) resonance near 1512 nm. Such randomly-distributed and localized high-Q resonances are typical for random cavities based on multiple scattering feedbacks [23, 24], which will be reflected in the following characterization of active devices as well.

2.5.2 The random photonic crystal microcavity with PbSe QDs

To characterize active devices, colloidal PbSe quantum dots were embedded in the nanoscale air-holes comprising the line defects in disordered PCs. To maximize the density of QDs coupling with the microcavities, the samples were soaked in the PbSe QD solution for several hours. The SEM image in Fig. 2.9 shows a cross-section of the PCs embedded with PbSe quantum dots.

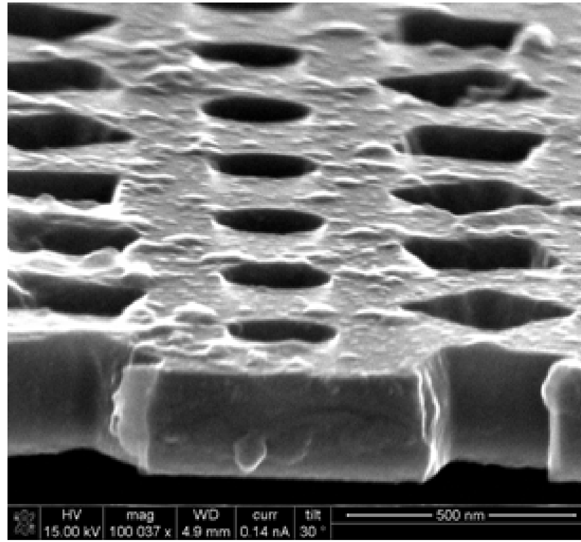

Figure 2.9 Scanning electron microscopy image of a cross section of the photonic crystal showing PbSe quantum dots embedded into photonic crystal microcavities.

The devices were optically excited at room temperature with a continuous wave (CW) Ti:sapphire laser operating at 810 nm. Emission from the QDs in the microcavities was focused by a high-resolution 100× objective lens with an effective focus length f=2 mm and a numerical aperture of 0.7. The diffraction-limited size of the focus spot of the pump beam (λ=810 nm and ~3.5mm aperture or beam size) is ~ 1μm. The localized modes have the minimum localization lengths of few lattice constants. The small focal spot allows us to efficiently pump these highly-localized modes. It should also be mentioned that the disordered structure supports multiple spatially overlapping modes of various localization lengths (modal volumes) at most probing frequencies (wavelengths). This can be seen clearly in the 2D contour map in Fig. 2.8(a) which shows randomly-distributed (hot spots) revealing positions of the localization regions. It means that, in the active structure, multiple modes are likely to be excited. The output spectrum was analyzed with a 0.75 m high-resolution monochromator and detected with an InGaAs

photomultiplier tube using phase lock-in amplification. The pump light is blocked by a bandpass filter placed in front of the monochromator. Unlike emission from the conventional, engineered PC microcavities the exact position of which is known, the output spectral characteristics for the random microcavities are sensitive to the location of the excitation. The disordered waveguides were probed systematically by scanning the focused pump-beam along the waveguide axis (x) as shown schematically in Fig. 2.10.

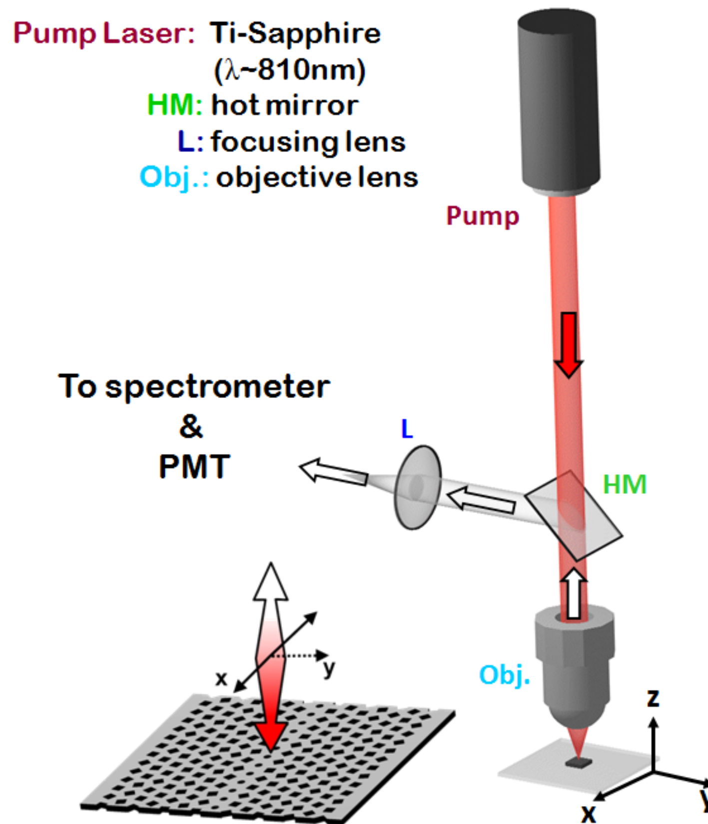

Figure 2.10 Schematic illustration of micro-photoluminescence setup.

A strong dependence of the excited modes' spectral characteristics on the excitation position was observed. Figure 2.11 shows a typical emission spectrum collected from a single excitation spot for varying excitation intensities. At lower pump

intensity, the spectrum exhibits a broad spontaneous emission. Once the pump intensity exceeds a certain threshold, a much narrower emission peak emerges (~4 nm linewidth). It is possible that multiple random resonances are being excited according to the non-Lorentzian line-shape of emission peak. There is a visible shoulder to the peak, and hence the linewidth of the emission peak is estimated by fitting the main peak without the shoulder. The plot of the peak emission intensity versus the pump intensity (L-L), shown in Fig. 2.12(a), exhibits a soft threshold at ~100 μW. Figure 2.12(b) depicts the measured narrowing of the emission linewidth above the pump threshold. The data shown in Figs. 2.11 and 2.12 do not indicate lasing, but suggest the onset of enhanced spontaneous emission coupled into localized modes as a result of strong feedback from random PC microcavities. Such feedback enables photon intensity around the resonance peak to quickly build up over that of the background luminescence.

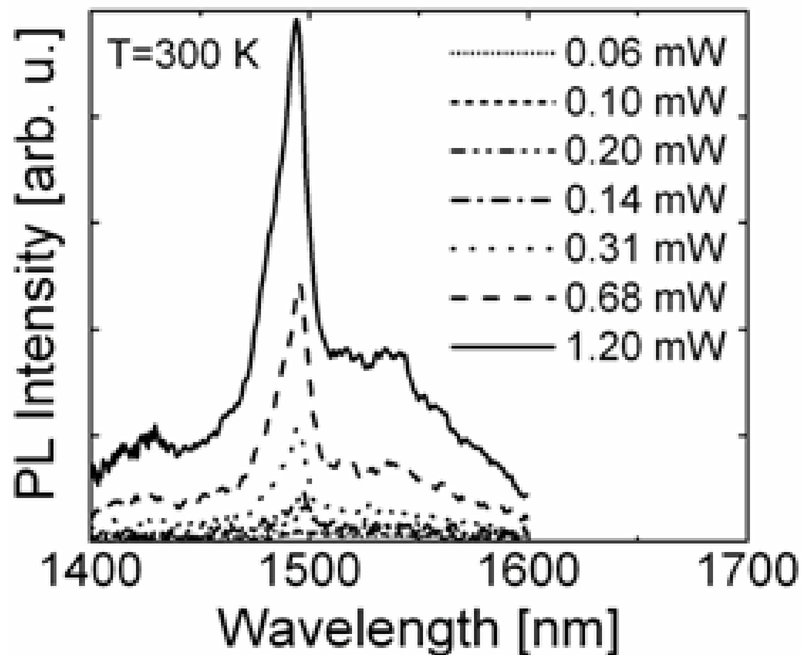

Figure 2.11 Emission spectra of a silicon random photonic crystal microcavity with PbSe quantum dots measured at 300K at different pump powers.

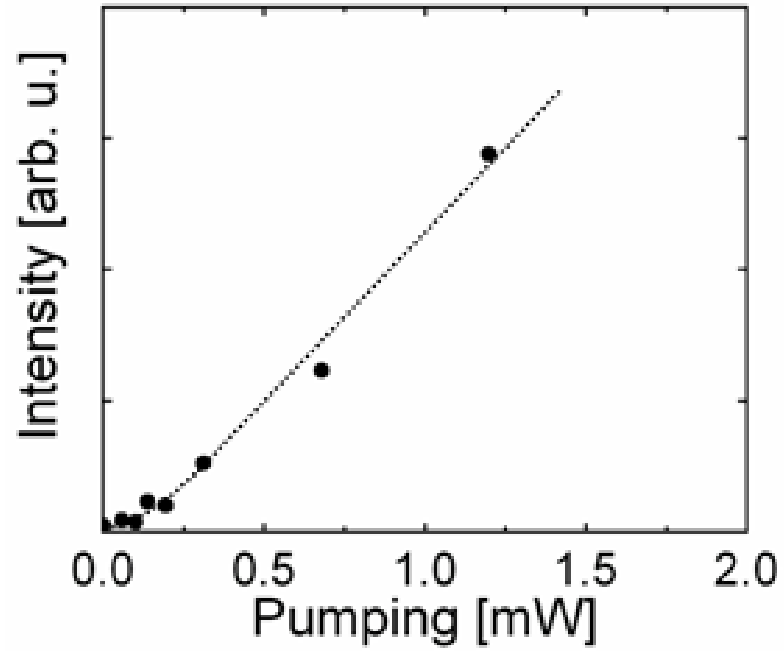

(a)

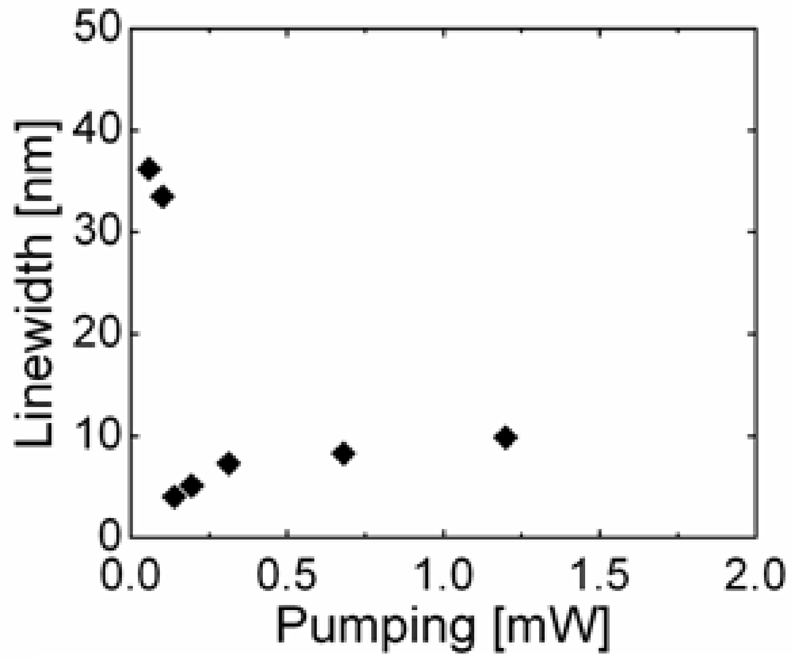

(b)

Figure 2.12 (a) Light-light characteristics, and (b) emission peak linewidth versus pump powers setup.

2.6 Discussion and conclusion

The observation of lasing could be prevented by the low fill factor of the QDs in the microcavity and the resulting low modal gain in our experiment. In order to increase the QD density, novel techniques have been suggested such as spin coating of a nanoparticle/polymer composite and evaporation-induced nanoparticles/polymer self-assembly [25]. Another important issue is the luminescence efficiency of the colloidal PbSe dots. It is observed that the efficiency is reduced, possibly due to surface contamination and oxidation, when the QDs are dried on the silicon PC microcavities. The luminescence efficiency is the highest in a sol-gel form or in a polymer matrix solution. It has also been demonstrated that PbS/PbSe core–shell nanocrystals are immune to degradation during the drying process [17]. The use of such dots will significantly enhance the radiative efficiency and the output intensity of the microcavity light sources in future.

In conclusion, we demonstrated a silicon-based light emitter based on high-Q random cavities in disordered photonic crystal waveguides with embedded colloidal PbSe quantum dots. Emission with a minimum linewidth of 4 nm is observed. Such nanoscale light sources on silicon, with potential compatibility with complementary metal oxide semiconductor chips, could be of interest for optical interconnects in silicon photonics.

Chapter III

1.5 µm PbSe Colloidal Quantum Dot Coherent Electroluminescent Devices on Silicon

3.1 Introduction

Several technologies are currently being investigated to realize a silicon complementary metal oxide semiconductor (CMOS)-compatible lightwave network for inter- and intra-chip optical interconnects. As one of the promising candidates for the gain media, chemically synthesized colloidal QDs such as Pb(S, Se) have been investigated. By coupling their emission to the resonance of suitable high quality factor microcavities such as photonic crystals [26], toroidal microcavities [27], photonic beads [28], silicon-on-insulator (SOI) membranes [29], and glass capillaries [30], amplified spontaneous emission and lasing was demonstrated.

For a more compact and versatile light source on a silicon platform, an electrically injected coherent light source is highly desired. In this chapter, electrically injected enhanced spontaneous emission from PbSe QDs, characterized by a spectrally narrow linewidth, is presented. In order to achieve this, two approaches have been investigated. First, to realize an electroluminescent device, QDs were immersed in a conjugated polymer matrix with suitable charge transport layers and linked to silicon PC microcavities. As the QD emission is coupled with the microcavity resonances, spectrally narrow enhanced spontaneous emission was attained. The second approach utilizes the

chemical treatment on PbSe QDs to remove the long-chain oleate ligand coating QDs, which enables direct carrier injection to QDs through an indium tin oxide (ITO) and ZnO nanocrystals. By embedding the light emitting region between highly reflective DBR and metal mirrors, fabricated on a (001) silicon substrate, coherent and directional emission was observed at ~1.55 μm.

3.2 Electroluminescence from silicon-based PC microcavities with PbSe QDs

3.2.1 Device design

PbSe QDs are chemically synthesized by the same method which is described in Chapter 2. In order to fabricate a device suitable for electrical injection, PbSe colloidal QDs are mixed with poly[2-methoxy-5-(2'-ethyl-hexyloxy)-1,4-phenylene vinylene] (MEH-PPV), a conductive polymer matrix, and sandwiched between an indium tin oxide (ITO) anode and a thermally evaporated top cathode consisting of tris(8-hydroxyquinoline)aluminum (Alq_3), calcium, and aluminum.

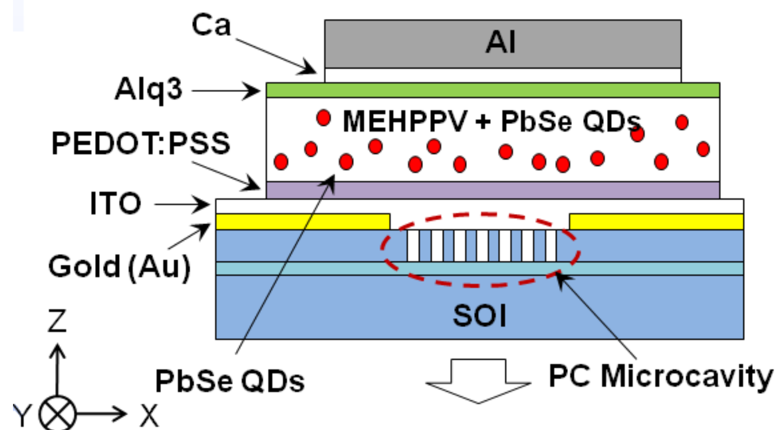

Figure 3.1 Schematic of the device heterostructure fabricated on silicon-on-insulator (SOI). PbSe quantum dots with MEH-PPV are clad by PEDOT:PSS on the ITO anode and Alq_3/Ca/Al cathode.

The device heterostructure is schematically shown in Fig. 3.1. The ITO surface is altered by a layer of poly(3,4-ethylenedioxythiophene) poly(styrenesulfonate) (PEDOT:PSS), the purpose of which is two-fold: to make it smooth to prevent electrical shorts, and to align the Fermi level of ITO with the hole state of PbSe QDs as closely as possible for the efficient hole injection (Fig. 3.2).

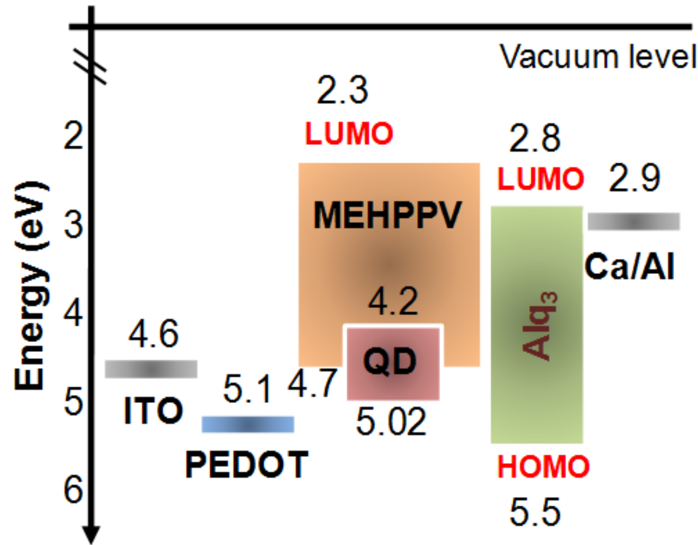

Figure 3.2 Energy band diagram of device heterostructure with PbSe quantum dots as a gain medium.

The resonator was designed as an L3 defect PC microcavity with three missing holes in a line in the silicon layer of an SOI wafer. The PC is therefore clad by SiO_2 and ITO on the two opposite surfaces. The outer air holes at the edges of the L3 cavity are shifted by 0.1*a* (Fig. 3.3(a)) in order to reduce leaky components of the in-plane electric field and attain a high Q-factor [8]. Since ITO is deposited on the photonic crystal with air holes, it was expected that a small amount of filling of the holes would be unavoidable due to the conformal nature of the deposition. However, as shown in Fig. 3.3(b), the degree of filling is extremely small. The Q-factor and modal volume of the L3 cavities, as

estimated from three-dimensional (3D) finite difference time domain (FDTD) calculations, are 2,000 and 0.14 μm^3 (~$1.6(\lambda_c/n)^3$), respectively. Asymmetric cladding by SiO_2 and ITO, both having refractive indices larger than air (n=1) results in a smaller Q-factor and larger modal volume than previously reported values [8].

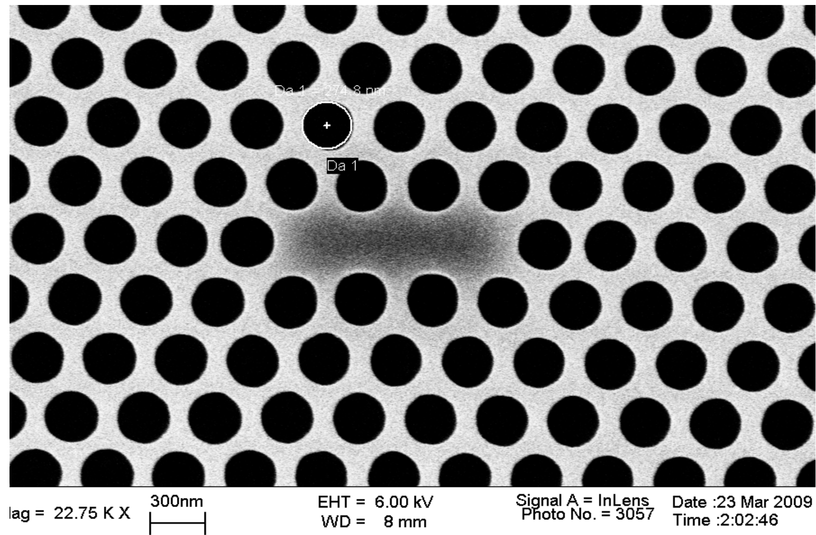

(a)

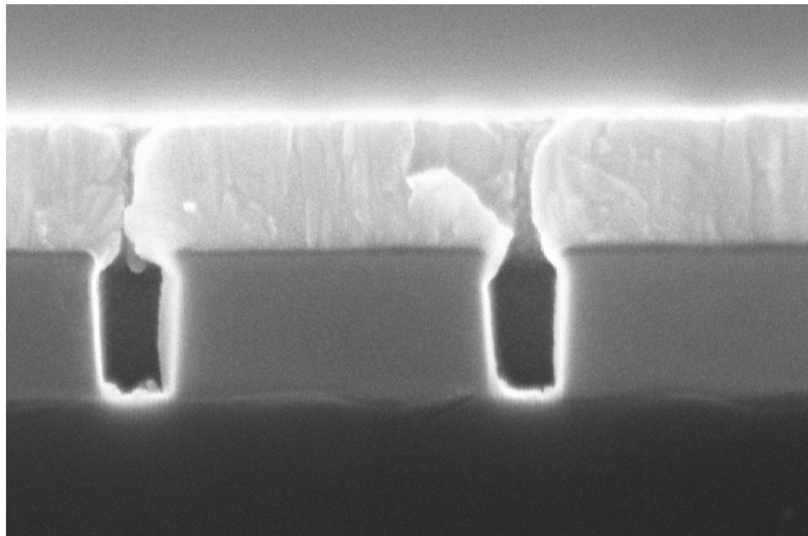

(b)

Figure 3.3 (a) Scanning electron microscopy (SEM) image of the L3 defect photonic crystal (PC) microcavity in silicon. Out air holes at both edges in the defect are shifted by 0.1*a*; (b) SEM image of a cross section of PC microcavity in silicon after ITO deposition. Filling of holes with ITO is negligible.

Unlike a regular PC microcavity device, the PbSe QDs in this device are spatially separated from the PC resonator by a 200 nm ITO layer. However, this separation is short enough for the light from the PbSe QDs to couple to the PC slab since the light wavelength in ITO is ~1.22 μm (corresponding to 1.55 μm in free space). Figure 3.4 shows the electric field (red line) along the z-direction calculated by the transfer-matrix method with the refractive index profile shown (blue line). Due to the thin silicon layer, the fundamental mode only exists in this structure and no higher modes are found. Although the electric field is mostly confined in a silicon layer with a high refractive index, a small amount of electric field is still extended into a QD layer.

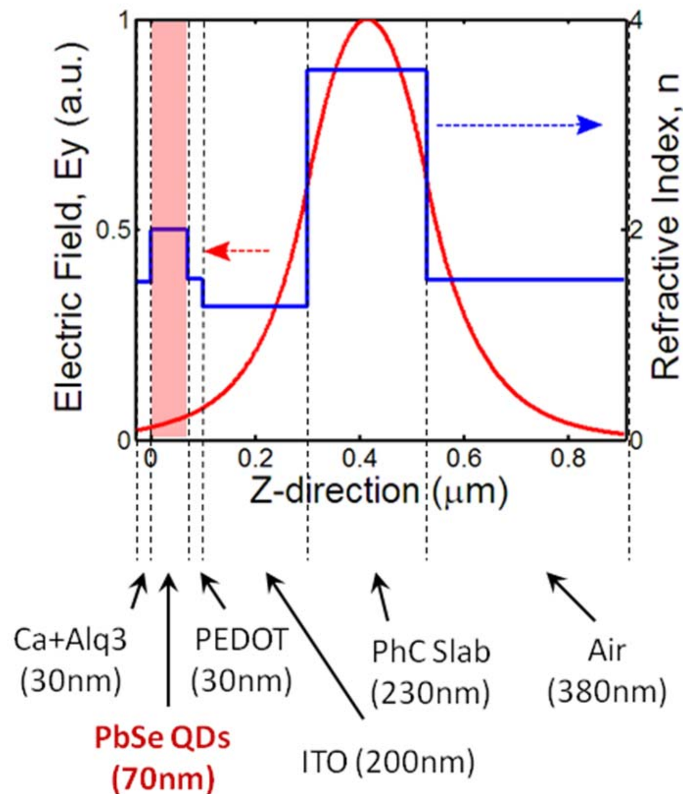

Figure 3.4 Distribution of the electric field (red line) along the z-direction (vertical direction) calculated by the transfer-matrix method with the refractive index profile shown (blue line). The shaded area corresponds to the overlap of confined electric field in the PC slab with the gain medium.

In order to quantitatively calculate the overlap of the confined electric field in the PC slab with PbSe QDs, a three dimensional finite difference time domain (FDTD) calculation was carried out. Figure 3.5 shows the electric field of a cavity mode calculated by the FDTD method in different planes and it is clear that the electric field of a cavity mode extends to the PbSe QDs layer. The calculated overlap of the electric field and PbSe QDs is ~5%, which is comparable to the confinement factor in single quantum-well lasers and this value is very sensitive to the ITO thickness.

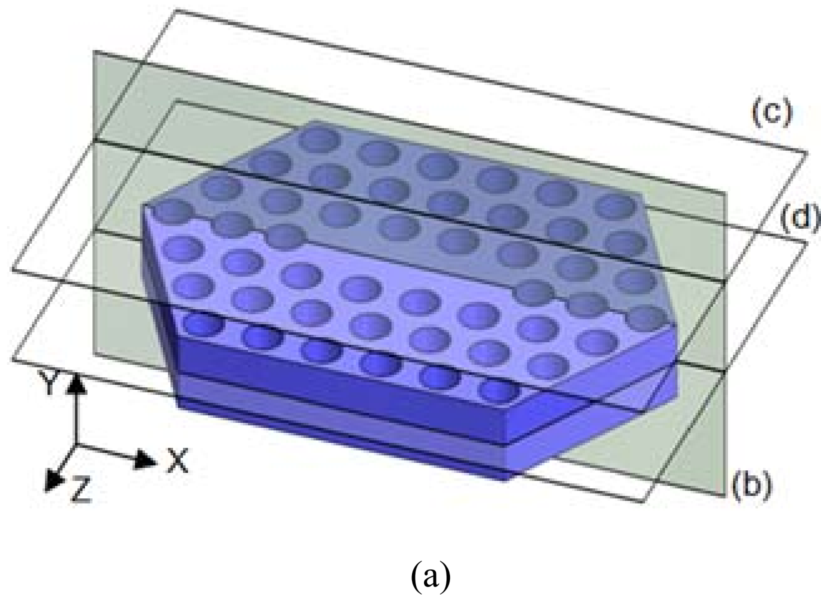

(a)

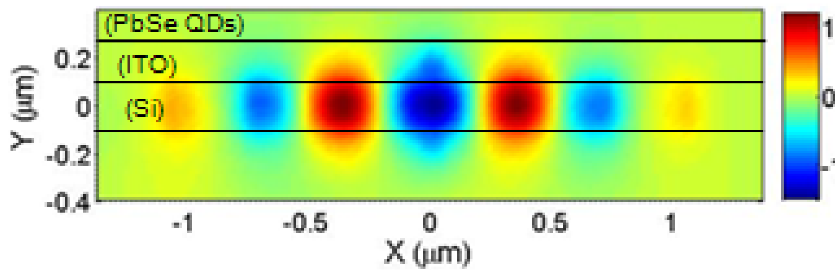

(b)

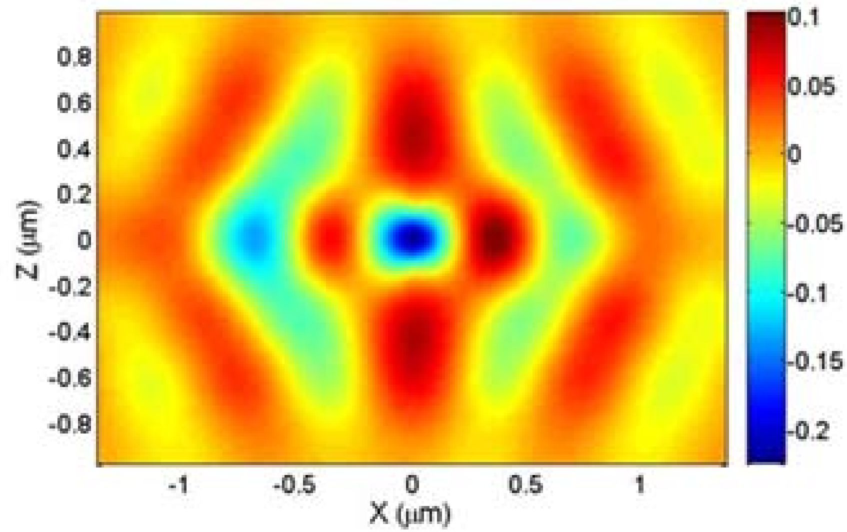

(c)

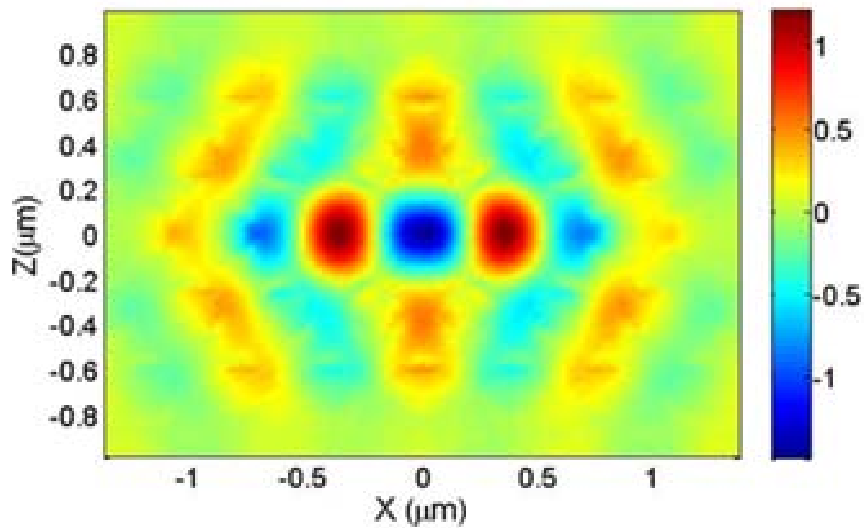

(d)

Figure 3.5 (a) Three dimensional schematic of L3 defect photonic crystal microcavity; (b), (c), and (d) numerically calculated electric field profile (E_z) of the cavity mode in *x-y* plane at the center of a defect (b), *x-z* plane at the interface of ITO and PbSe QD (c), and *x-z* plane at the center of a defect (d).

3.2.2 Fabrication

The fabrication of the device was done by positioning the active gain medium on the PC microcavities. Figure 3.6 shows the detailed descriptions of the fabrication steps.

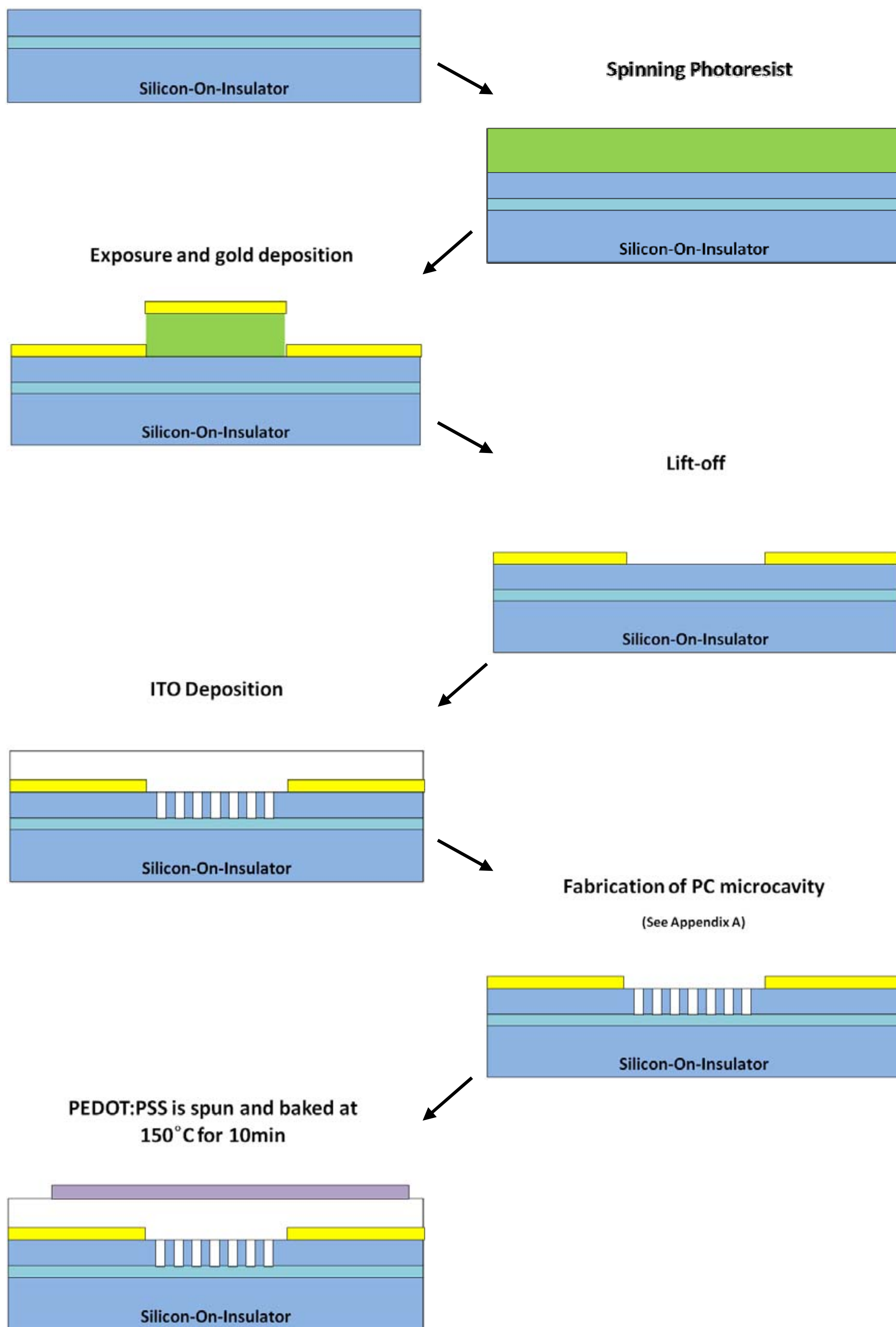
Silicon-On-Insulator
Spinning Photoresist
Silicon-On-Insulator
Exposure and gold deposition
Silicon-On-Insulator
Lift-off
Silicon-On-Insulator
ITO Deposition
Silicon-On-Insulator
Fabrication of PC microcavity
(See Appendix A)
Silicon-On-Insulator
PEDOT:PSS is spun and baked at
150°C for 10min
Silicon-On-Insulator

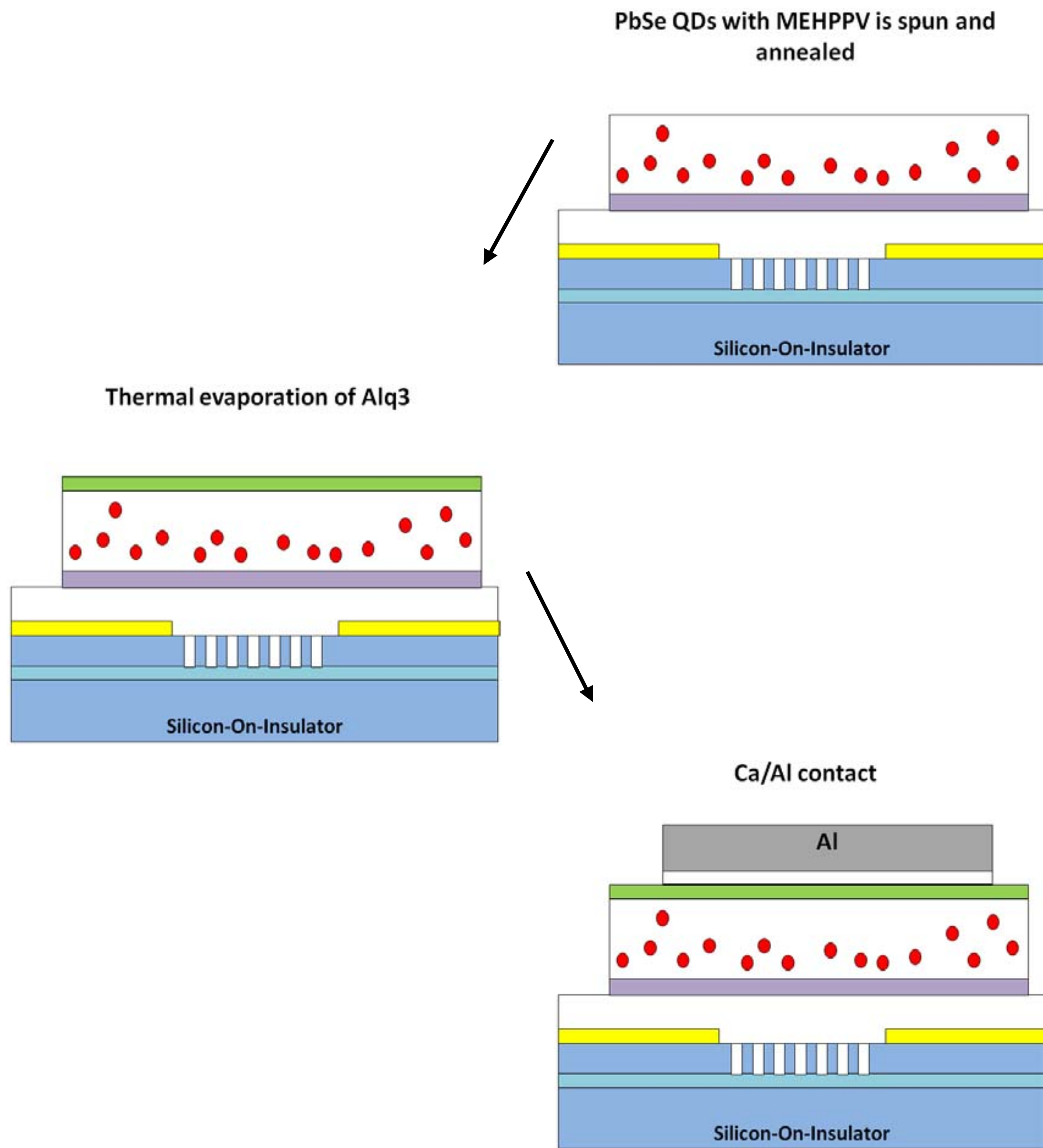

Figure 3.6 Flow chart of device fabrication. See appendix A for photonic crystal fabrication.

First, alignment marks are made on the back side of a double side polished silicon wafer. By aligning all patterns on top side with respect to them, the device on top side can be easily located from the back side when characterized. A 90 μm diameter circular

active area is defined by standard optical lithography and metal (20 Å NiCr, and 130 Å Au) lift-off to block the background light. A 50 nm thick SiO_2 layer is deposited by plasma assisted chemical vapor deposition (PECVD) at a temperature of 300 ^oC. After samples are cleaned by acetone and isopropyl alcohol (IPA), and dried, polymethyl methacrylate (PMMA) 950K A4 (Microchem) is spin coated on silicon at 3,000 rpm and baked on a 180 ^oC hot plate for 2min to evaporate any solvent residue. A photonic crystal, consisting of a triangular lattice of air holes with period a=400 nm and hole radius r=110-130 nm, is patterned in the PMMA layer by electron beam lithography with an accelerating voltage of 20 kV and an aperture size of 10 μm. The pattern in PMMA is transferred into a SiO_2 layer by reactive ion etching (RIE) and the PMMA is cleaned using an oxygen plasma and acetone. Finally, the silicon layer is etched by inductively coupled plasma (ICP) RIE with a SiO_2 etch mask and the remained SiO_2 is removed by buffered hydrofluoric (HF) acid for a short time. Multiple devices with varying air hole size in the PC, ranging from 200 to 260 nm in diameter, were fabricated in order to compensate for the wavelength shift of the resonant mode due to partial filling of the air holes with ITO. Figure 3.7 shows the photonic crystals fabricated in the circular active area, defined by a metal.

Subsequent ITO deposition on the PC microcavity is followed by spin casting of PEDOT:PSS and baking at 150ºC for 10 min. PbSe QDs/MEH-PPV with a 45wt% of QDs is spin casted at 2,000 rpm on top of the PEDOT: PSS layer and annealed at 100°C for 30 min in an inert environment with both oxygen and water concentration lower than 5 ppm. After the device is cooled down to room temperature, 30 nm Alq_3, 5 nm Ca, and 160 nm Al are thermally evaporated in succession. A metal mask with a diameter of 3

mm is used to define the electrode. The evaporator is operated under a vacuum of 1×10^{-7} torr.

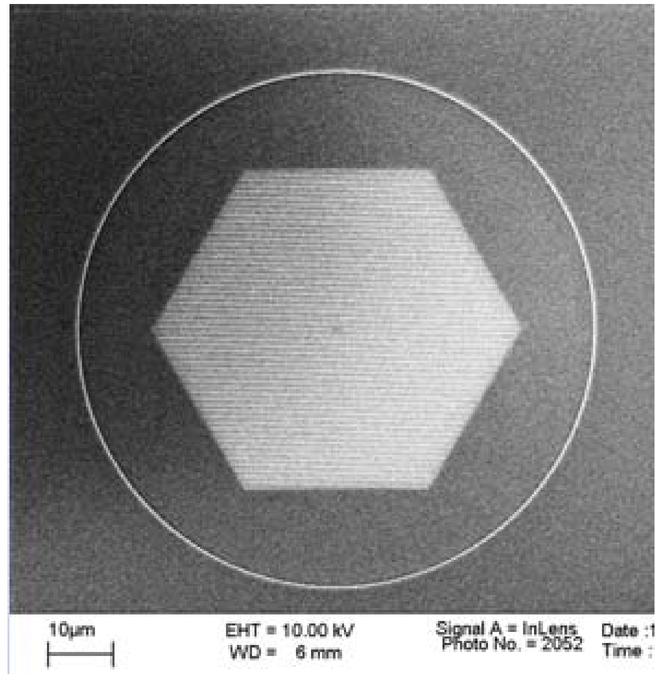

Figure 3.7 The circular active area is defined by standard optical lithography and a metal lift-off. Photonic crystals are aligned within this area and patterned by electron beam lithography and reactive ion etching.

3.2.3 Device characterization

The devices were characterized at room temperature by applying a forward bias between the ITO anode and the Al cathode. Figure 3.8 shows the measured current-voltage (I-V) characteristics of the device with a turn-on voltage of ~12 V and a measured series resistance of ~86 Ω beyond the turn-on voltage. The light output from the device was analyzed with a 0.75 m high-resolution monochromator and detected with an InGaAs photomultiplier tube using phase lock-in amplification.

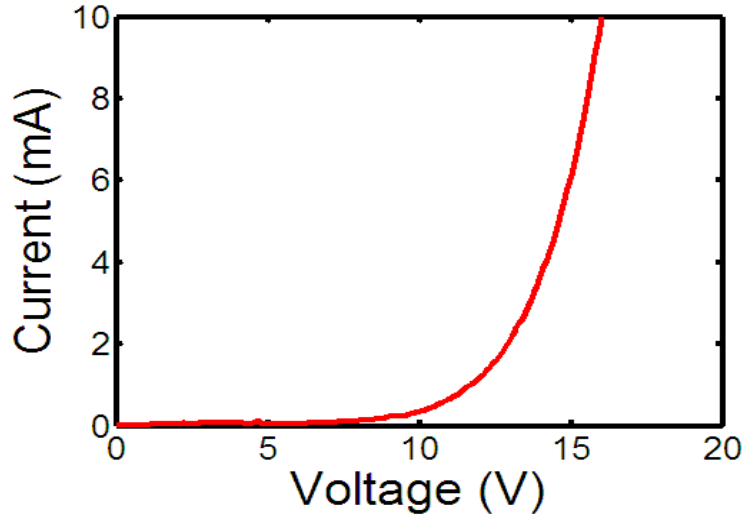

Figure 3.8 The measured current-voltage characteristic of the device. A turn-on voltage is around 12 V with a series resistance after a turn-on estimated to be ~86 Ω.

A control device without the PC microcavity and gold blocking layer, which has an active area of ~7 mm^2, was also fabricated in order to measure the electroluminescence spectra of the PbSe QDs. The output spectra of the control device without a PC microcavity exhibits a broad emission between 1.4-1.7 µm, with a full-width-at-half-maximum (FWHM) of ~180 nm (Fig. 3.9(a)). This electroluminescence is smooth and symmetric, showing a perfect fit to a Gaussian curve. On the other hand, as shown in Fig. 3.9(b), the room temperature spectral output of the device with a PC microcavity exhibits a distinct resonance at λ=1669 nm with a linewidth of ~4 nm at an injection current of 8 mA (a current density of 113 mA/cm^2), which corresponds to a cavity Q factor of ~420. In contrast to the control device, the device with a PC microcavity has a 1,000 times smaller active area (~6.4×10^{-3} mm^2); hence the broad background light is not seen. The reduction in Q factor, from the calculated value, is believed to be due to imperfect device fabrication.

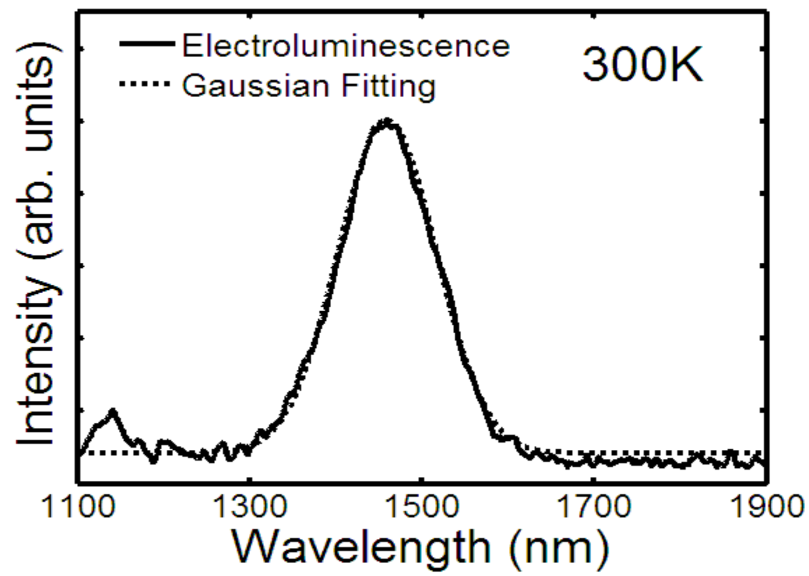

(a)

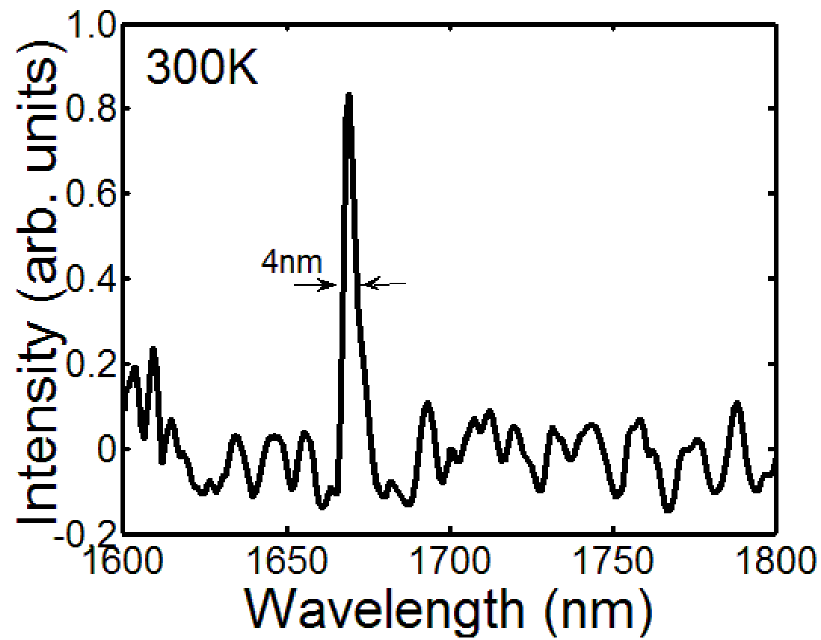

(b)

Figure 3.9 Measured room temperature electroluminescence of the control device without a photonic crystal microcavity and a gold blocking layer (a) and the device with a photonic crystal microcavity (b); (b) the resonant mode is clearly observed at λ=1669 nm with a linewidth of ~4 nm.

In a second device, a similar electroluminescence spectra was osbserved, but with a wider emission linewidth (Fig. 3.10(a)). The measured light-current characteristic of this device, shown in Fig. 3.10(b), displays a turn-on behavior at ~6mA which could be due to a relatively large carrier loss caused by nonradiative surface recombination [31].

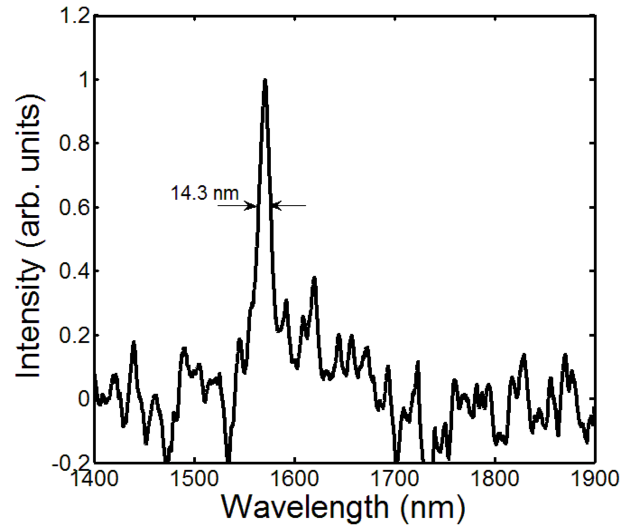

(a)

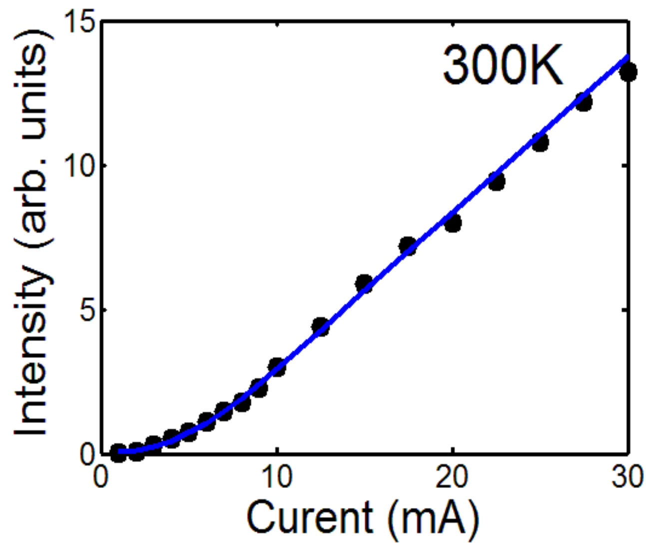

(b)

Figure 3.10 (a) The measured room temperature electroluminescence of the second device, showing a resonant mode at 1571.2 nm with a linewidth of 14.3 nm; (b) measured light-current characteristics of the resonant mode in a second device showing a turn-on current of ~6 mA.

3.3 Coherent and directional electroluminescence from PbSe QDs embedded between DBR and metal mirrors

The long-chain oleate ligand coating surfaces of PbSe QDs is detrimental in electrically injected devices in that it impedes the carrier injection from electron and hole transporting layers into the QDs, which requires a high turn-on voltage. Moreover, off-positioning of a PbSe QD layer from a microcavity results in the small overlap between QDs and the cavity field, which limits the Purcell enhancement and makes lasing less possible. By employing a chemical treatment on PbSe QDs, electronic coupling between them is remarkably improved.

3.3.1 Device heterostructure

The device heterostructure is schematically shown in Fig. 3.11(a). The light emitting region consists of PbSe QD layers, an indium tin oxide (ITO) with poly(3,4-ethylenedioxythiophene) poly(styrenesulfonate) (PEDOT:PSS) as a hole transporting layer (HTL), and ZnO nanocrystals as an electron transporting layer (ETL). PbSe QDs are synthesized by a non-coordinating solvent technique [17] and 6 nm size of PbSe QDs are chosen for 1.55 μm emission. Ethanedithiol (EDT) treatment on PbSe QDs was employed to increase the electronic coupling between PbSe QDs by displacing long chain oleat ligand [32]. PEDOT:PSS provides a smoother surface for ITO, which prevents morphologically induced electrical shorts and allows holes to be efficiently injected into the PbSe QDs, which is shown in the energy band diagram (Fig. 3.11(b)).

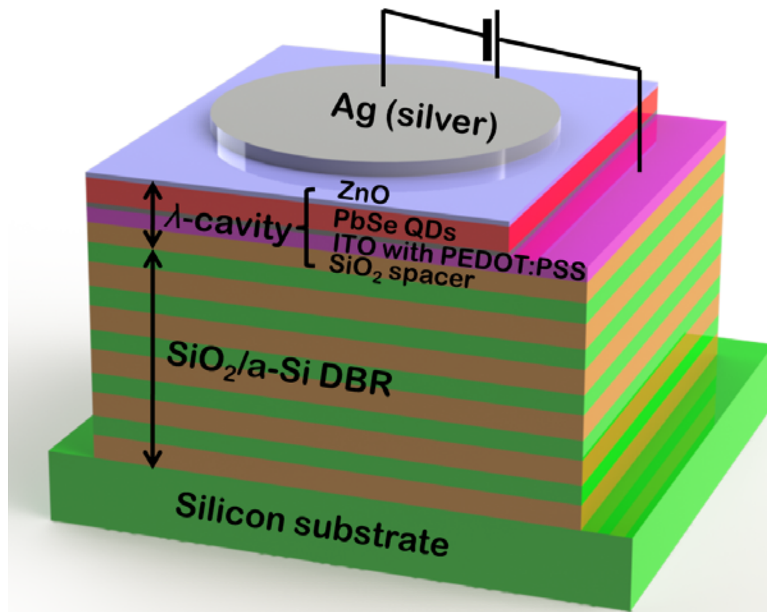

(a)

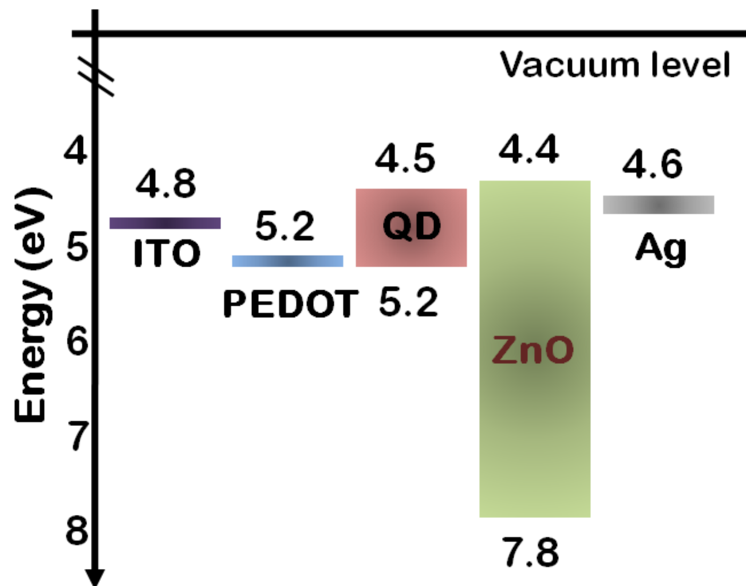

(b)

Figure 3.11 (a) Schematic of the device heterostructure fabricated on a silicon substrate. The light emitting region consisting of ITO, PEDOT:PSS, and ZnO, is clad by Ag and the bottom DBR which is made of SiO_2 and amorphous-Si; (b) energy band diagram of the device heterostructure. Electron and hole states of PbSe quantum dots are well aligned with the work functions of ZnO and PEDOT:PSS.

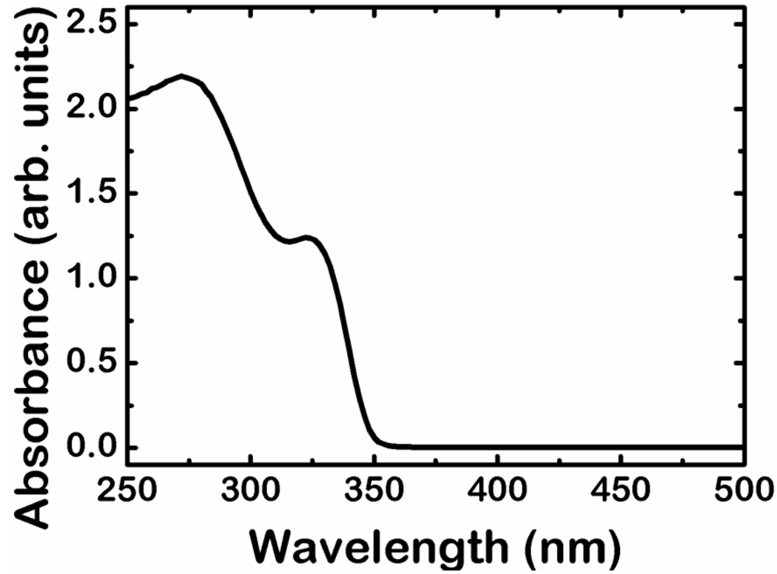

Figure 3.12 Absorption of as-synthesized ZnO nanocrystals showing a shoulder peak around 320 nm ($E_g \sim 3.9$ eV).

ZnO nanocrystals are also chemically synthesized by hydrolysis and condensation of zinc acetate dihydrate by potassium hydroxide in methanol [33], and treated by ultraviolet (UV) light to enhance the conductivity, which is known to passivate electron traps on the ZnO surfaces [33, 34]. As shown in Fig. 3.12, the measured absorbance spectrum exhibits a shoulder peak around 320 nm, corresponding to the bandgap energy of 3.9 eV. This in turn gives an average particle size of 3.5 nm [35]. ZnO nanocrystals are inherently n-type and, therefore, offers an efficient electron injection by aligning conduction band with the electron states of PbSe QDs. In order to tune a resonance wavelength, 100-500 nm thick SiO_2 is additionally inserted between ITO and the DBR, which tailors the cavity length from λ/2 to λ. The 5-period, highly reflective bottom DBR, deposited on the silicon substrate is composed of amorphous silicon (a-Si) as the high refractive index layer ($n_r \sim 3.48$) and SiO_2 as the low refractive index layer ($n_r \sim 1.52$).

The top mirror is formed by a layer of Ag. Measured reflectivity spectrum of the DBR and Ag mirror, as shown in Fig.3.13, exhibits a very high reflectivity of ~98.7 % at λ ~ 1.55 μm. The bandwidth of the photonic stopband spans the wavelength range of 1.3-1.6 μm due to a large index difference between a-Si and SiO_2. This avoids the Bragg mode overlap with the QD emission and ensures single mode operation.

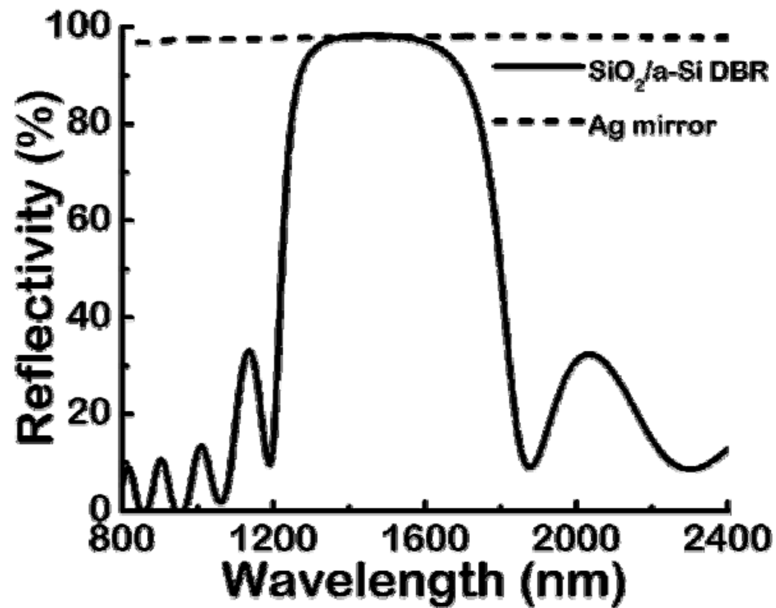

Figure 3.13 Measured reflectivity spectra of Ag mirror and SiO_2/a-Si DBR. Both mirrors exhibit a high reflectance of ~98 % from 1400 nm to 1700 nm.

The Q factor of the λ-cavity device, calculated with the measured reflectivity of the DBR and Ag mirrors is about 500. Figure 3.14 shows the electric field calculated by finite difference time domain (FDTD) method, with the refractive index profile shown. In order to account for the dispersive property of the metal, the dielectric function of Ag is modeled as a sum of Lorenzian functions [36]. The maximum electric field spatially coincides with a layer of PbSe QDs, which is highlighted in this figure, and the calculated overlap of the electric field in a cavity with the PbSe QD layer is 20 %.

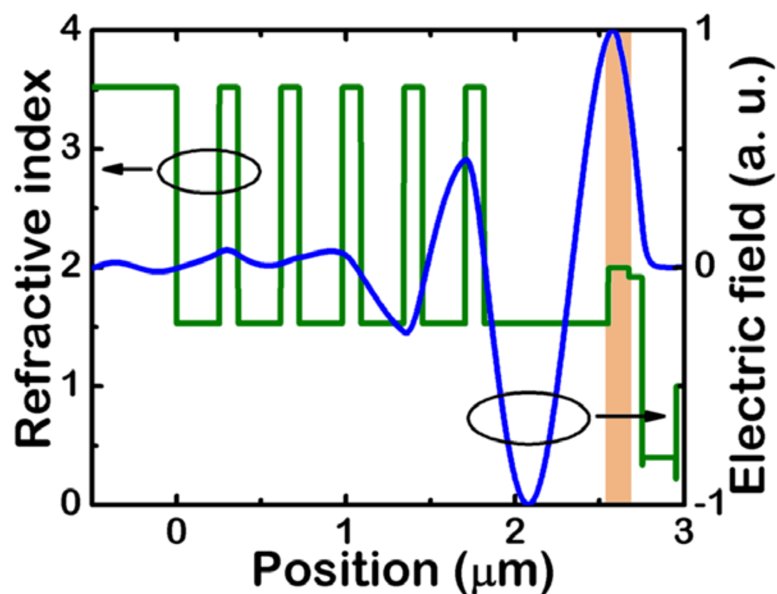

Figure 3.14 Numerically calculated electric field intensity (blue line) in the device with refractive index profile (green line). The maximum electric field spatially coincides with a layer of PbSe QDs, which is highlighted.

3.3.2 Fabrication

The fabrication starts with the deposition of alternating 255 nm thick SiO_2 and 111 nm thick a-Si on (001) silicon substrate by plasma enhanced chemical vapor deposition (PECVD) at 300ºC. Deposition rate and conditions were carefully calibrated to achieve the smooth surfaces needed for a high quality mirror. 250 nm thick ITO was sputtered on the DBR at room temperature and annealed at 250ºC for 30min in a nitrogen atmosphere to increase the film conductivity and improve the surface morphology. After cleaning samples with sonication in acetone and isopropyl alcohol (IPA), the ITO surface was further treated with oxygen plasma to remove organic residue and increase the work function. PEDOT:PSS (Clevios, P VP Al 4083) was filtered through a 0.45 μm polyvinylidene difluoride (PVDF) syringe filter and then spin-coated at 2,000 rpm and annealed at 150ºC for 10min in a nitrogen environment. After the sample was cooled

down to room temperature, it was immediately transferred into an inert ambient with both oxygen and water concentration lower than 5ppm for subsequent processing.

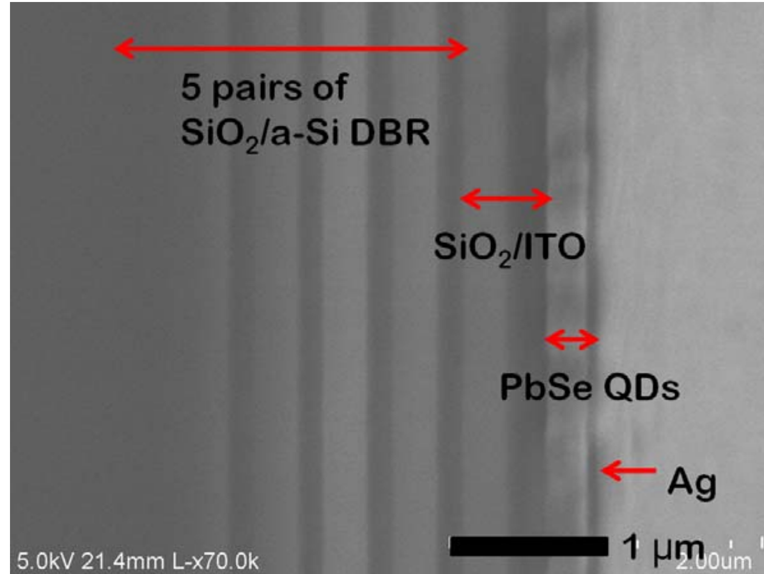

Figure 3.15 A cross-sectional scanning electron microscopy image of the fabricated device. The distributed Bragg mirror consisting of SiO_2 and a-Si is clearly seen.

PbSe QDs suspended in chlorobenzene was spin-cast on top of the PEDOT:PSS layer and 0.1M of EDT in acetonitrile was dropped on the surface. After the lapse of 2 minutes to allow the EDT to react with the oleate ligand of PbSe QDs, the excess EDT in acetonitrile was spun away. This procedure was repeated three times to form a 100 nm thick uniform QD layer [32], and the QD film was baked at 80ºC for 30min to remove solvent residue. After deposition of a PbSe QD layer, ZnO nanocrystal in ethanol was spin-coated and baked at 80ºC for 30min. Finally, the Ag cathode with an area of 1mm^2 was thermally evaporated on top of the ZnO nanocrystal layer with a shadow mask. Figure 3.15 shows a cross-sectional SEM image of the fabricated device.

3.3.3 Device characterization

The current density-voltage (*J-V*) characteristics of the fabricated device were measured at room temperature in a nitrogen rich ambient to prevent device degradation. Figure 3.16 shows the measured *J-V* characteristic on a log-log plot. The slope of the plot increases around 2.3 V, which is believed to be the onset of electron and hole injection into the QDs [37]. A decrease of the *J-V* slope is observed as the bias is increased above 5 V, which indicates that the carrier injection is limited by series resistance of either the ETL or the HTL. The measured *J-V* characteristics, plotted on a linear scale, including the reverse bias region, shows good rectifying behavior (inset of Fig. 3.16).

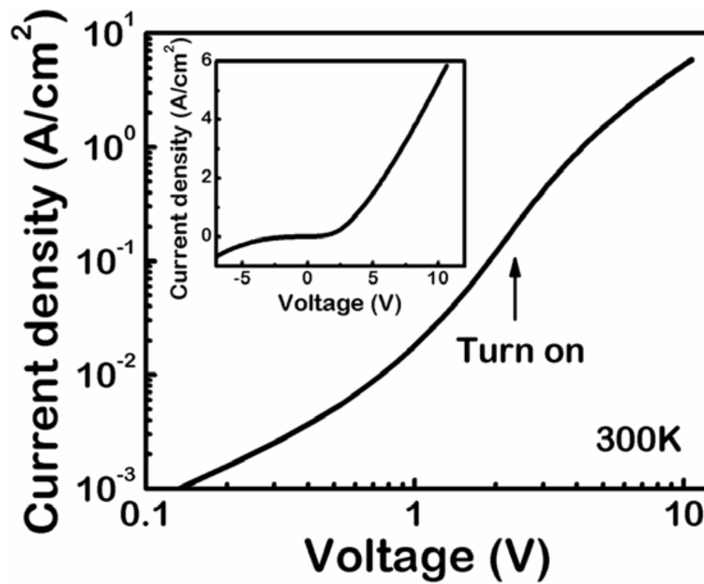

Figure 3.16 Measured current density-voltage characteristics of the fabricated device on a log-log plot. The increase of the slope at 2.3 V indicates the onset of carrier injection into the QDs. The inset shows *J-V* characteristics in linear scale, which exhibiting a good rectifying behavior.

For electroluminescence (EL) measurements, a forward bias was applied between the ITO anode and the Ag cathode. In order to avoid heating, a pulsed current source was used with a repetition rate of 50 Hz and a duty cycle of 50%. The light output from the

device was analyzed with a 0.75 m high-resolution monochromator and detected with a liquid nitrogen cooled Ge detector using phase lock-in amplification.

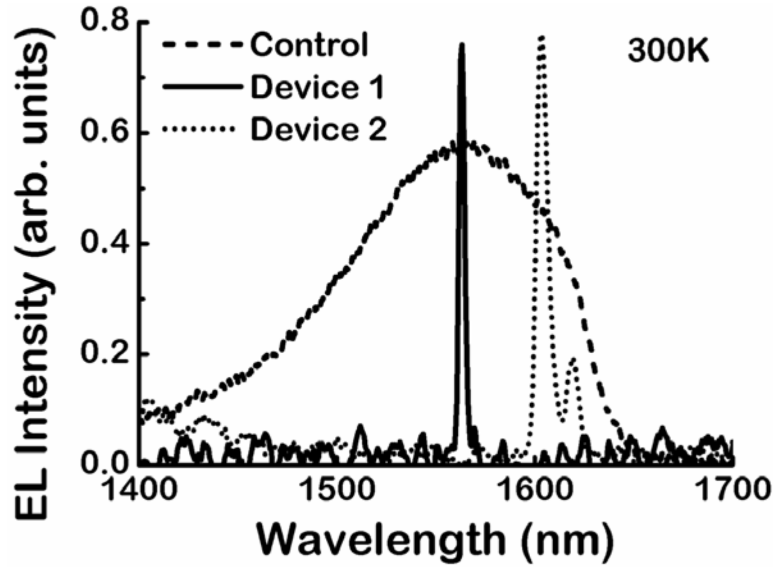

(a)

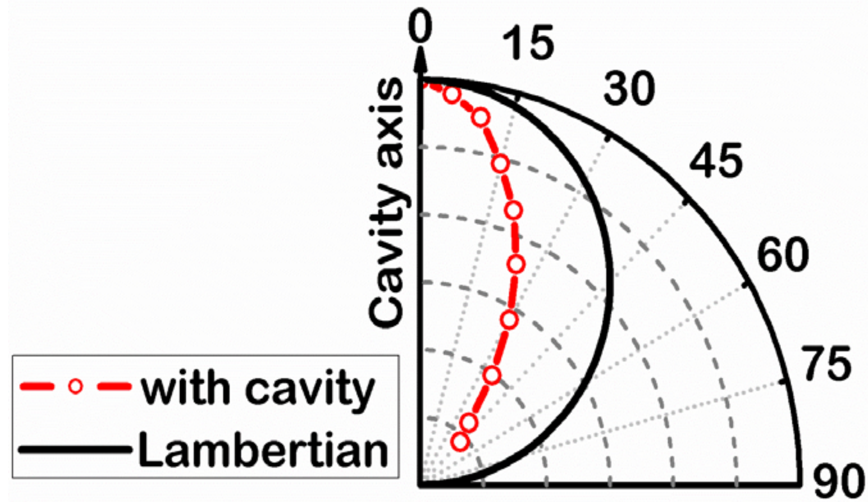

(b)

Figure 3.17 (a) Room temperature electroluminescence spectra from the control sample without a DBR and two devices with different cavity sizes. Resonant modes are tuned by varying the cavity size. The narrowest linewidth is ~3.1 nm at λ=1563.1 nm; (b) angular emission characteristics recorded from the device with a DBR at angles ranging from 0-45 degrees with respect to the cavity axis. The Lambertian pattern is also shown for comparison.

Figure 3.17(a) shows the normalized EL spectra of a control device without a DBR and devices with a DBR. The output spectrum of the control device exhibits a broad emission between 1.4-1.65 μm, with a full-width-at-half-maximum (FWHM) of ~120 nm. On the other hand, the devices with a DBR and two different thickness of SiO_2 spacer show cavity resonances at λ=1563.1 (Device 1) and 1603.7 nm (Device 2), respectively. The narrowest linewidth observed is ~3.1 nm at an injection current density of 3 A/cm^2 from Device 1, which is ~38 times less than that of the control device and corresponds to a cavity Q factor of 500. The additional peak at λ=1619.3 nm was also observed on the shoulder of the dominant peak in Device 2. This abnormal peak is due to the non-uniform cavity thickness over the relatively large device (~1 mm^2). The light emission from the device with a DBR was also measured at angles ranging from 0-45 degrees with respect to the cavity axis, as shown in the angular emission characteristics (Fig. 3.17(b)). Also shown is the Lambertian emission pattern for comparison. The device with a DBR exhibits a highly directional light output parallel to the cavity axis, showing a smaller divergence compared to the Lambertian emission pattern.

The measured light-current density characteristics, shown in Fig. 3.18, displays the linear increase of light output as the current density increases. The onset of light output inferred from the extrapolation of the linear fit to the measured points is around 2.4 V, which coincides with the turn-on estimated from the *J-V* characteristics. As the current density increases above 4 A/cm^2, the integrated light output becomes saturated due to heating.

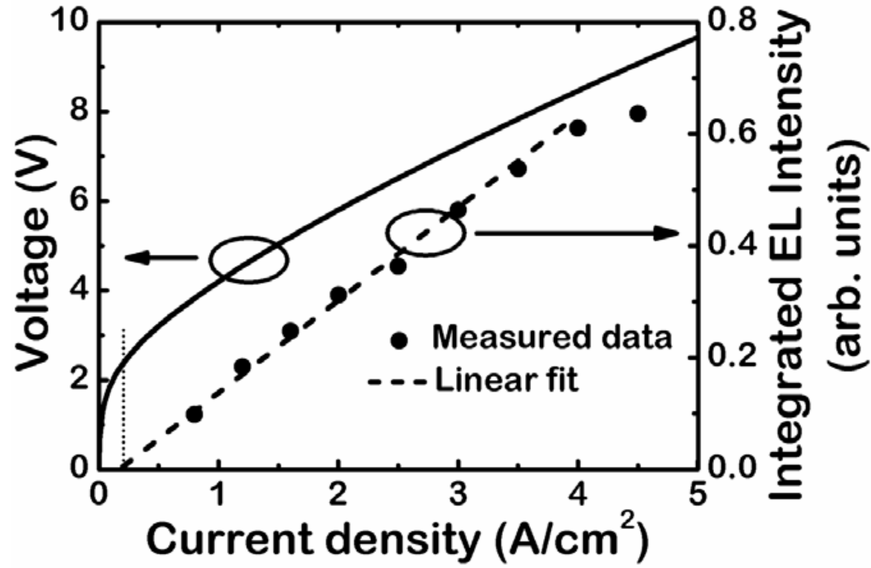

Figure 3.18 Measured voltage-current density and light-current density characteristics of the device. The integrated light output increases linearly with current. The extrapolation of the linear fit indicates a turn-on voltage of ~2.4 V.

3.4 Discussion

Based on the electronic band degeneracy (8-fold degeneracy) [38] and radiative recombination lifetime of single excitons in PbSe QDs (0.88 μs) [39], it is envisioned that a carrier density, given by the average number of photoexcited electron-hole pairs in a PbSe QD per second, of ~ 5×10^6 carriers will be necessary to achieve population inversion in PbSe QDs. Such a carrier density translates to an injection current density of 0.5 A/cm^2 with an assumed dot density of 10^{12} /cm^2. In reality, multi-exciton recombination may be the dominant recombination process. If this is indeed the case, the very short lifetime (~0.1 ns) of multi-excitons will require a current density of ~5 kA/cm^2 to achieve stimulated emission. The required injection in a practical device will be close to this value. Therefore, the observed resonance is a manifestation of the Purcell effect

which enhances the spontaneous emission (see appendix A). The maximum achievable Purcell factor is expressed by

$$F_C = 3\lambda_c^3 Q / 4\pi^2 n^3 V_{mode} \tag{3.1}$$

In the first electroluminescent device with a PC microcavity, we estimate F_C to be ~25 based on an estimated mode volume of ~$1.6(\lambda_c/n)^3$ and a cavity Q of ~420. Since this is the maximum value theoretically calculated assuming that the emitter is positioned at the maximum electric field, additional measurements such as time-resolved electroluminescence of PbSe QDs with and without the PC microcavity are required to accurately estimate the enhancement of spontaneous emission.

In order to achieve coherent emission and lasing, a microcavity with a higher Q factor together with more robust electron and hole transporting layers, to withstand a higher current density, are required. In the first electroluminescent device with a PC microcavity, reducing the ITO layer thickness would be an effective way to increase coupling of the light from the gain medium to PC slab. However, this would increase the series resistance in ITO and would fail to provide the optimum lower refractive index layer cladding for the PC microcavities, resulting in a low Q factor. In addition, oxygen and water in the environment are detrimental to the organic material based electron and hole transporting layers, especially during current injection. In the second approach, we remarkably improved electrical injection to QDs but the current density was still lower than theoretical estimation to achieve lasing. The observed resonance is due to the Purcell effect which enhances the spontaneous emission and significantly decreases the emission linewidth. Therefore, investigation of reducing the series resistance in the charge transporting layers will be of intense research.

3.6 Conclusion

To summarize, coherent emission with a narrow linewidth at room temperature was demonstrated from electrically injected PbSe QDs embedded in two different microcavities. The first approach, using PC microcavities exhibits a resonance at λ=1669 nm having a linewidth of 4 nm under a current density of 113 mA/cm^2. This corresponds to a cavity Q factor of ~420. In a second device with bottom DBR and a metal mirror, a minimum linewidth of ~3.1 nm was measured, corresponding to a cavity Q factor of 500, for an extremely low injection current density of 3 A/cm^2. It also exhibits a highly directional emission, which is favorable for efficient fiber coupling. This directional and coherent silicon based light source using colloidal QDs is of interest as a viable technology for optical interconnects as the device is miniaturized.

Chapter IV

Monolithically Integrated GaN Nanowire Laser on Silicon

4.1 Introduction

The successful catalyst-free growth of Ga(In)N nanowires of 20-100 nm diameter and lengths upto 2 μm on both (001) and (111)-oriented silicon substrates has been recently demonstrated [40-49]. The nanowire density can be varied in the range of 10^{8}-10^{11} cm^{-2} and the emission wavelength can be tuned, by varying the In composition, from 366 to 700 nm at room temperature. Most importantly, the nanowires grow vertically in the wurtzite crystalline form and detailed structural characterizations indicate that they are relatively defect-free. This is mainly due to their large surface-to-volume ratio. Consequently, there is much interest in developing nanoscale lasers using semiconductor nanowires [10, 50-55].

Single nanowires have been shown to function as Fabry-Pérot cavities and waveguides due to their thickness being comparable to the effective wavelength in semiconductors [10, 50-54]. However, poor reflectivity (< 0.4) [56] between semiconductor and air requires the nanowire to be very long (~40 μm) to achieve stimulated emission [56, 57], which is not conducive to the realization of nanoscale lasers. Recently, there has been an effort to combine semiconductor nanowires with lithographically-defined cavities such as a one-dimensional photonic crystal (PC) microcavity [54], a microstadium cavity [55], a silica microfiber knot cavity [58], and

two-dimensional distributed feedback scheme [59]. While the modal gain of a nanowire Fabry-Pérot cavity is strongly dependent on the length of the nanowire [57], an external high-Q microcavity which could provide a strong feedback regardless of the dimension of the nanowire offers the possibility of achieve nanoscale lasing.

In this chapter, an optically pumped monolithic single GaN nanowire laser on silicon with a two dimensional (2D) photonic crystal resonant cavity is presented, which has a sub-wavelength modal volume, operating at room temperature.

4.2 Growth of GaN nanowires

GaN nanowires were grown on (001) and (111) Si substrates in the absence of a foreign metal catalyst in plasma-assisted molecular beam epitaxy (PA-MBE) system [49]. First, the surface oxide on the substrate was removed with a 900 °C anneal in the growth chamber. The substrate temperature was lowered to 800 °C and a few monolayers of Ga were deposited in the absence of N. GaN nanowire growth was initiated at the same temperature at a rate of 300 nm/hr under nitrogen-rich conditions. The nitrogen flow rate was held constant at 1 sccm. The aerial density of nanowires was varied in the range of 10^8–10^{11} cm^{-2} by varying the duration and magnitude of the initial Ga flux to form the droplets. A cross-sectional scanning electron microscopy (SEM) image of GaN nanowires with a density of ~10^{11} cm^{-2}, grown on (001) Si with a Ga flux of 1.5×10^{-7} Torr and 3 min pre-deposition of Ga droplets, is shown in Fig. 4.1(a). In order to achieve a low aerial density (~10^8 cm^{-2}), The Ga flux and pre-deposition time of Ga droplets was reduced to 3.5×10^{-8} Torr and 1min, respectively. Figure 4.1(b) shows an oblique view SEM image of GaN nanowires grown on (111) Si with a low density of ~10^8 cm^{-2}. A

single nanowire is vertically aligned and has a length of ~600 nm and a diameter of 20-50 nm. It was observed that while the high density (>10^9 cm^{-2}) nanowires grow vertically both on (001) and (111) Si, the low density nanowires are vertical only on (111) Si. This aspect is under further investigation.

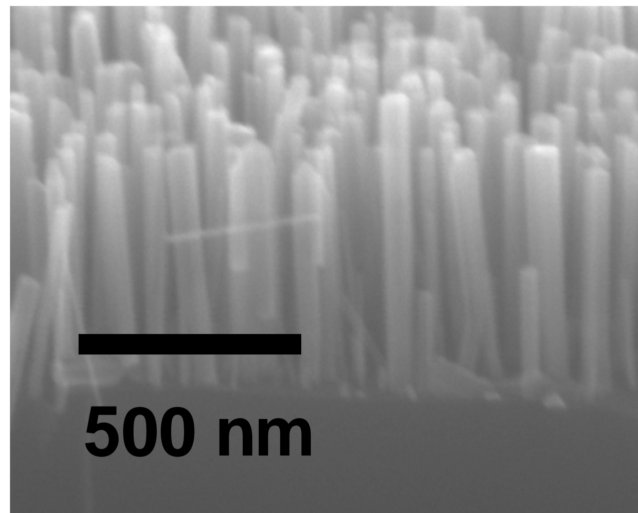

(a)

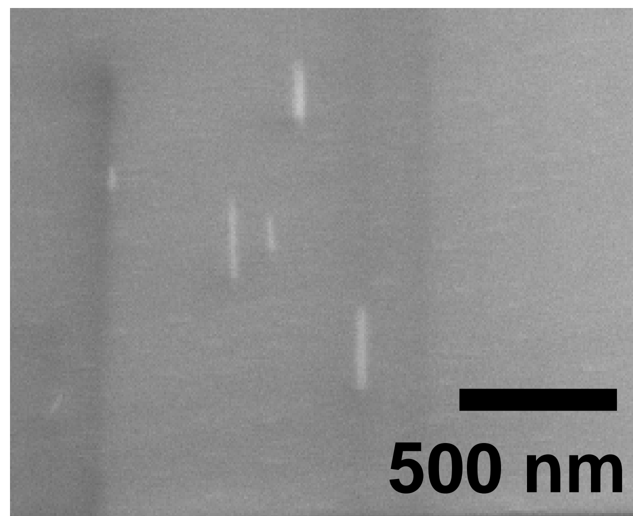

(b)

Figure 4.1 (a) and (b) Cross-sectional SEM images of catalyst-free GaN nanowires grown by plasma-assisted MBE with different densities of ~1×10^{11} cm^{-2} on (001) Si (a) and ~1×10^{8} cm^{-2} on (111) Si (b) under the growth conditions described in the text. The vertically aligned GaN nanowires have a length of ~600 nm and a diameter of 20-50 nm.

High-resolution transmission electron microscopy (HRTEM) studies [49] indicate that the nanowires are relatively defect-free and some evidence of this is provided in the HRTEM image of Fig. 4.2. The diffraction pattern in the inset of Fig. 4.2 reveals that the nanowire has a single crystal wurtzite structure and the *c*-plane is normal to the growth direction.

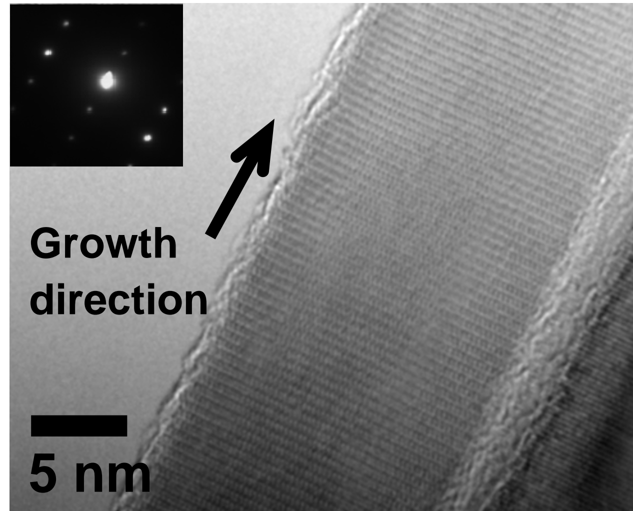

Figure 4.2 High resolution TEM image of a GaN nanowire with a diameter of 20 nm which exhibits no observable defects. The inset shows the diffraction pattern indicating the nanowire is a single crystal wurtzite structure with the *c*-axis along the direction of growth.

4.3 Device design

As confirmed by previous studies [60], the GaN nanowire has the wurtzite crystal structure and the *c*-axis coincides with the geometrical *z*-axis of the nanowire. This results in an anisotropic dispersion curve near the band edge as shown in Fig. 4.3. The small density-of-states in the *x*- and *y*-direction allows the same gain to be achieved with fewer carriers. Also, the small fraction of the *z*-orbital in the HH state causes less coupling between the z-polarized light and the HH state, which gives rise to a smaller

gain near the band edge. Therefore, the gain for the same injection is larger for the x- and y-polarized (TM-polarized) light than for the z-polarized light [60].

Figure 4.3 Anisotropic band structure in the Wurtzite crystal structure. A smaller density of states in the x-direction results in a larger gain near the band edge with the same amount of carrier injection.

The most common photonic crystal structure that is widely employed, from the perspective of ease of fabrication and good optical confinement, is a free-standing 2D PC slab structure. It basically consists of a high refractive index slab freely suspended in air. The 2D PC provides horizontal (in-plane) optical confinement while the vertical (out-of-plane) confinement is provided by total internal reflection at the slab-air interfaces. Such a structure is not a substitute for a 3D PC; however, it provides many of the properties that one desires from a perfect photonic crystal. Figure 4.4 shows the band structure obtained by plane wave expansion (PWE) for such a 2D PC slab with air holes. Modes that are guided in the slab are located below the light line. These modes decay exponentially in the region outside the slab and cannot couple energy to the radiation modes. The modes above the light line are radiation modes that are leaked into the air

cladding. In these dispersion curves, it is worthy to note that a photonic band gap is opened only for the TM-polarized light (in-plane E-field and out-of-plane H-field). Thus, the microcavity for the TM-light is conveniently designed by introducing a defect on a 2D PC slab [61]. As discussed, the GaN nanowire has a larger gain in the x- and y-polarized light (Ex, Ey), and thus the photonic crystal microcavity is suited for maximizing the coupling between the gain medium and the resonant cavity in terms of polarization.

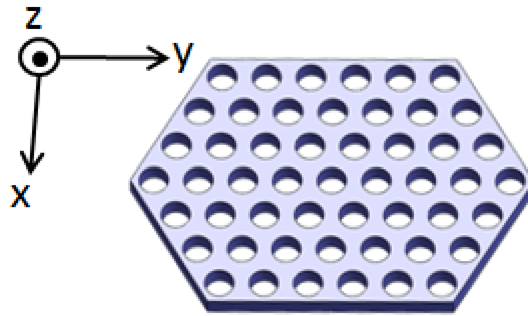

(a)

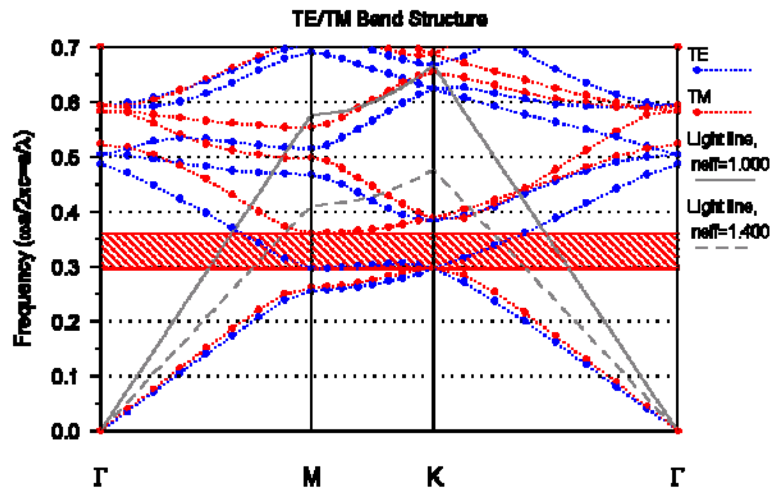

(b)

Figure 4.4 (a) Two dimensional (2D) photonic crystal slab with air holes; (b) calculated dispersion curves of 2D photonic crystal for TM and TE light.

The device heterostructure, schematically shown in Fig. 4.5, consists of a single GaN nanowire at the center of a H2 defect. This single nanowire is surrounded by a 2D PC microcavity fabricated in a TiO_2 layer and a spin-on-glass (SOG) layer as a low refractive index material to reduce optical loss from the TiO_2 layer to the Si substrate. The refractive index is influenced by the method of film preparation [62] and causes detuning of the resonant wavelength. For a better estimation, spectroscopic ellipsometry was carried out to characterize the optical properties of SOG and TiO_2. The measured optical refractive indices of SOG and TiO_2 at λ=380 nm are 1.4 and 2.5, respectively and the imaginary part of the refractive index of TiO_2 is ~0.001. As a resonator, a H2 defect PC microcavity is chosen to tolerate any alignment error in a lithography step and is designed by using the PWE method and three-dimensional (3D) finite difference time domain (FDTD) simulation.

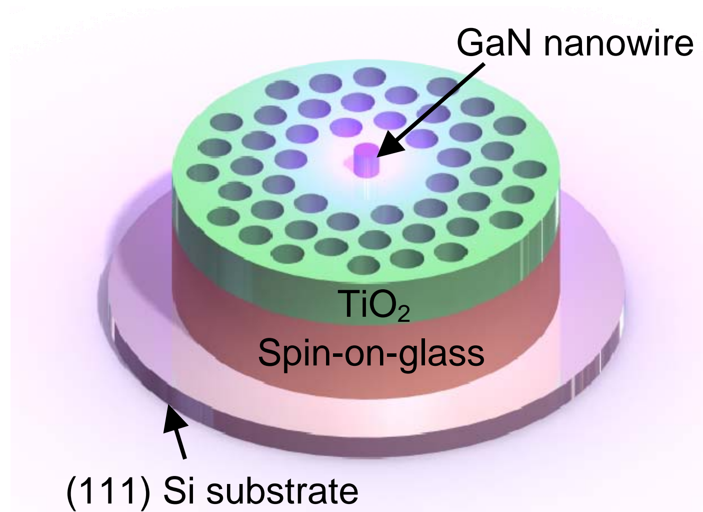

Figure 4.5 Schematic representation of nanowire laser consisting of a single GaN nanowire and a two dimensional photonic crystal microcavity in the TiO_2 layer (120 nm). Spin-on-glass (380 nm) with a low refractive index (n_r=1.4) helps to reduce optical loss from the microcavity in the TiO_2 layer to the Si substrate.

Using the effective refractive index, a 2D PC slab can be approximated to an ideal two dimensional photonic crystal. The effective refractive index is calculated by the transfer matrix method with the measured refractive indices. As shown in Fig. 4.6(a), the optical field of light is strongly confined and the effective refractive index is estimated to be 2.105, which is close to the refractive index of TiO_2. The PC is formed with a triangular lattice of air holes of radius 40 nm and a period 120 nm. A small hollow that is formed around the nanowire in the center of the H2 defect during device fabrication is assumed to be a partially filled hole with a diameter of 80 nm in the calculation. The depth of the hollow was roughly estimated to be ~30 nm based on the amount of TiO_2 deposited on the top of the nanowire. Resonance mode of the H2 defect microcavity calculated by the PWE method with the effective refractive index is shown in Fig. 4.6(b). This appears in the middle of the photonic band gap. Thus, the light confined in the H2 defect cannot propagate in any direction, which ensures a high quality factor (Q) factor.

FDTD simulations are carried out in order to calculate the Q factor and modal volume. After an impulse source is excited inside the defect, multiple monitors placed in asymmetric locations in the cavity record the change of optical fields. For accurate estimation, fast harmonic analysis (FHA) is used at the predicted resonant frequency by PWM. The calculated Q-factor, mode volume, and confinement factor Γ are 570, ~0.003223 μm^3 ($0.92(\lambda/n)^3$), and 0.04, respectively. The modal gain estimated from the Q-factor [63] is ~520 cm^{-1} and the corresponding optical gain at threshold is ~13,000 cm^{-1}, which is achievable in GaN [64]. The calculated mode profile (E_Z) is shown in Fig. 4.6(c) and the peak intensity of the electric field coincides with the nanowire.

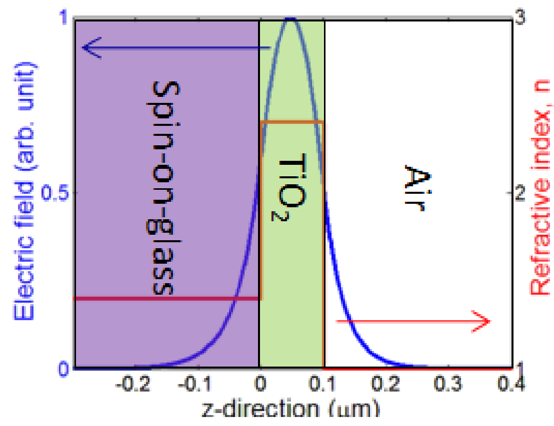

(a)

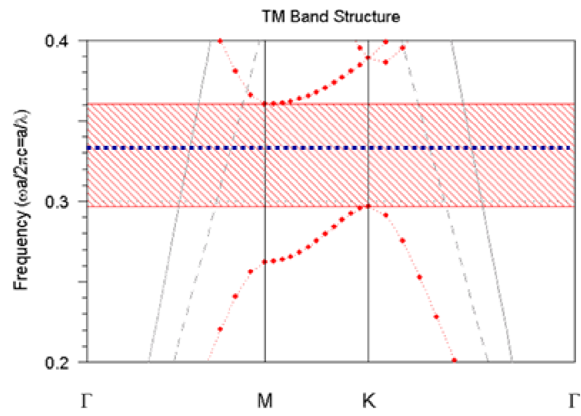

(b)

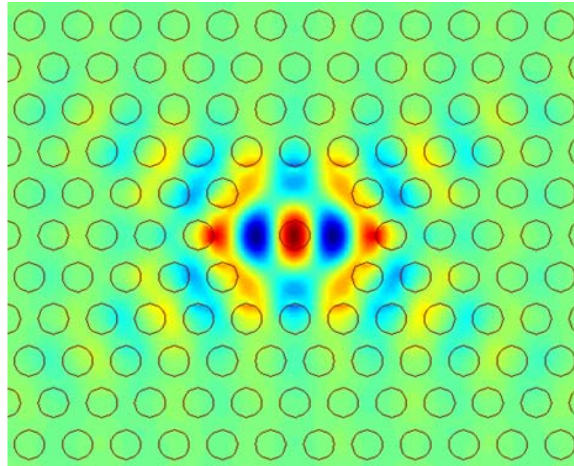
(c)

Figure 4.6 (a) Refractive index profile and calculated electric field by transfer matrix method; (b) the resonant mode of H2 defect (dotted line) and photonic band gap (shaded area); (c) calculated mode profile (E_Z) using 3D FDTD.

4.4 Device fabrication

Device fabrication is initiated with the spinning of a SOG layer on a low density nanowire (~10^8 cm^{-2}) sample grown on (111) Si substrate. The SOG film is baked at 100 °C and 140 °C successively for 4 min to evaporate residual solvents and is then cured at 350 °C on a hot plate for 30 min in the absence of oxygen. A SEM image revealed that the sidewalls of the nanowires are not coated by SOG. After the device is cooled down to room temperature, TiO_2 is deposited by electron beam evaporation. The thickness of the SOG and TiO_2 films, measured by cross-sectional SEM, are 380 nm and 120 nm, respectively.

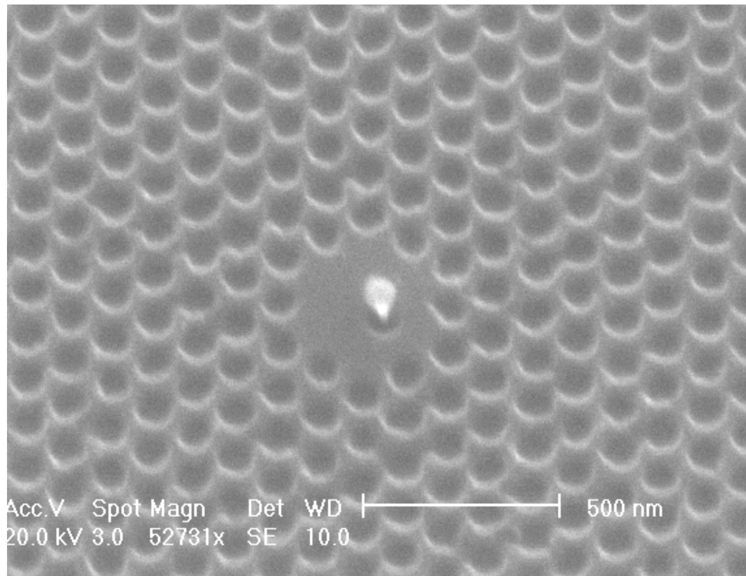

Figure 4.7 An oblique view SEM image of the fabricated device. The single GaN nanowire is well-aligned in the center of the H2 defect of the photonic crystal microcavity. Due to the directional nature of TiO_2 evaporation, a small amount of TiO_2 is deposited on top of the GaN nanowire and a partially filled hollow region is created around the nanowire.

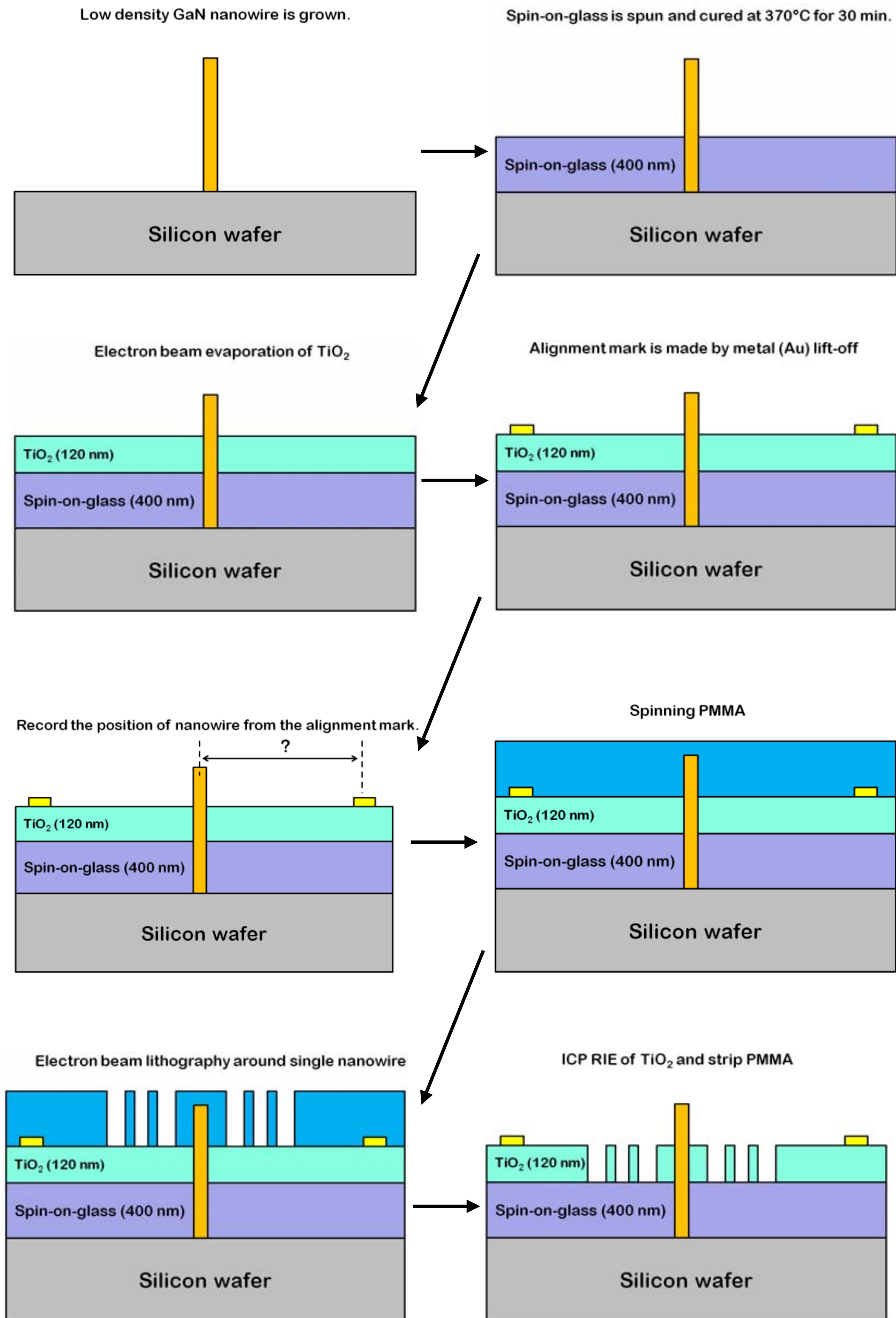

Figure 4.8 Flow chart of device fabrication. Refer to Appendix B for photonic crystal fabrication.

The 2D PC microcavity is fabricated in the TiO_2 layer around the nanowire. Polymethyl methacrylate (PMMA) with a thickness of 300 nm is spin-coated and a 2D PC, consisting of a triangular lattice of air holes with period *a*=120-130 nm and hole diameter *d*=70-80 nm, is patterned by electron beam lithography with an electron energy of 20 keV. The pattern in the PMMA layer is transferred to a TiO_2 layer by inductively coupled plasma reactive ion etching using SF_6, C_4F_8, and Ar gases. PMMA is finally removed using oxygen plasma and acetone. Figure 4.7 shows the fabricated device with a single nanowire aligned in the center of the H2 defect of the PC microcavity. A detail of fabrication flow is shown in Fig. 4.8.

4.5 Device characterization

The device is optically excited at room temperature with a pulsed laser at λ=266 nm with a pulse duration of ~100 fs and a repetition rate of 80 MHz. The pumping laser is focused on the device with an infinity-corrected objective lens (×27) and the emitted light is collected with the same lens. The output spectrum is analyzed with a monochromator (resolution ~0.5 nm) and detected with a photomultiplier tube using phase lock-in amplification. Figure 4.9(a) shows the output spectra recorded for pump power densities of 95 kW/cm^2 (below threshold), 143 kW/cm^2 (slightly above threshold), and 477 kW/cm^2 (above threshold). At low pump power density (~95 kW/cm^2), a broad GaN bandedge emission with a full width at half maximum (FWHM) of ~10 nm is observed, which compares well with the reported linewidth of ~12 nm for GaN bandedge emission [51].

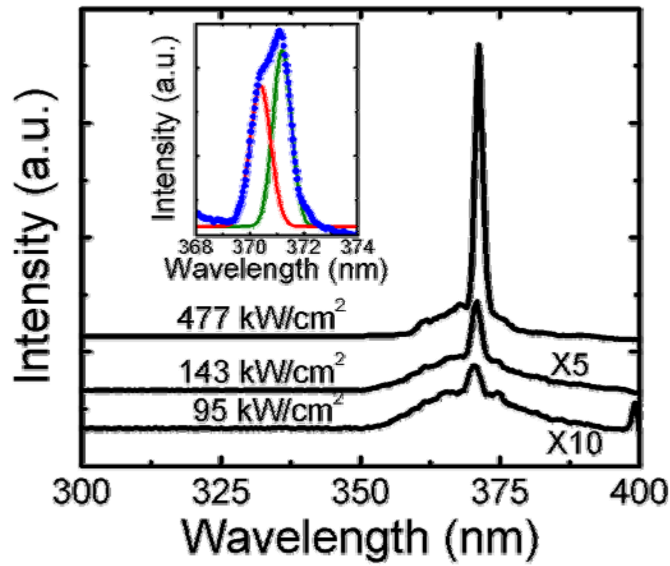

(a)

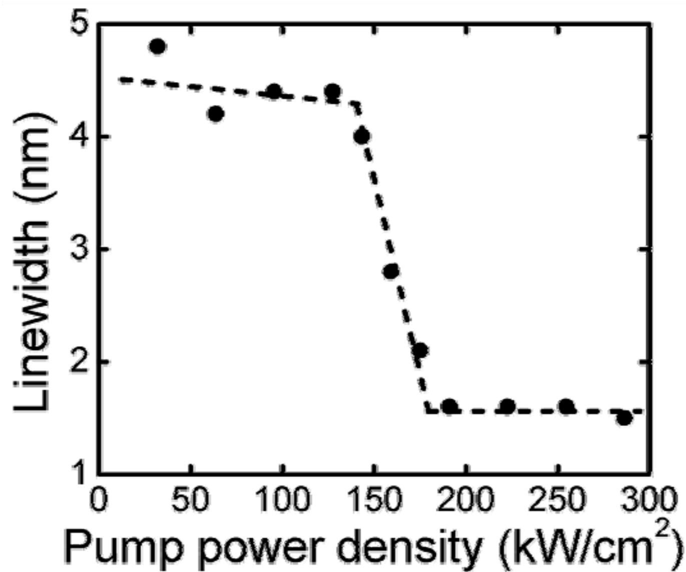

(b)

Figure 4.9 (a) Photoluminescence of the laser at pump power densities of 95 kW/cm^2 (below threshold), 143 kW/cm^2 (near threshold) and 477 kW/cm^2 (above threshold). Spectra are offset for clarity. The inset shows the lasing spectrum (blue circles), which is matched to the sum of two Gaussian peaks (green and red solid lines); (b) measured linewidth of the spectral output as a function of the pump power density. The spontaneous emission linewidth of 4.5 nm decreases sharply at threshold (~120 kW/cm^2) and attains a value of 1.5 nm above threshold.

The output emission also exhibits a fairly narrow peak (~4.5 nm) at λ=370.4 nm which is believed to be due to the Purcell effect which enhances spontaneous emission. The enhanced spontaneous emission peak becomes more pronounced near threshold (120 kW/cm^2) and evolves into a coherent lasing peak above threshold. The spectrum recorded at a high pump power density of 477 kW/cm^2 shows a narrow lasing peak at λ=371.3 nm. This peak is made up of two transitions, indicated by the two Gaussian fitting curves, with the dominant transition having a linewidth of ~0.55 nm limited by the measurement system. The redshift (~0.9 nm) of the peak wavelength is partly due to bandfilling effects and is also due to device heating which causes a redshift of the bandgap energy and an increase of the refractive indices. The variation of measured emission linewidth with pump power is shown in Fig. 4.9(b).

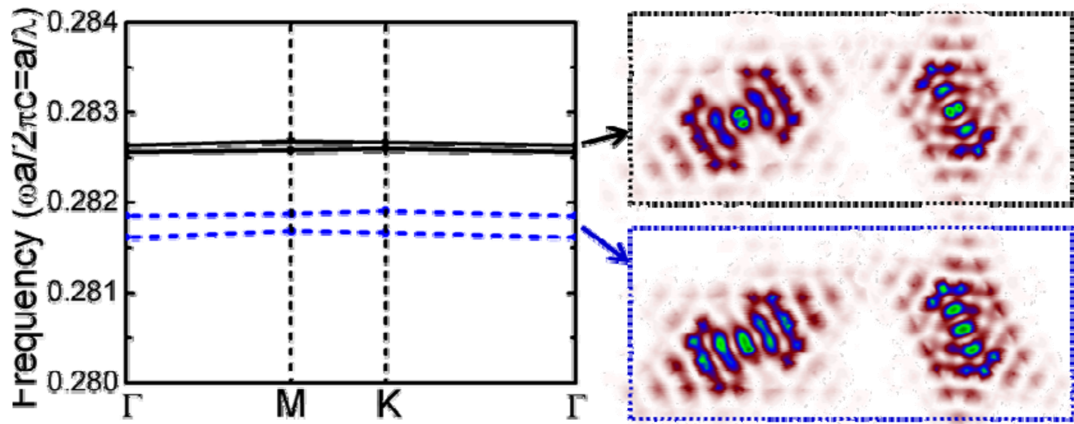

Figure 4.10 Calculated resonant modes with the nanowire in the center (black) and off-center by 60 nm (blue). Mode profiles of each case are shown on the right.

To understand the origin of the dual lasing peaks, the resonant modes were calculated for different positions of the nanowire in the H2 defect. As shown in Fig. 4.10, there are two degenerate modes at a/λ = 0.2826 and 0.28267 (black lines), which are

spectrally very close when the nanowire is placed in the center. As the nanowire is placed off-center in the H2 defect, the two degenerate modes becomes more separated, leading to individual modes at *a*/λ = 0.28167 and 0.28191 (blue lines). We therefore believe that the dual lasing peaks result from a lifting of the degeneracy of the dominant H2 cavity modes due to an off-center positioning of the GaN nanowire within the defect [65].

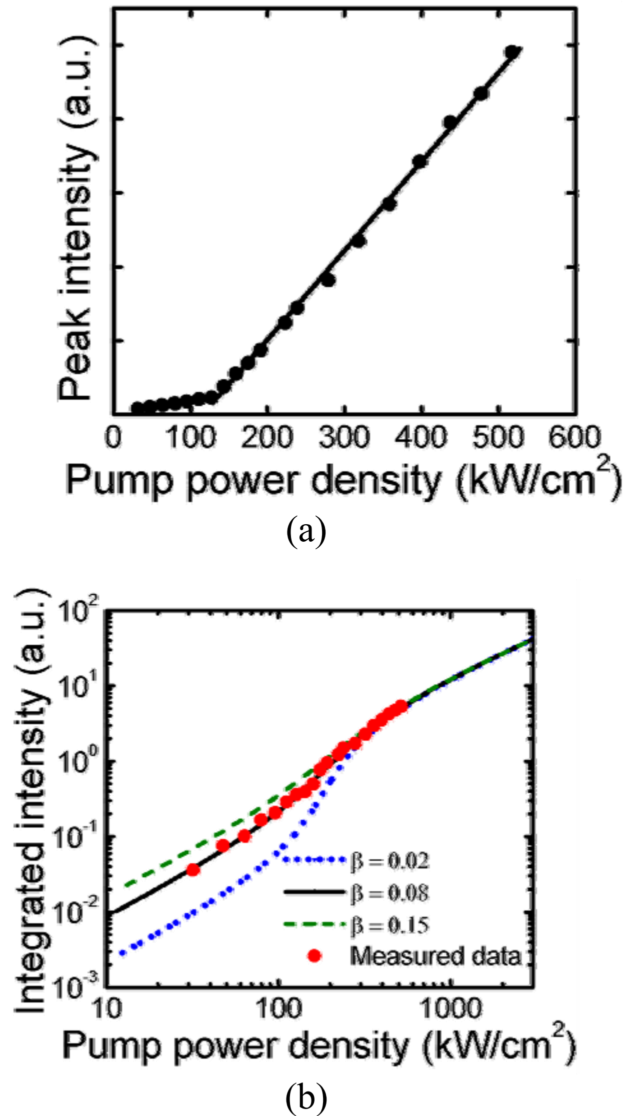

Figure 4.11 (a) Variation of peak output intensity with pump power. The change in slope near threshold (~120 kW/cm^2) is clearly observed; (b) log-log plot of spectrally integrated light intensity (red circles) versus pump power density. Theoretically calculated light intensity using the rate equations is also shown for spontaneous emission factors (β) of 0.02, 0.08, and 0.15.

The measured variation of the peak intensity of the emitted light with pump power density is shown in Fig. 4.11(a). A clear lasing threshold is observed at a pump power density of ~120 kW/cm^2. Calculated plots of emission intensity versus pump power density on a log-log scale are shown in Fig. 4.11(b). Calculations were done for values of the spontaneous emission factor β of 0.02, 0.08 and 0.15 [66]. The material parameters for GaN were obtained from Ref. 32. The optical gain was approximated by a linear model, $g(n)=g_0(n-n_{tr})$, where $g_0=2.5\times10^{-16}$ cm^2 and $n_{tr}=7.5\times10^{18}$ cm^{-3} [67]. The measured integrated emission intensity versus pump power density is also plotted alongside the calculated curves. The best agreement between calculated and measured data is obtained for β=0.08.

4.6 Conclusion

In conclusion, photonic crystal microcavity lasers were fabricated monolithically with a single nanowire on (111) Si using electron beam lithography and standard dry etching techniques. Lasing action was investigated by optical excitation with 100 fs pulses having λ=266 nm. A clear lasing threshold is observed at room temperature both in the variation of emitted light intensity and the spectral linewidth. The threshold power P_{th} is estimated to be 120 kW/cm^2. The spectral linewidth beyond threshold is measured to be 1.5 nm. Analysis of the emission lineshape yields two non-degenerate Gaussian peaks, each having linewidths less than 1 nm. This is believed to be due to a splitting of the doubly degenerated cavity mode caused by slight imperfection in device processing. The value of the spontaneous emission factor β is estimated to be 0.08.

Chapter V

GaN Nanowire Polariton Laser

5.1 Introduction

Two regimes for photon-matter interaction are possible when the emitter is embedded in a microcavity; weak coupling and strong coupling. In the weak coupling regime, the spectral width of the emission can be much narrower than in free space and the spontaneous emission rate can be altered, either enhanced or inhibited (see Appendix A Purcell effect). On the other hand, the strong coupling regime corresponds to an emitter inside a microcavity that is so strongly coupled to the photon modes the normal perturbative approach of Fermi'golden rule which describes the spontaneous emission rate in the weak coupling regime breaks down [68]. Instead we see a new set of energy levels resulting from the mixing of light and matter states.

In detail, when the emitter is placed at the antinodes of the resonant field of the microcavity, the exciton strongly interacts with the confined optical field of the cavity (for more details of excitons, see Appendix C). If the rate of energy exchange between the cavity field and the excitons is much faster than the decay and decoherence rate of both the cavity photons and the excitons, an excitation in the system is stored in the combined system of photons and excitons [69]. Thus, the elementary excitations of the system are no longer excitons or photons but a new type of quasiparticles called the polaritons, which are half-matter and half-light.

Polariton lasers operating in the strong coupling regime utilize the Bose condensation of polaritons induced by quasithermal equilibrium, while normal lasers require the population inversion condition. Therefore, a polariton laser has attracted interest as a promising candidate to realize zero threshold lasing. In this context, strong-coupling effects [69-71] and polariton lasing [72-75] are currently subjects of intense research. Polariton lasing was reported in GaAs-quantum well (QW) microcavities at a threshold density two orders of magnitude lower than that of photon lasing in the same device [73, 76]. GaAs-based polariton systems, however, do not survive at higher temperatures due to the small exciton binding energy and exciton-photon interaction energy of ~10 meV. Candidates for room temperature polariton lasers include systems using III-N [74, 77, 78], ZnSe [79], ZnO [80], or organic molecules [81] as the electronic media. Polariton lasing at room temperature was reported in bulk organic microcavities [75], and in bulk [74] and multiple-quantum-well (QW) [82] GaN microcavities. However, the threshold density in organic cavities is still higher than some competing lasing mechanisms in the device, and in III-nitride microcavities, only modest improvement was obtained compared to weakly-coupled GaN QW devices. Furthermore, in III-nitride bulk-microcavity and QW-microcavity structures, the media and photon coupling is significantly reduced by a large built-in polarization field [83]; the optical quality and reproducibility of the devices are often compromised by relatively large compositional inhomogeneities and structural defects [84].

In this chapter, using a new structure — GaN nanowires — as the active media, a room-temperature polariton laser operating at an energy threshold orders of magnitude lower than before is presented. Remarkably, the nanowires are free of extended defects,

have no alloy fluctuation to introduce inhomogeneous broadening, have a surface recombination velocity ~ 10^3 cm/s, which is two orders of magnitude smaller than that of GaAs, and very small surface depletion and thus are easily reproducible [42, 49, 85-88]. It has been seen experimentally that the polarization field in the nanowires is negligible [89] and the internal quantum efficieny is ~ 50-60%. A single nanowire was enclosed in a dielectric microcavity. The characteristic polariton dispersions were measured by angle-resolved photoluminescence. The linewidth narrowing and energy shift of the lasing mode, population redistribution in the momentum space, and coherence functions of the polariton laser were studied. A second threshold, corresponding to photon lasing with an inverted carrier population, was observed at 2700 times the polariton lasing threshold.

5.2 Strong coupling

The linear Hamiltonian of the emitter-microcavity system in strong coupling regime is described in the second quantization form [69]

$$\hat{H}_{pol} = \hat{H}_{cav} + \hat{H}_{exc} + \hat{H}_I \tag{5.1a}$$

$$\hat{H}_I = \sum g_0 \left(\hat{a}^+_{k_{//}} \hat{b}_{k_{//}} + \hat{a}_{k_{//}} \hat{b}^+_{k_{//}} \right) \tag{5.1b}$$

$\hat{a}^+_{k_{//}}$ is the photon creation operator and $\hat{b}^+_{k_{//}}$ is the exciton creation operators with an in-plane wave number $k_{//}$. g_0 is the exciton-photon dipole interaction strength. It is nonzero only between modes with the same $k_{//}$. g_0 is often called the coupling constant since it is the most critical component which determines the degree of coupling between excitons and cavity fields, and is given by Eqn. (5.2).

$$g = \left(\frac{1}{4\pi\varepsilon_r\varepsilon_0} \frac{\pi e^2 f}{m_0 V_m} \right)^{1/2} \tag{5.2}$$

m_0 is free electron mass and V_m is mode volume. f is the oscillator strength and described in Appendix C.

The energies of the polaritons, which are the eigenenergies of the Hamiltonian, are deduced from the diagonalization procedure [69].

$$E_{LP,UP}(k_{//}) = \frac{1}{2}\left[E_{exc} + E_{cav} \pm \sqrt{4g_0^2 + (E_{exc} - E_{cav})^2} \right] \tag{5.3}$$

When the exciton and photon are at the same energy, energies of lower polariton (LP) and upper polariton (UP) have the minimum separation, $2g_0$, which is often called the normal-mode splitting. When the cavity energy is tuned across the exciton energy, the new polariton energies anticross as shown in Fig. 5.1. This is one of the signatures of *strong coupling*.

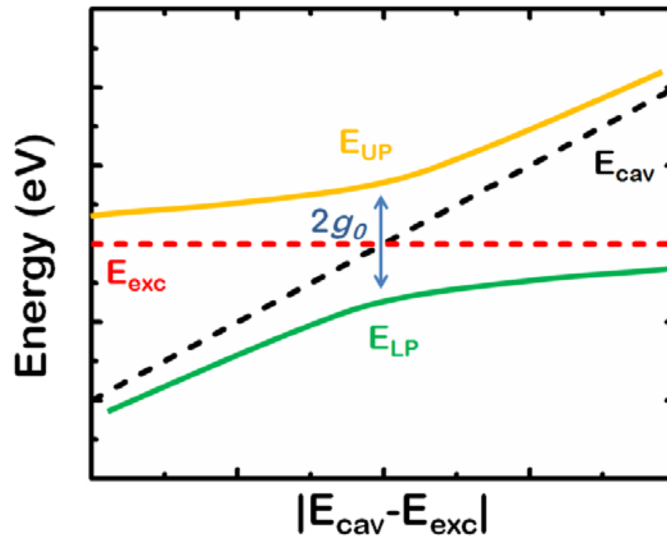

Figure 5.1 Anticrossing of lower and upper polariton energy levels when tuning the cavity energy across the exciton energy.

When taking into account the finite lifetime of the cavity photon and exciton, the eigenenergy give in Eqn. (5.3) is modified.

$$E_{LP,UP}(k_{//}) = \frac{1}{2}\left[E_{exc} + E_{cav} + i(\gamma_{exc} + \gamma_{cav}) \pm \sqrt{4g_0^2 + [E_{exc} - E_{cav} + i(\gamma_{exc} + \gamma_{cav})]^2}\right] \quad (5.4)$$

γ_{exc} is the nonradiative decay rate of an exciton and γ_{cav} is the mirror loss of a cavity photon. Thus the coupling strength must be larger than half of the difference in decay rates to have polaritons as the new eigenmodes, which is the condition for the strong coupling regime (Eqn. 5.5).

$$g_0 >> \frac{(\gamma_{exc} - \gamma_{cav})}{2} \quad (5.5)$$

In order to attain a strong coupling, a photon and an exciton must exchange the energy coherently at least once. When the system does not satisfy the condition given in Eqn (5.5), excitons and photons are the eigenmodes and the system is said to be in the weak coupling regime.

5.3 Device design and fabrication

The GaN nanowire-microcavity used in this study is shown schematically in Fig. 5.2(a). It consists of a SiO_2 λ−cavity sandwiched by a top and a bottom DBR made of 7 pairs of SiO_2/TiO_2. A single nanowire is placed at the central antinode of the cavity field to maximize the interaction between the GaN nanowire excitons and the cavity mode. The inset to Fig. 5.2(a) shows the scanning electron microscope (SEM) image of the nanowire lying on the half cavity, before the top cavity was deposited. The wire has a diameter of ∼60 nm and a length of ∼750 nm. The nanowire diameter corresponds to the total thickness of 50 quantum wells used in similar devices [82]. A low background

carrier concentration of 8.5 x 10^{16} cm^{-3} was derived from measurements made on Pt-GaN nanowire Schottky diodes [86].

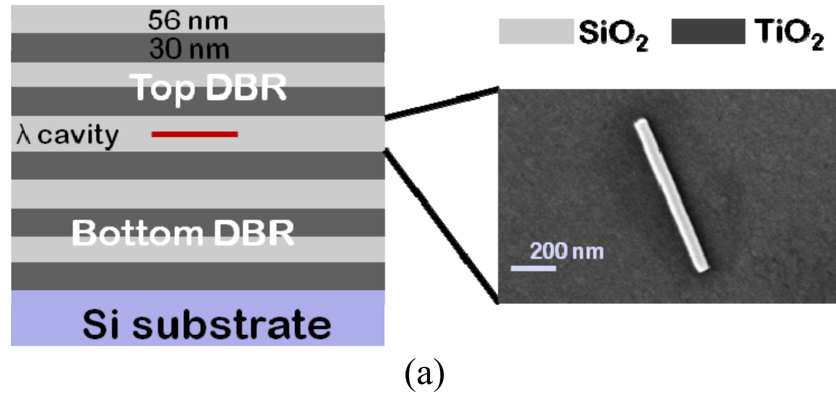

(a)

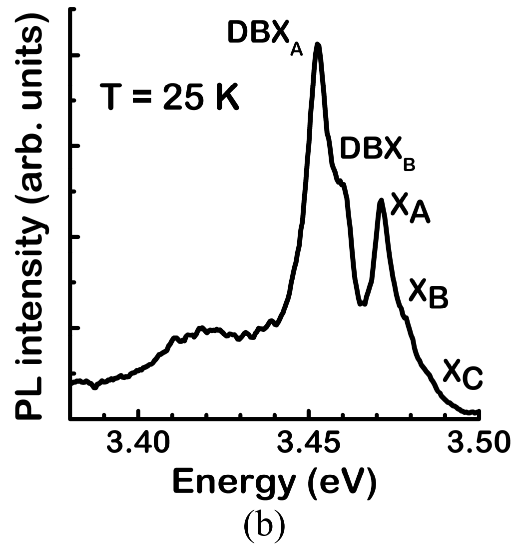

(b)

Figure 5.2 (a) Schematic representation of the dielectric microcavity with a single GaN nanowire of diameter 60 nm (inset) buried in the center of a λ-sized cavity; (b) photoluminescence spectrum from a single GaN nanowire measured at 25K showing free and bound exciton transitions.

A photoluminescence (PL) spectrum of the nanowires at 25 K is shown in Fig 5.2(b). The three free exciton transitions, $X_{A,B,C}$, corresponding to the wurtzite crystalline structure are indicated. The peaks labelled DBX_A and DBX_B are bound exciton transitions. The broad and weak transition at ~ 3.41 eV is related to the surface [86]. The

lineshape of the exciton transitions resembles a Lorentzian function instead of a Gaussian function, suggesting negligible inhomogeneous broadening of the exciton resonances in the nanowires.

To isolate a single nanowire, grid masks with alignment marks are prepared for the sample and a single nanowire is located by SEM with respect to the alignment marks. The top DBR is deposited and 5 μm mesas centered about the single nanowires are etched down to complete the microcavity. Two devices, fabricated from different samples of GaN nanowires with different cavity-exciton detunings were studied. The measured results are qualititively similar and in the following I present the sample which is negatively detuned at 300K.

5.4 Dispersion of polaritons

The planar DBR cavity confines the photon field in the *z*-direction but not in the *x-y* plane. The collected light from a tilted angle θ relative to the *z* axis has a resonance at $\lambda_c/cos\theta$. As a result, the cavity has an energy dispersion versus the in-plane wave number $k_{||}$.

$$E_{cav} = \frac{\hbar c}{n_c}\sqrt{k_\perp^2 + k_{||}^2} \qquad \text{where } k_\perp = n_c(2\pi/\lambda_c) \tag{5.6}$$

There is also one-to-one correspondence between the incidence angle θ and each resonance mode with in-plane wave number $k_{||}$.

$$k_{||} = n_c \frac{2\pi}{\lambda_c} \tan\left[\sin^{-1}\left(\frac{\sin\theta}{n_c}\right)\right] \approx \frac{2\pi}{\lambda_c}\theta \qquad \text{when } k_{||} << k_\perp \tag{5.7}$$

Thus, angle-resolved photoluminescence is an indirect way to probe the dispersion of the resonance modes.

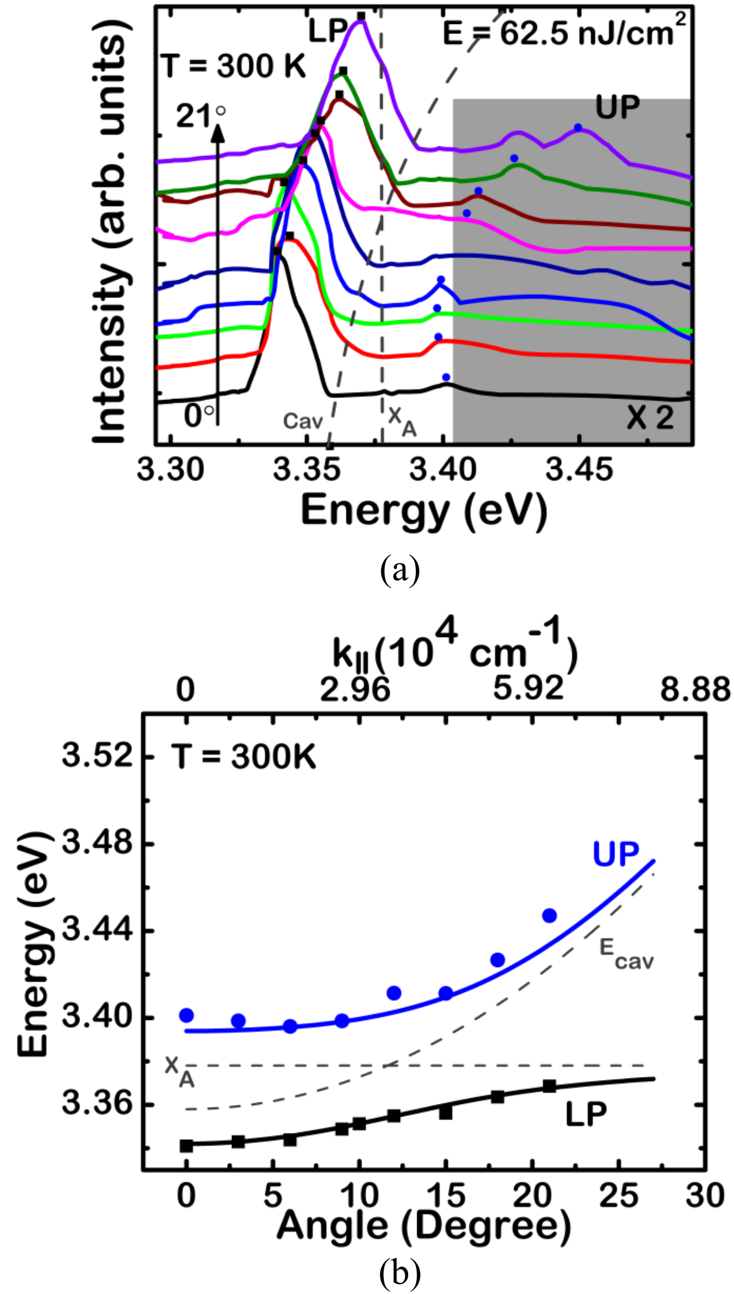

Figure 5.3 (a) Angle-resolved photoluminescence measured at room temperature; (b) polariton dispersion curves obtained from the data of (a). The solid curves indicate the calculated polariton dispersion from a coupled harmonic oscillator model.

Figure 5.3(a) shows the dispersion of the resonant modes measured at 300 K by angle-resolved photoluminescence and the spectra. A peak below the exciton resonances is clearly observed in the spectra, which asymptotically approaches the X_A exciton energy at larger angles. A weaker peak above the exciton resonances can also be identified, and the two peaks anti-cross with increasing angle. Using the one-to-one correspondence between the angle of the out-coupled photon and the in-plane wavenumber of the polaritons, we obtained the energy-momentum dispersion of the resonances (Fig. 5.3(b)). The results are well described by the polariton dispersions calculated by the coupled oscillator model (as shown by the solid curves). Here we only consider the coupling of X_A exciton and the cavity mode, because the X_B and X_C excitons have much weaker oscillator strengths according to PL measurements.

The cavity to exciton detuning δ and photon-exciton interaction potential V_A are obtained by fitting the data and are found to be δ= -20 meV and V_A = 48 meV for the X_A exciton. The exciton linewidth without thermal broadening used in the Hamiltonian is Γ_{XA} = 4.5 meV and is obtained from independent photoluminescence measurement on a single GaN nanowire at 25 K. The relatively large value of V_A for a single nanowire is due to both the large oscillator strength of excitons resulting from a small internal electric field of ~0.19 MV/cm [49, 88, 89], and a modified cavity field that concentrates within the nanowire. Since the refractive index of the nanowire is higher than that of the cavity, the cavity field is mainly within the nanowire region even without additional transverse confinement of the cavity mode, as shown in the FDTD simulation (Fig. 5.4). The polarization field in a bulk GaN microcavity is calculated to be ~ 1 MV/cm for a reported compressive stress of 30 kBar [79]. The oscillator strength in the single nanowire is

therefore approximately twice than in the bulk microcavity and the interaction potential V_A is expected to be ~ 44 meV compared to the bulk value of 31 meV [79].

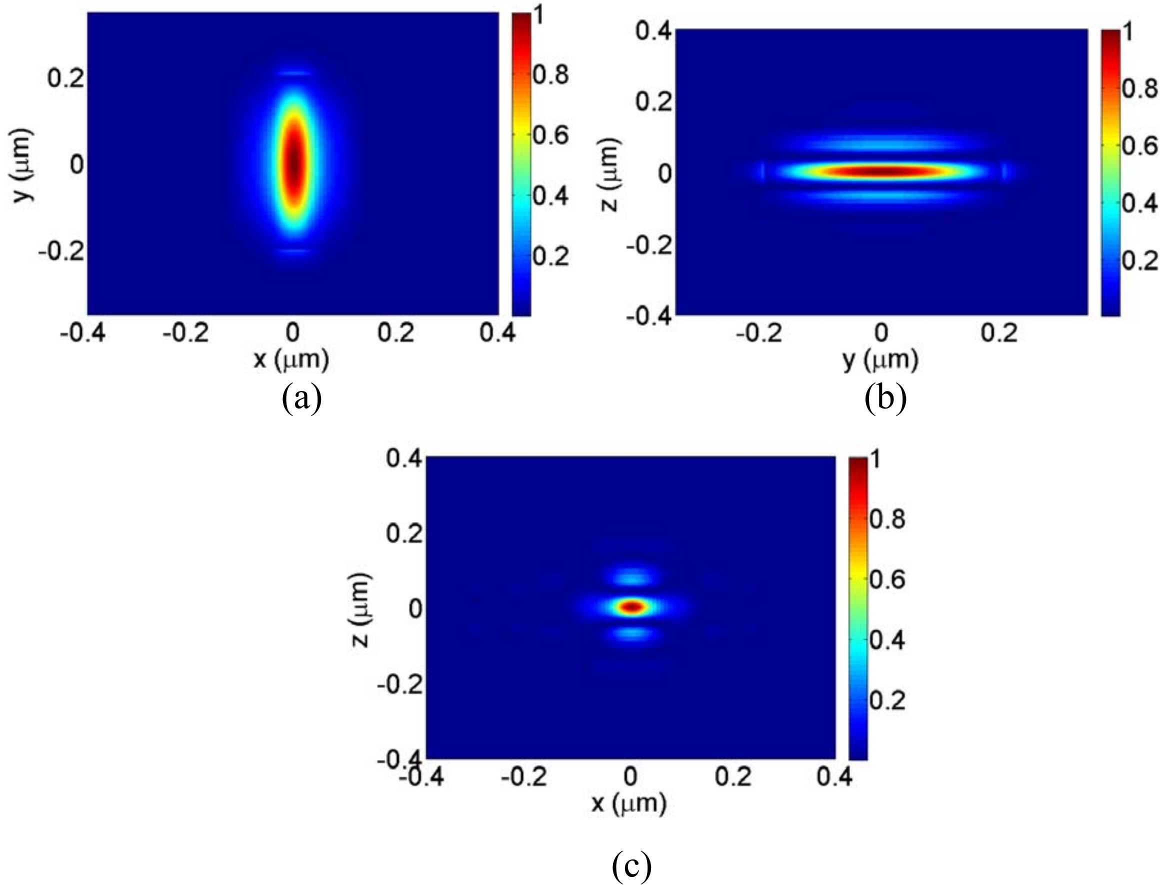

Figure 5.4 The calculated electric field intensity distribution of the fundamental resonance mode around the nanowire embedded in a 5 μm diameter pillar cavity. Cross-sectional profiles of the electrical field intensity along the *x*, *y* and *z* directions. The *y* direction is defined to be along the length of the nanowire. The *z* direction is in the cavity growth direction. The origin is at the center of the nanowire.

5.5 Nonlinear optical characteristics

To investigate the non-linear optical properties of the nanowire microcavities, the device was pumped non-resonantly with a frequency-tripled Ti-Sapphire laser focused to a spot size of ∼100μm in diameter. Photoluminescence from the normal direction was

analyzed with a high resolution monochromator, and detected with a photomultiplier tube using phase-sensitive lock-in amplification.

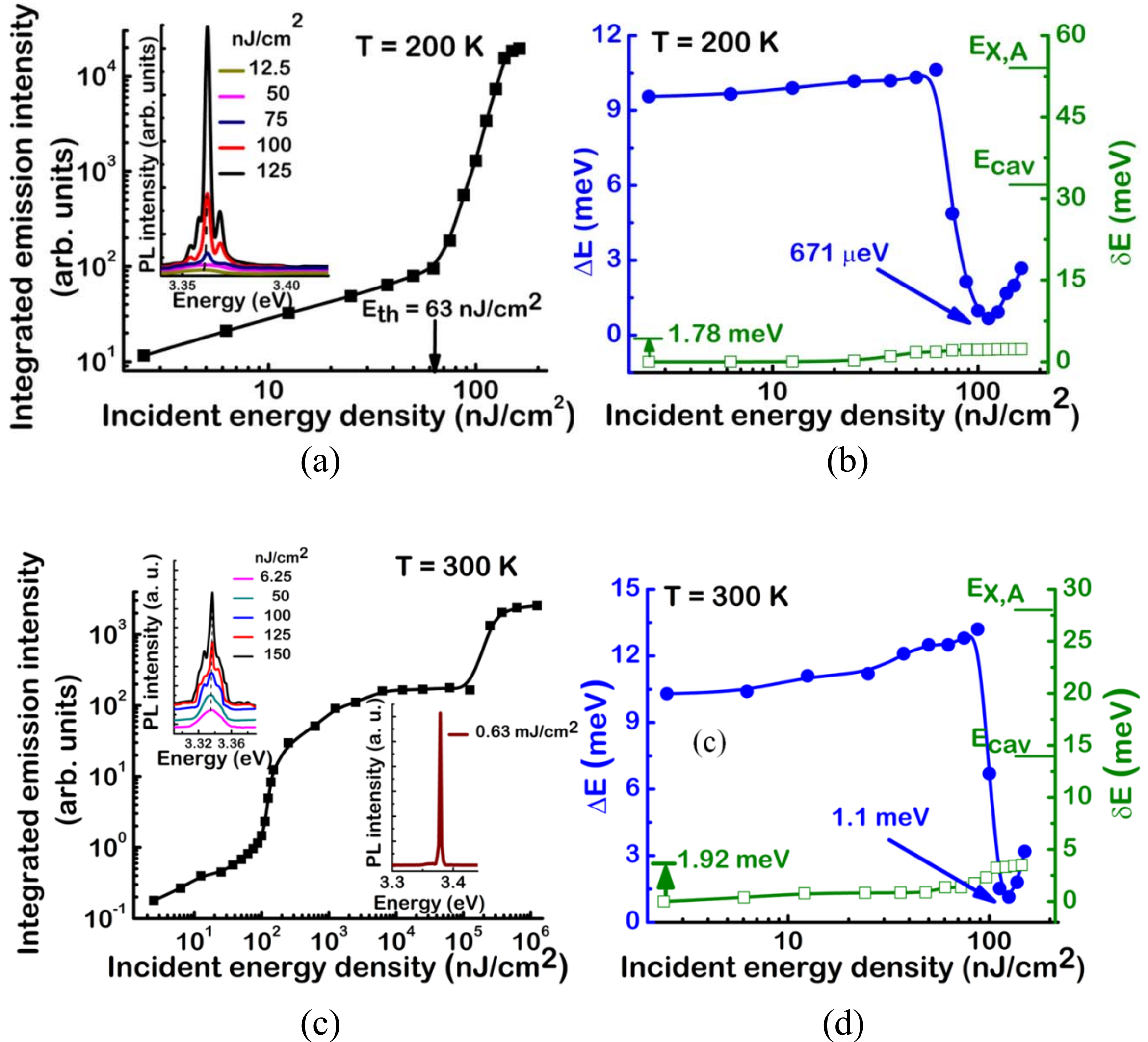

Figure 5.5 (a) Measured polariton emission intensity at 200K as a function of incident optical excitation energy showing strong non-linearity at threshold. The inset shows the emission spectra; (b) variation of the emission linewidth and peak energy corresponding to the data in (a); (c) variation of the emission intensity with excitation energy at 300K clearly showing the two thresholds for polariton and photon lasing. The insets show the corresponding emission spectra; (d) variation of linewidth and emission energy at 300K for polariton lasing.

With increasing pumping power, a sharp super-linear increase of the PL intensity from lower polaritons (LPs) at $k_{||}$~0 was observed at both 200 and 300K (Fig. 5.5), accompanied by a sharp decrease in the emission linewidth and a small blueshift of the LP energy. Both features indicate the onset of stimulated scattering into the LP states near $k_{||}$=0. The incident excitation energy at threshold was E_{th1} = 92.5 nJ/cm^2 at 300 K and 63 nJ/cm^2 at 200 K. We estimate an upper bound of the LP density at the threshold to be $N_{LP}(E_{th1}) = 2x10^{16}$ cm^{-3} , using the relation $N_{3D} < E_{th1}/(E_{pump}D)$. The LP density at the threshold, $N_{LP}(E_{th1})$, is two orders of magnitude lower than any previously reported GaN polariton lasers, and three orders of magnitude less than the exciton Mott density of 3x10^{19} cm^{-3}, [90] the latter corresponding to the required carrier density for conventional photon lasing.

Remarkably, the gain media in our device is a single nanowire with the lateral size of ~0.045 μm^2, which is orders of magnitude smaller than the optical excitation spot size used in these measurements. Therefore the nanowire-microcavity device can allow further reduction in the threshold energy with electrical injection. Above threshold, the emission spectra showed multiple peaks with greatly reduced linewidths, corresponding to different transverse modes of the LPs due to localization of the LP modes by the nanowires. Similar multi-mode lasing has been observed in bulk [74] and multiple-QW [82] GaN microcavities, where the localization was attributed to photonic disorders in the structures, and the modes varied with spatial alignment of the pump with the sample. In contrast, in our device, the modes are intrinsic to the nanowire-microcavity. They are not due to crystal defects and do not depend on the spatial alignment of the pump. Below threshold, the modes are indistinguishable due to a thermally broadened linewidth of

>10 meV. At threshold, the linewidths are greatly reduced to a mere 0.67 meV at 200K and 1.1 meV at 300K, and thus revealing the discrete modes in the spectra. The reduction in linewidth indicates the increase in the coherence time of the LPs in the lasing mode to 6.2 ps at 200K and 3.8 ps at 300K. Identical polariton lasing characteristics were observed for the second device at 80K (Fig. 5.6).

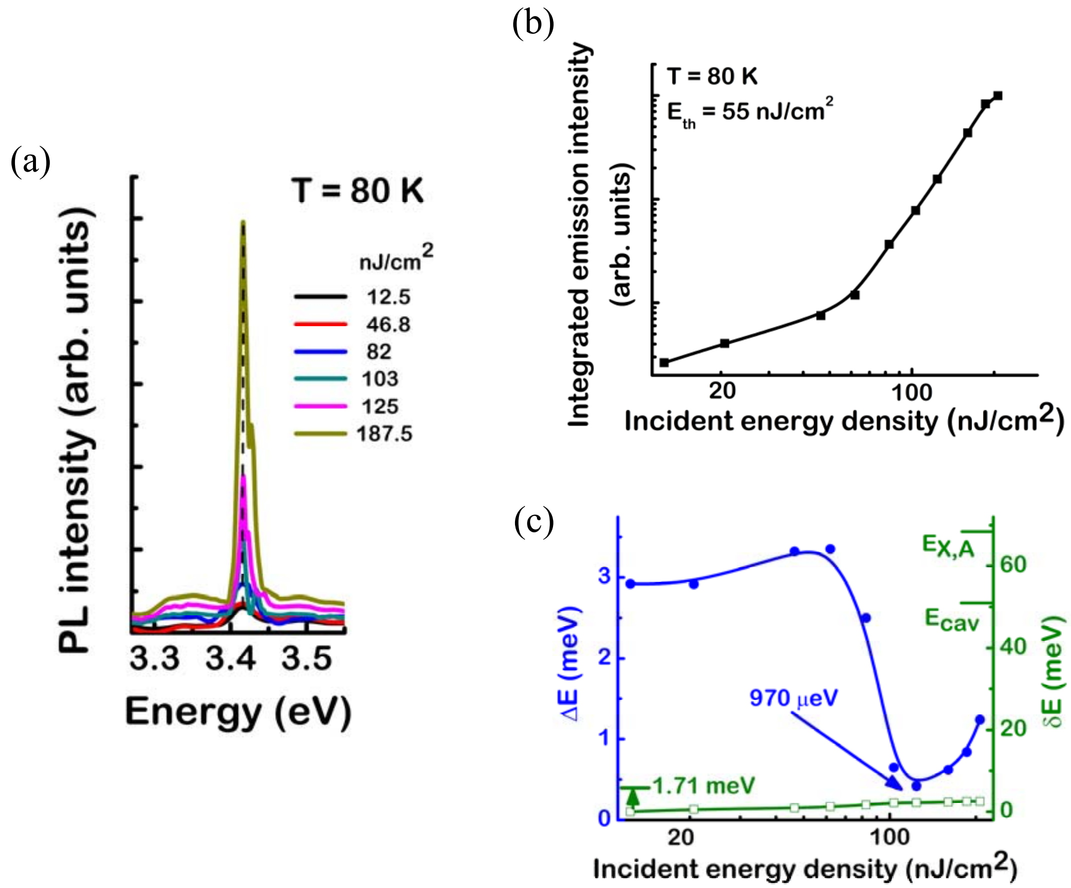

Figure 5.6 (a) Photoluminescence spectra measured from the second device as a function of incident pump density at zero detection angle at 80 K; (b) corresponding variation of integrated emission intensity; (c) linewidth and blueshift with incident pump density. A threshold is observed at 63 nJ/cm^2 and a minimum full-width half maximum linewidth of 0.97 meV is measured, corresponding to a coherence time of 4.8 ps.

A small blueshift δE of the LP emission was observed with increasing pump power up to δE~1.78 meV (200K)and 1.92 meV (300K) around the threshold. Further increasing excitation density above threshold led to only negligible change in δE until exciton saturation sets in at much higher pump powers. The behavior is typical in polariton lasers. The blueshift is caused by repulsive self-interaction of the exciton-polaritons and the resultant renormalization of the exciton self energy [91]. From the blueshift, the exciton-polariton population N_{3D} may be estimated using $\delta E \approx 3.3\pi E_X^B a_B^3 N_{3D}$, [74] where E_X^B = 30 meV is the X_A exciton binding energy and a_B = 3.5 nm is the exciton Bohr radius. We found $N_{3D} = 1.43 \times 10^{17}$ cm^{-3} at threshold. This value is a factor of 7 larger than that estimated from the incident excitation energy, which could be due to a couple of reasons. The first is the spread of values of a_B for GaN quoted in the literature. Second, the exciton population introduces both phase space filling and a saturation of the oscillator strength, both resulting in a blueshift of the lower polariton energy. The formula quoted above is based on phase space filling only. Hence the exciton population calculated based on the total measured blueshift is higher than the actual exciton population.

With further increase of excitation density (by using an objective lens and spot size of ~ 10 μm) to $(10^2\text{-}10^3)E_{th1}$, the emission becomes strongly blueshifted and broadened (see supplementary information), indicating exciton saturation and transition to the weak coupling regime [76]. A second distinct threshold was observed at $E_{th2} \approx 2700E_{th1}$ = 250 μJ/cm^2, which correspond to a population slightly higher than the Mott density and represents the onset of photon lasing. The integrated emission intensity over the entire range of excitation power density is shown in Fig. 5.5(c). The two distinct

thresholds, three orders of magnitude apart in excitation density, are strong evidence of the very different origin of the nonlinear emissions. Polariton lasing results from stimulated scattering of polaritons into the quantum degenerate polariton states at $k_{||} \sim 0$, without requiring population inversion. Photon lasing results from stimulated emission into the cavity modes upon population inversion in the electronic media.

To confirm the physical mechanism for the first nonlinear threshold, we measured the LP population distribution in k-space by angle-resolved photoluminescence. Figure 5.7 shows the spectra of angle-resolved PL between 0° and 27° at 300 K, both below (a) and above (b) threshold. There is no obvious energy-relaxation bottleneck at all excitation densities. Below threshold, emission intensities are comparable at different angles. Above threshold, the emission becomes sharply peaked at small angles, showing condensation in k-space. The number of polaritons per $k_{||}$ state is estimated from the PL intensity by taking into account the radiative lifetime of polaritons (The occupation number ($N_{LP}(k_{||})$) is calculated from the intensity ($I_{LP}(k_{||})$) by using the formula, $I_{LP}(k_{||}) = \eta N_{LP}(k_{||})\left|C(k_{||})\right|^2 M/\tau_C$, where η is the collection efficiency, $\tau_C/\ |C(k_{||})|^2$ is the radiative lifetime of the LPs and M is the number of transverse states subtended by the detection cone.) [92] and is shown in Fig. 5.8. As can be seen again that below threshold the distribution is random where as above threhold there is a sharp increase in the occupancy near $k_{||} \sim 0$ states.

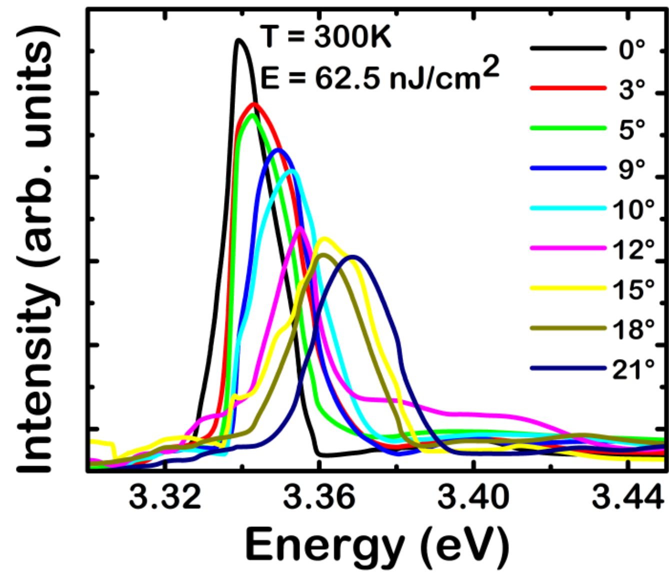

(a)

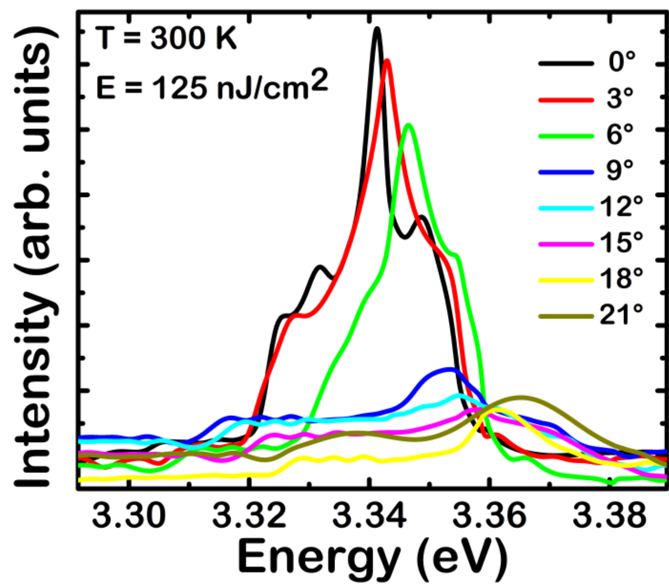

(b)

Figure 5.7 Angle resolved lower polariton luminescence spectra measured at 300K (a) below and (b) above the polariton lasing threshold.

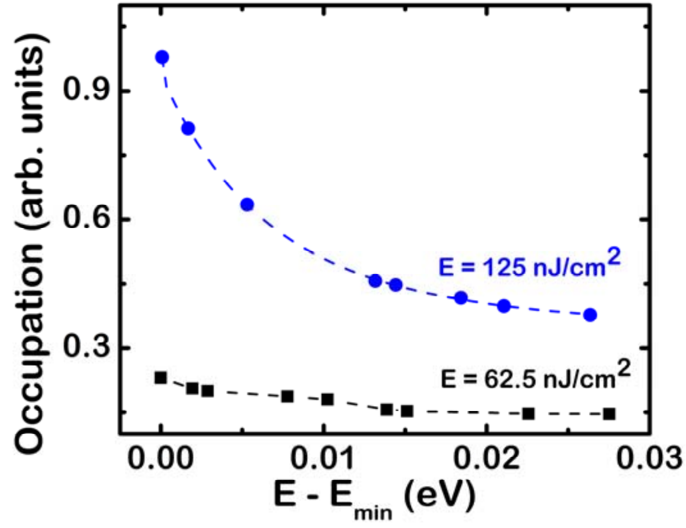

Figure 5.8 Polariton occupancy for different $k_{||}$ states deduced from the data of Fig. 5.7.

Coherence properties of the emission below and above E_{th1} were also studied and the measured data are shown in the supplementary document. The first order coherence was measured with a Michelson interferometer using pulsed excitation. Below threshold, the interference fringe contrast has a noise limited value of ~ 2.5% and it increased to a value of ~ 32% at threshold (92.5 nJ/cm^2). The second order coherence function in time domain was measured as a function of incident excitation energy by a Hanbury-Brown and Twiss type measurement system. Similar results as reported by Kasprzak et al [93] were obtained.

5.6 Conclusion

In conclusion, room temperature polariton lasing at record low threshold polariton densities was achieved in a vertical microcavity containing a single GaN nanowire. The threshold density was two orders of magnitude lower than reported values for GaN-based

polariton lasers. Dynamic and coherence properties of the device suggest that the low-threshold lasing results from stimulated scattering and accumulation of a quantum degenerate polariton population near the band minimum. In comparison, a second threshold corresponding to conventional photon lasing was also observed at a density 2700 times the polariton lasing threshold density. Reducing the lateral size of the microcavity would increase the photon-exciton coupling and further improve the optical qualities of the polariton laser. Our work represents a first step in developing a new generation of ultra-low power and ultra-compact, room-temperature photonic devices based on GaN nanowire polaritons.

Chapter VI

Rolled-up Microtube Laser with InAs Quantum Dots

6.1 Introduction

One emerging technique for fabricating a single crystalline semiconductor microtube is to use the strain-driven self-rolling mechanism. A pseudomorphically strained epitaxial layer is rolled into micro or nanotubes through a controlled release from their host substrates by selective etching, which occurs due to the minimization of the elastic energy [94]. Since the first demonstration by Prinz *et. al.* [94], such microtubes have been realized using GaAs, SiGe, and SiO/SiO_2 based materials and have been designed as nanoreactors, nanopipelines, injection needles, and optical resonators [95, 96].

The formation of an InGaAs/GaAs microtube structure grown on GaAs, illustrated in Figs. 6.1(a) and (b), is initiated and controlled by selective removal of the underlying AlAs sacrificial layer. The optical microscopy image of a rolled InGaAs/GaAs microtube is illustrated in Fig. 6.1(c). The tube diameter is determined by the strain of the InGaAs/GaAs heterostructure, and the tube wall thickness is directly related to the thickness of the bilayer as well as the number of revolutions. Combining the advantages of both top-down and bottom-up fabrication processes, this unique approach offers an exceptional flexibility for achieving semiconductor microtube structures with wall thicknesses ranging from a few nanometers to a few microns and diameters varying from ~10 nm to ~100 microns using standard photolithography process.

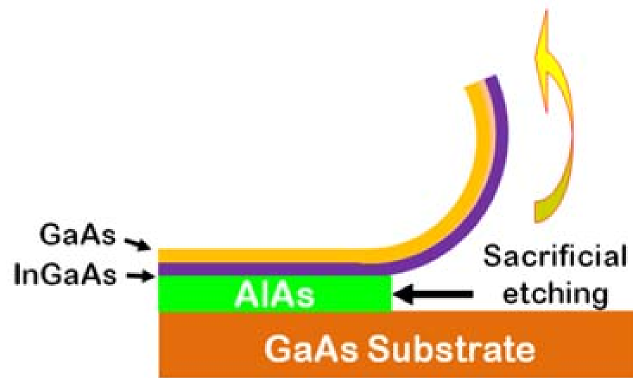

(a)

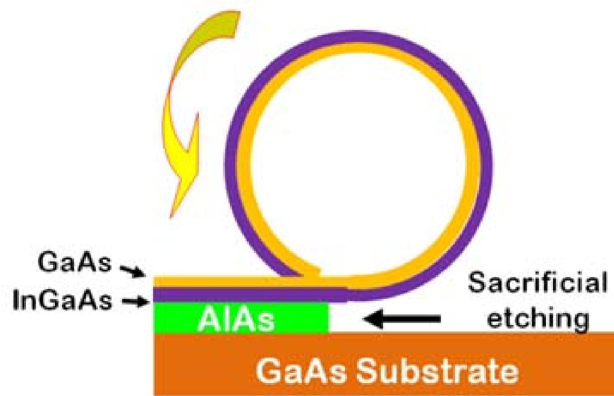

(b)

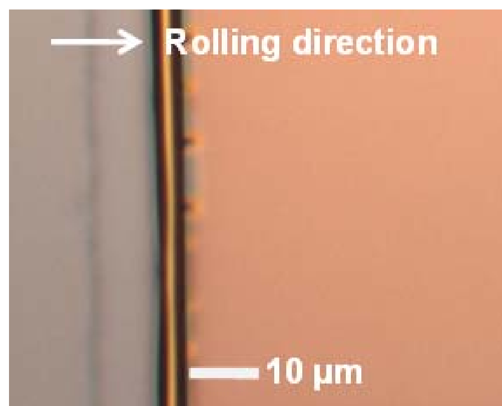

(c)

Figure 6.1 (a) and (b) Illustrations of the formation of InGaAs/GaAs microtube structures on GaAs; (c) Optical microscopy image of an InGaAs/GaAs microtube formed on GaAs.

Of both fundamental and practical interest is the incorporation of self-organized quantum dots or quantum wells in the GaAs microtube structures, wherein controllable strong coupling between the dots/wells and whispering-gallery modes can potentially be achieved. Compared to many conventional optical microresonators, such quantum dot microtubes exhibit a number of distinct characteristics, including epitaxially smooth surface, photolithographically definable surface geometry, extremely small mode volume, and a near perfect overlap between the maximum optical field intensity and the dot layers, thereby promising a new generation of nanophotonic devices. Recent studies also suggest that the confined optical modes preferentially emit from the inside notch of the tube, which may lead to nanoscale lasers with directional emission [97].

6.2 Design of free standing rolled-up microtube cavity

Free standing optically pumped microtube cavity based on GaAs was investigated in this study. The heterostructure of the device before the formation of the microtube is shown in Fig. 6.2(a). The pseudomorphically strained multilayer, where two layers of InAs/GaAs quantum dots are buried in a GaAs matrix, is grown on a 50 nm AlAs sacrificial layer on a GaAs substrate by molecular beam epitaxy (MBE). A strained U-shaped mesa, illustrated in Fig. 6.2(b), is first defined by etching down to the InGaAs layer. The AlAs sacrificial layer is etched at the starting edge of the rolled-up microtube. The self-rolling process is initiated with the selective etching of the AlAs sacrificial layer using hydrofluoric (HF) acid based solutions. After a certain distance, the middle part of the tube is separated from the substrate and, as a result, free-standing microtubes are formed, illustrated in Fig. 6.2(c).

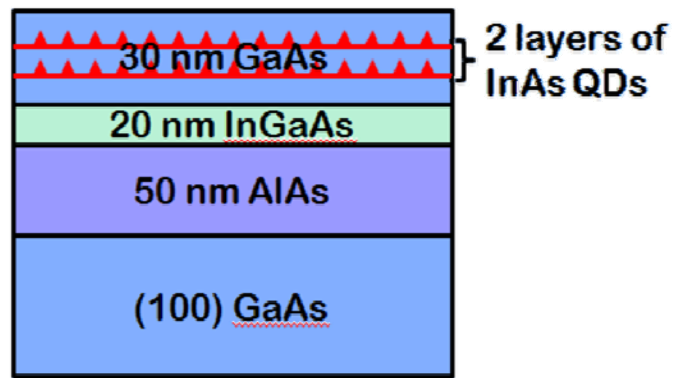

(a)

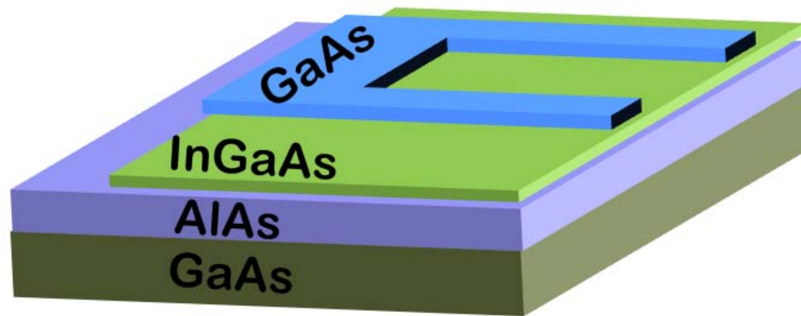

(b)

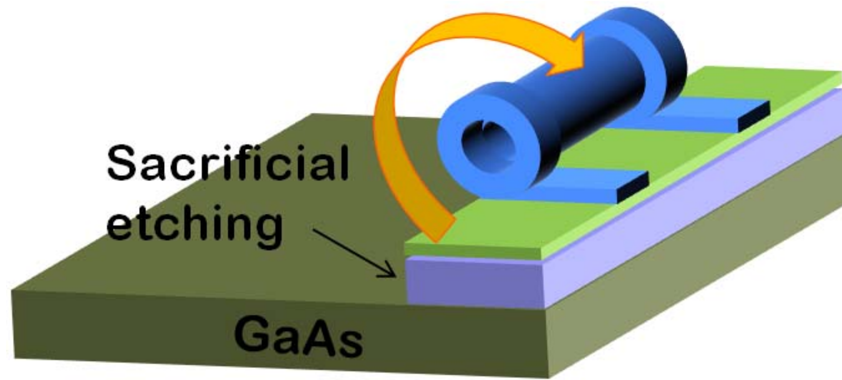

(c)

Figure 6.2 (a) Device heterostructure. InAs quantum dots are buried in a GaAs matrix grown on an InGaAs strained layer and AlAs sacrificial layer; (b) and (c) illustration of the formation of free-standing quantum dot microtubes on GaAs substrates.

6.3 Surface passivation of GaAs

Because of high surface-to-volume ratio due to the thin walls of the microtube and a large surface recombination velocity in GaAs, the elimination of non-radiative recombination at surface states is necessarily required to achieve room temperature operation.

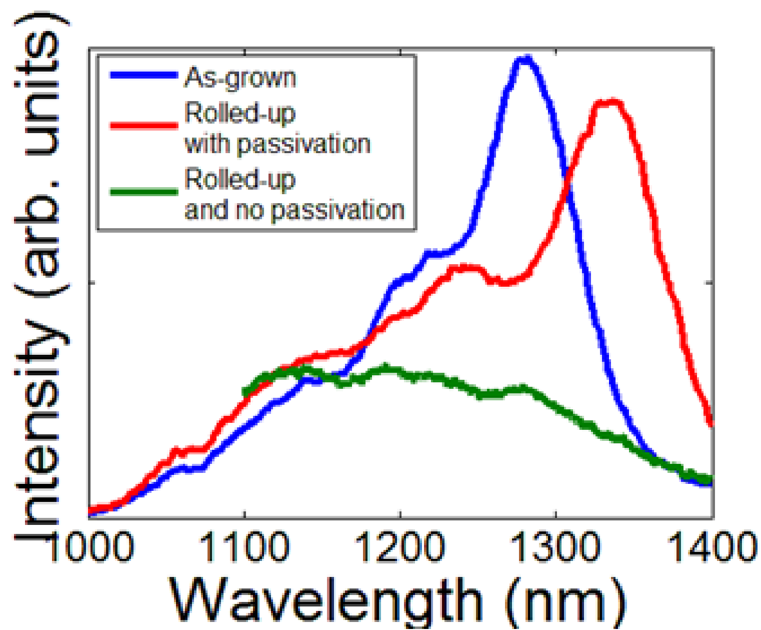

Figure 6.3 The photoluminescence intensity comparison between thin GaAs with and without surface passivation using an ammonium sulfide solution.

Surface oxide layers are rapidly formed due to oxygen present in air. Some surface defects are induced by oxygen chemisorption on the GaAs. Surface defects degrade the efficiency of luminescent intensity by acting as surface states, i.e. non-radiative recombination centers. A high density of surface states could also cause the surface Fermi level in GaAs to be pinned near the midgap. To prevent surface defects and minimize surface oxides, surface passivation by other species of atoms are required. Hence, the surface passivation technique with an ammonium sulfide solution was

investigated [98]. Before and after microtubes are formed, native oxides on GaAs are removed by dilute hydrochloric acid ($HCl : H_2O = 1 : 1$). Samples are then rinsed and stored in deionized (DI) water before they are soaked in an ammonium sulfide solution for 10 mins. As shown in Fig. 6.3, the emission intensity from the sample with passivation does not degrade while the sample without passivation shows very weak photoluminescence (PL) intensity. The red shift of the PL peak observed is caused by the reduced strain due to formation of the microtube.

6.4 Device characterization

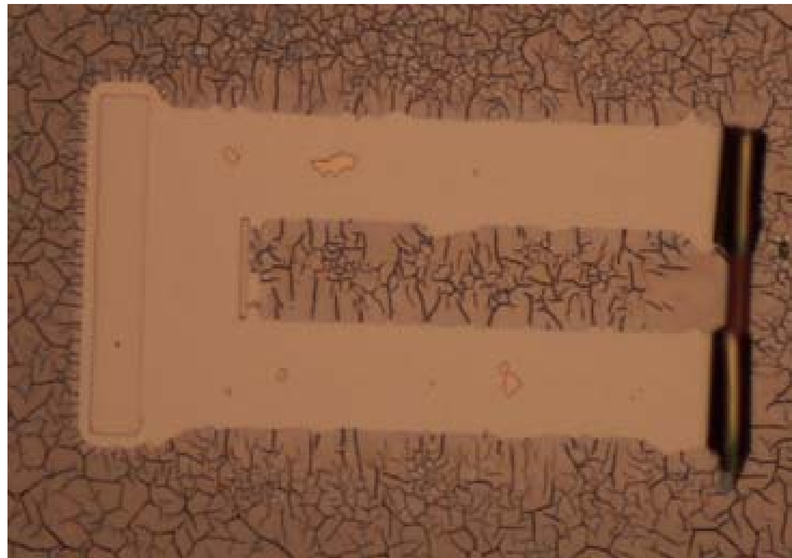

Figure 6.4 The microscopy image of the fabricated device. The tube is separated from the GaAs substrate by 400 nm.

Fig. 6.4 shows a microscopy image of a fabricated free-standing InGaAs quantum dot microtube device. The air-gap between the tube and the GaAs substrate is estimated to be about 0.4 μm based on the number of revolutions. It is also evident that the positions of the free-standing microtubes, as well as their separation from the substrate,

can be precisely controlled by the U-shaped mesa and the etching time. The radius of the microtube is about 3 μm and the wall thickness is ~100 nm.

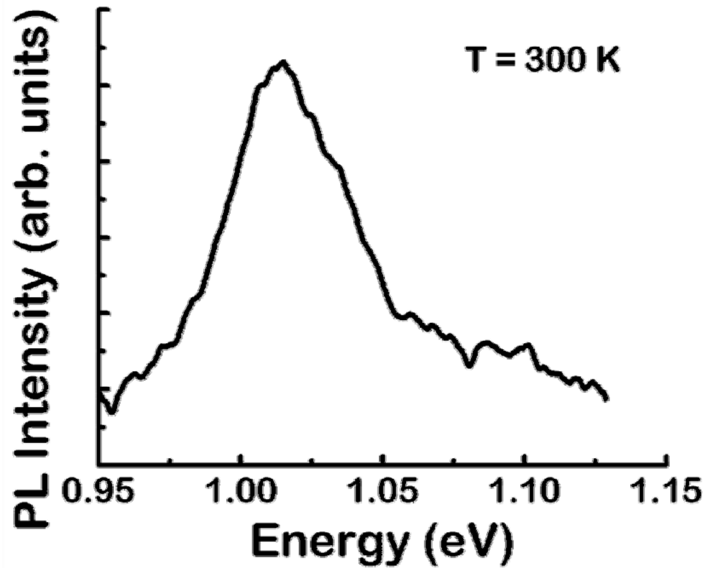

(a)

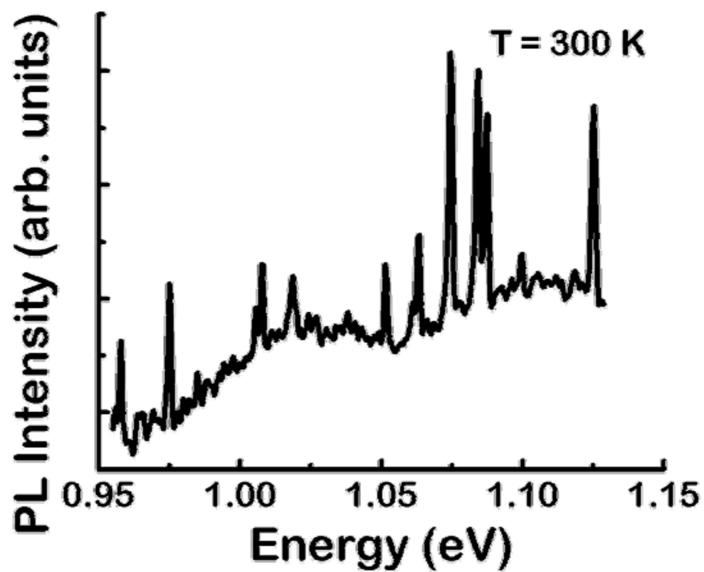

(b)

Figure 6.5 (a) Room temperature photoluminescence spectrum of as-grown sample showing broad emission; (b) emission spectrum of microtube with a radius of ~3 μm and a wall thickness of ~100 nm exhibits multiple resonance peaks. The narrowest linewidth is ~1.5 nm, corresponding to a cavity quality factor of ~800.

Emission characteristics of quantum dot microtube are investigated using micro-photoluminescence spectroscopy. The microtube was optically excited with a diode laser (λ = 523 nm) through an objective lens. Emission from the devices was collected using the same objective, analyzed by a high resolution monochromator, and detected by a liquid nitrogen cooled Ge detector with lock-in amplification. Figure 6.5(a) shows micro-photoluminescence spectrum of as-grown sample exhibiting broad emission at room temperature. On the other hand, the emission spectrum of a microtube with a radius of ~3 μm and a wall thickness of ~100 nm separated by 400 nm from the substrate exhibits multiple resonance peaks. The modes are spaced apart by approximately 12 meV, which is in good agreement with the calculated mode for an optical ring resonator predicted by Eqn. (6.1).

$$\pi \cdot D \cdot n_{eff} = \lambda \cdot m \tag{6.1}$$

D : tube diameter

n_{eff} : effective refractive index

λ : resonant wavelength

m : azimuthal mode number

The minimum linewidth observed is ~1.5 nm and corresponds to a cavity quality factor of ~800. The light-light (L-L) characteristics of the microtube device, shown in Fig. 6.6, are derived from the most dominant emission peak for varying excitation power levels. We believe a soft turn on at ~700 kW/cm^2 represents lasing threshold.

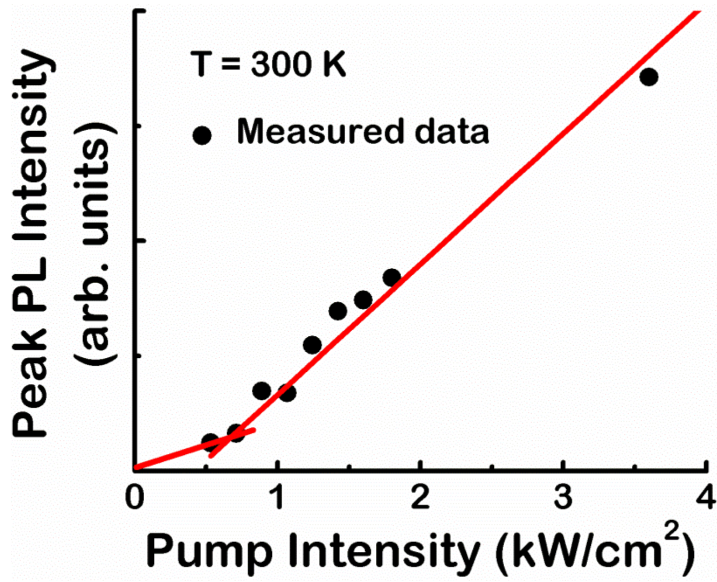

Figure 6.6 Measured light-light characteristics of microtube device showing a threshold at ~700 kW/cm^2.

6.5 Finite difference time domain (FDTD) simulation

The confined optical modes in a rolled-up microtube were analyzed using the FDTD method. The differences from conventional ring resonators are that the resonator is a hollow tube and is not filled, and the thickness of the tube wall is much less than the light wavelength that passes around the tube periphery. Furthermore, the circular symmetry present in conventional ring resonators is broken due to the spiral tube shape. Therefore, the microtube cavity is approximated as a free-standing spiral optical ring resonator, with the presence of inside and outside notches (Fig. 6.7(a)).

From a previous study [97], it was found that the transverse electric (TE) modes having an electric field normal to the wall surface experience loss due to diffraction. Hence, we limit the calculation to transverse magnetic (TM) modes with an electric field

parallel to the wall sheet and a magnetic field perpendicular to the wall as shown in Fig. 6.7 (a).

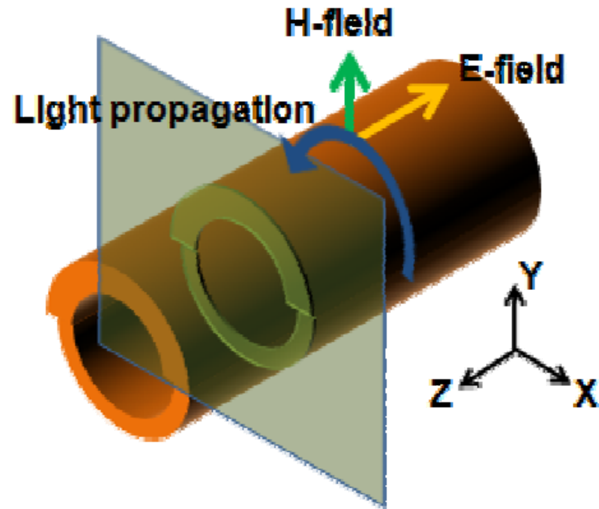

(a)

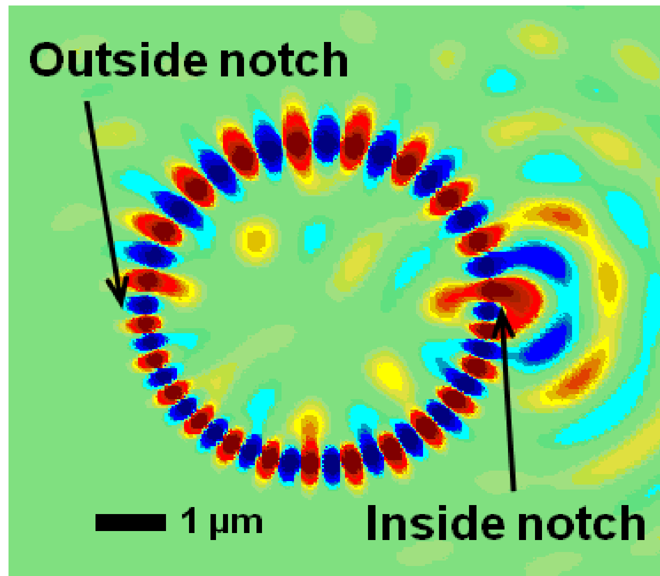

(b)

Figure 6.7 (a) Schematic representation of a spiral microtube structure. TM mode with an electric field parallel to the wall and a magnetic field normal to the wall is shown; (b) Distribution of the optical resonance modes simulated by FDTD method for microtube ring resonator with a diameter of 5 μm. Strong emission from the inside notch can be clearly observed.

The simulated azimuthal mode profiles for photons ($\lambda \sim 1.3$ μm) confined in a microtube with tube diameters of 5 μm and wall thickness of 100 nm are shown in Fig. 6.7(b). It can be clearly observed that photons are strongly confined in microtubes. The scattering loss around the tube surface is essentially negligible, due to the epitaxially smooth surface. The calculated Q-factors are in the range of 5,000 to 100,000, depending on the tube diameters and wall thicknesses, which are primarily limited by the optical scattering at the inside notch [97]. This unique phenomenon is enormously important for the achievement of nanoscale lasers with directional emission and output efficiency that are generally difficult to realize using photonic crystal, microdisk, and toroidal based optical cavities.

6.6 Theoretical calculation of threshold

In order to achieve a microtube based nanoscale quantum dot laser, it is necessary to understand the effects of key design parameters affecting the modal gain, such as the tube diameter and wall thickness. Since a microtube is formed by strain-driven self rolling mechanism, it consists of two different thicknesses of walls and two notches at which the wall thickness changes (Fig. 6.8). A microtube cavity can support two resonant modes: (1) a longitudinal mode propagating along the tube axis and (2) an angular mode propagating along the circumference. We assume that an angular mode is dominant because of poor reflection on both ends of the microtube, which is essential to support the longitudinal mode. Hence, the microtube is approximated as a ring resonator shown in Fig. 6.8(b). In this structure, the bending loss and the scattering loss are two major loss

mechanisms. The bending loss occurs when the light travels along a curved wall, and the scattering loss happens at two notches because of a step discontinuity of the wall.

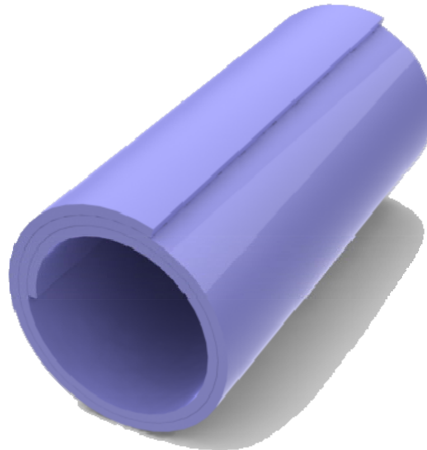

(a)

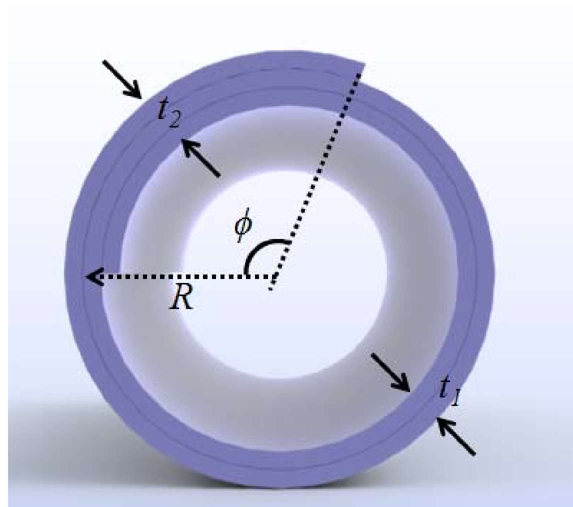

(b)

Figure 6.8 (a) Schematic representation of a microtube cavity; (b) the front view of a microtube cavity. A microtube cavity is approximated to a ring resonator with two different thicknesses of walls and two notches.

6.6.1. Bending loss

Figure 6.9 shows the geometry of a curved waveguide with a radius curvature of *R* and a thickness of *t*. The wave equation in cylindrical coordinates to describe a wave in a curved waveguide is given by Eqn. (6.2).

$$\frac{d^2E_z}{dr^2}+\frac{1}{r}\frac{dE_z}{dr}+\left[k_0^2n^2(r)-\frac{\beta^2}{r^2}\right]E_z=0 \tag{6.2}$$

$$E_z(x)=\left(1+\frac{x}{R}\right)^{-1/2}F(x)\exp(-j\beta y) \tag{6.3}$$

$$\frac{d^2F}{dx^2}+\left[k_0^2n^2(x)-\beta_e^2/h_s^2\right]F=0 \text{ where } h_s=1+x/R \text{ and } \beta_e^2=\beta^2-1/(2R)^2 \tag{6.4}$$

$$\beta\approx\beta_0+\delta\beta_1/R+\delta\beta_2/R^2 \tag{6.5}$$

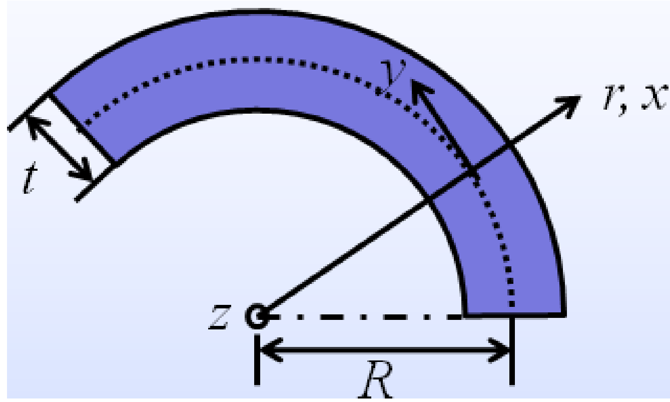

Figure 6.9 A geometry of a curved waveguide representing a wall of a microtube cavity.

With a proper transformation (Eqn. (6.3)), Eqn. (6.2) is reduced to Eqn. (6.4) and the propagation constant (Eqn. (6.5)) is represented by a propagation constant in a straight waveguide and a series of R^{-1} functions [99]. Calculated deviation of the propagation constant in a curved waveguide from the propagation constant in a straight waveguide is

shown in Fig. 6.10. The difference between them becomes larger as the radius of curvature (R) increases, but this difference is negligible even at R = 1μm. The bending loss is evaluated as the ratio of the radiated power to the total power [99, 100] and is approximated by Eqn. (6.6).

$$\gamma_b \approx \frac{2p^2s^2}{v^4(st+2)}k_0(n_s - n_a)\exp\left(-\frac{s^3}{3v^3}R_0\right) \tag{6.6}$$

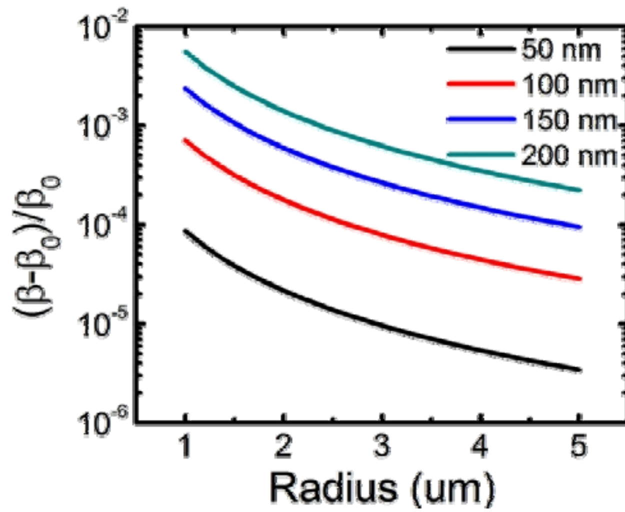

Figure 6.10 Deviation of a propagation constant in a curved waveguide. β and β_0 represent a propagation constant in a curved waveguide and a straight waveguide, respectively.

The bending loss is evaluated by changing the radius of curvature for various wall thicknesses. As shown in Fig. 6.11, the bending loss approximated by Eqn. (6.5) (dashed line) shows good agreement with accurate numerical calculations (solid lines). A thin microtube suffers more bending loss than a thick microtube because of less light confinement inside the wall, and the bending loss increases exponentially as the radius curvature increases.

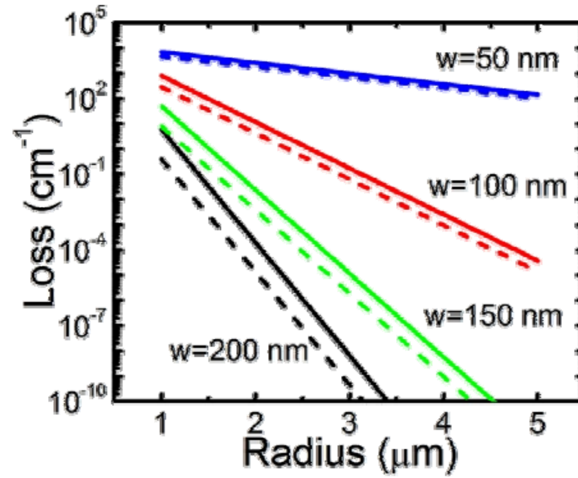

Figure 6.11 The radius dependent bending loss for different wall thicknesses. The bending loss shows an exponential dependence on the radius.

6.6.2. Scattering loss at notches

Light traveling the microtube experiences a step discontinuity of the waveguide at two notches (inside and outside notches) as shown in Fig. 6.12(a). The scattering loss at each notch is modeled as a straight waveguide with a step discontinuity and evaluated by using a mode matching method [101]. Figure 6.12(b) describes all possible modes which can exist around a step. When light reaches the step discontinuity, some of the incident light energy is lost as radiation. Backward-scattered energy is coupled to radiation modes of the input side, whereas forward-scattered energy is coupled to radiation modes of the output side. Thus, to the left of the discontinuity, the fields consist of the incident and reflected guided modes along with the continuum of backward-traveling radiation modes, whereas to the right, the fields include the transmitted guided mode and the continuum of forward-traveling radiation modes (Eqn. (6.7)).

$$E_z^{(I)} + \int_0^{k_0 n_a} e_R(\kappa) E_z^{(R)}(\kappa) d\kappa = c_T E_z^{(T)} + \int_0^{k_0 n_a} e_T(\kappa) E_z^{(T)}(\kappa) d\kappa \quad (6.7)$$

- $e_R(\kappa)$: Amplitude coefficient of the backward traveling radiation mode
- $e_T(\kappa)$: Amplitude coefficient of the forward traveling radiation mode
- c_T : Amplitude coefficient of the transmitted guided mode

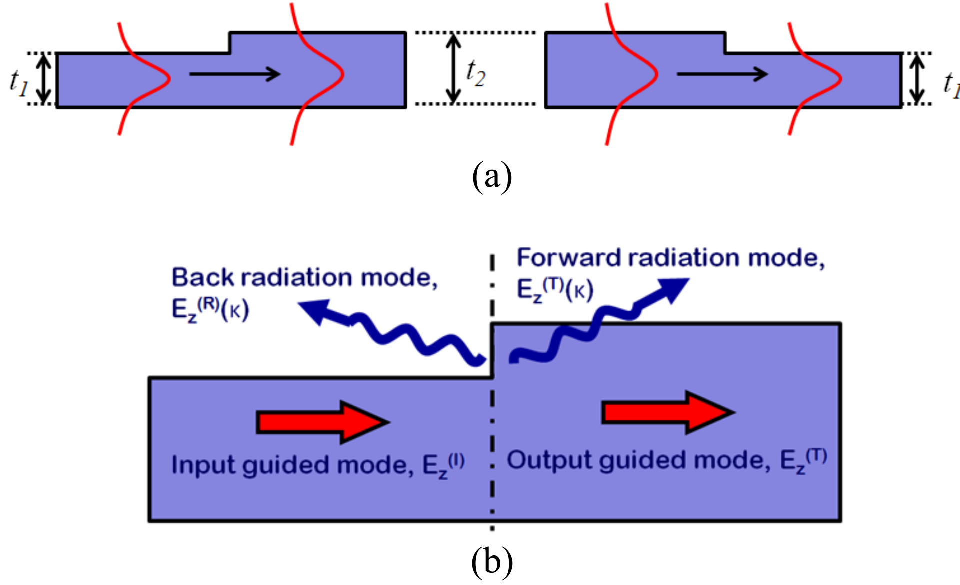

Figure 6.12 (a) Schematic representation of inside and outside notches along the microtube; (b) schematic representation of an equivalent waveguide with a step discontinuity. The input guided mode at the step discontinuity partially changes to an output guided mode and the rest of them is scattered in forward and backward directions.

According to the energy conservation law, the total energy on the left side must be the same with that of the right side as Eqn. (6.8).

$$|c_T|^2 + |e_R(\kappa)|^2 + |e_T(\kappa)|^2 = 1 \quad (6.8)$$

Backward radiation modes are also assumed to be orthogonal to forward radiation modes. This approximation is quite good for small step discontinuities but for large step, the

approximation fails. As a result, the total power loss due to a step discontinuity is given by Eqn. (6.9).

$$\frac{P_{rad}}{P_{in}} = \int_{-k_0 n_a}^{k_0 n_a} \left(\frac{\beta_r + \beta_1}{4\omega\mu_0} \right)^2 \left(I_m^2 + I_n^2 \right) \frac{|\beta_r|}{\kappa} d\beta_r \tag{6.9}$$

$$\text{where} \quad I_{m,n} = \int_{-\infty}^{\infty} E_z^{(I)} E_{zm,n}^{(T)}(\kappa) dx$$

The calculated scattering losses from a 100 nm thick waveguide to a thicker waveguide and from a 150 nm thick waveguide to a thinner waveguide are shown in Fig. 6.13. As intuitively expected, the radiation loss increases as the step discontinuity becomes larger.

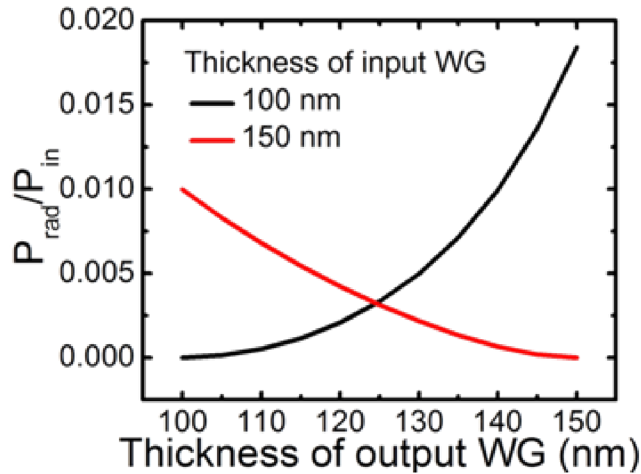

Figure 6.13 Calculated scattering loss at notches when the light travels from 100 nm thick waveguide to a thicker waveguide (black) and from 150 nm thick waveguide to a thinner waveguide (red).

6.6.3. Optical loss through substrate

The free standing rolled-up microtube cavity discussed in Chapter 6.2 is not perfectly suspended in air. The separation of the microtube is strongly dependent on the number of revolutions and the wall thickness. Therefore, in most cases, the close proximity of the microtube to the substrate induces an optical loss. In order to evaluate

the substrate loss, the Q-factors of the ring resonators are calculated varying the distance between the resonator and substrate (Figure 6.14(a)). When the separation of a resonator is less than 400 nm the Q-factor decreases exponentially due to substrate loss. In other words, for a microtube suspended 400 nm away from the substrate, substrate loss can be ignored.

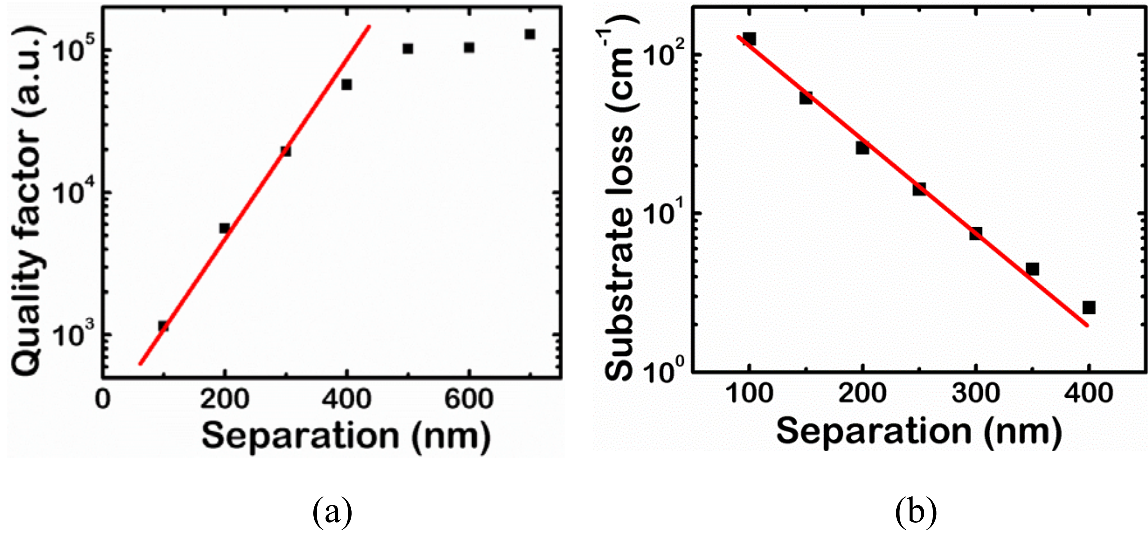

(a) (b)

Figure 6.14 (a) Variation of calculated cavity quality factors in a ring resonator. The wall thickness is 100 nm; (b) calculated substrate loss from a Q-factor.

By using Eqn. (6.10) [63], the Q-value is converted to a loss with a unit of cm^{-1}.

$$\alpha_{sub} = \frac{2\pi n_{eff}}{\lambda} \cdot \frac{1}{Q} \tag{6.10}$$

As shown in Fig. 6.14(b), substrate loss sharply increases as the separation reduces.

6.6.4. Modal gain and threshold carrier density

In order to set up the modal gain equation, the change in intensity of light after one round trip is considered. The light (I_0) passes through two notches in a single round trip, partially scattering and partially transmitting, where the transmission rate at each notch is represented by T_1 and T_2. It also loses energy while traveling curved walls,

represented by γ_{b1} and γ_{b2} for two different wall thicknesses. The threshold gain must be exactly equal to the roundtrip loss and can be represented by the sum of the bending loss, the scattering loss at notches, and the substrate loss (Eqn. 6.11).

$$g_{th} = \alpha_{bend} + \alpha_{step} + \alpha_{sub} \tag{6.11a}$$

$$\alpha_{bend} = \gamma_{b1} l_1 + \gamma_{b2} l_2 \tag{6.11b}$$

$$\alpha_{step} = \frac{1}{l_1 + l_2} \ln\left(\frac{1}{T_1 T_2}\right) \text{ where } l_1 = R(2\pi - \phi) \text{ and } l_2 = R\phi \tag{6.11c}$$

First, the bending loss and scattering loss are compared in Fig. 6.15(a). The bending loss is very small compared to the scattering loss at the notches and can be ignored. Therefore, the modal gain can be further approximated as (6.12). In conclusion, the threshold gain is inversely proportional to the radius of the microtube (Fig. 6.15(b))

$$\therefore g_{th} \approx \frac{1}{l} \ln\left(\frac{1}{T_1 T_2}\right) + \alpha_{sub} = \frac{1}{2\pi R} \ln\left(\frac{1}{T_1 T_2}\right) + \alpha_{sub} \tag{6.11}$$

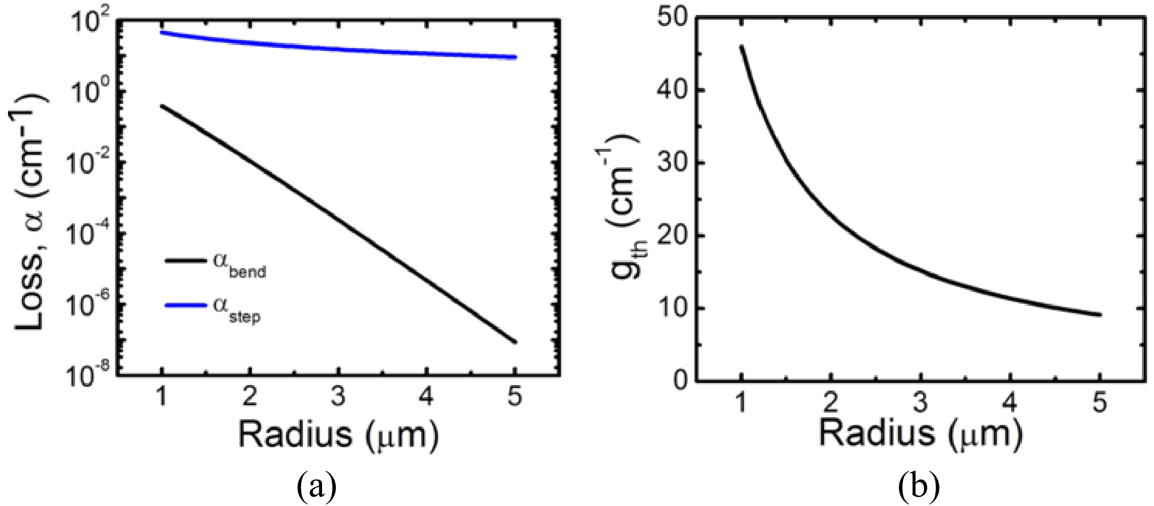

Figure 6.15 (a) The bending loss and the scattering loss by varying the radius curvature. The scattering loss is a dominant loss, which determines the threshold gain; (b) the radius curvature dependent threshold gain of a microtube. It is noted that the modal gain is inversely proportional to the radius of the microtube.

Based on the density matrix equation, the linear optical gain of the quantum dot active region with a volume density of dots N_D is given as Eqn. (6.13) [102, 103].

$$g(E) = \frac{2\pi e^2 \hbar N_D}{c n_r \varepsilon_0 m_0^2} \sum_{c,v} \frac{\left|P_{cv}^{\sigma}\right|^2}{E_{cv}} \int_{-\infty}^{\infty} \left[f_c(E') - f_v(E')\right] \cdot G(E' - E_{cv}) B_{cv}(E - E') dE' \tag{6.13}$$

E_{cv} : energy of interband transition.

$f_c(E')$: electron occupation function of the conduction band discrete state of the dots with the interband transition energy of E'.

$f_v(E')$: valence band discrete states.

P_{cv}^{σ} : transition matrix element

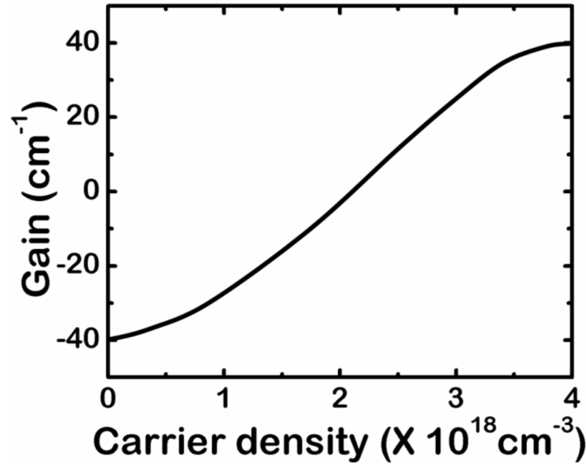

Figure 6.16 The maximum gain versus the carrier density with the Gaussian density of state broadening due to the quantum dot size fluctuation.

The inhomogeneous broadening due to the dot size fluctuation is considered as a Gaussian distribution function, $G(E)$ and the homogeneous broadening is also taken to account as a Lorentzian function, $B_{cv}(E)$. Figure 6.16 shows the calculated maximum gain versus the carrier density. After a transparent carrier density of around 2×10^{18} cm^{-3}, there is a linear increase in gain as the carrier density increases until it ultimately

saturates. Therefore, we can conclude that the threshold carrier density will follow the same behavior as the modal gain described earlier and we expect the threshold of the microtube to vary inversely proportional to the radius.

6.7 Conclusion

We have demonstrated coherent light emission from rolled-up InGaAs/GaAs quantum dot microtubes under optical pumping at room temperature. A surface passivation technique using ammonium sulfide is employed to prevent carrier depletion in a thin GaAs layer. Optical characterization reveals a threshold density of ~700 W/cm^2 from the microtubes with a diameter of ~6 μm and a wall thickness of ~100 nm, and the observed optical modes are determined by the tube diameter. The FDTD method confirms directional emission from the inside notch. Theoretical studies of modal gain and threshold carrier density are carried out to understand design parameters affecting the modal gain. We conclude that the threshold will be inversely proportional to the radius of the microtube.

Chapter VII

Conclusions and Suggestions for Future Work

7.1 Summary of completed work

In this study, different nanoscale coherent light sources with microcavities, which can be used for future optical interconnects and medical diagnosis, have been realized. Optically and electrically injected silicon based coherent light sources using PbSe QDs embedded in photonic crystal and planar microcavities are important in that they can be integrated with silicon technology. Monolithically integrated GaN nanowire lasers with PC microcavities also have the potential to allow on-chip and off-chip optical communication. A single GaN nanowire embedded in DBR mirrors shows polariton lasing in the strong coupling regime, which can be exploited as a zero threshold laser for low-power application. Strain-driven rolled up microtube cavities featuring InAs QDs with atomically smooth surfaces provide a high quality factor and ensure low threshold lasing at room temperature.

7.1.1. Coherent photoluminescence from PbSe colloidal QDs in silicon-based PC microcavities.

Enhanced photoluminescence from high-Q silicon-based random photonic crystal microcavities embedded with PbSe colloidal quantum dots was experimentally observed and investigated. The emission is optically excited at room temperature by a continuous-wave Ti-Sapphire laser and exhibits randomly-distributed localized modes with a

minimum spectral linewidth of 4 nm at a wavelength of 1.5 μm. It also shows a soft threshold at ~ 100 μW, which is the onset of enhanced spontaneous emission coupled into localized modes as a result of strong feedback from random PC microcavities. Such nanoscale light sources could be of interest as optical interconnects in silicon photonics, and are potentially compatible with complementary metal oxide semiconductor chips.

7.1.2 1.5 μm PbSe colloidal QD coherent electroluminescent devices on silicon

The characteristics of electrically injected silicon-based photonic crystal microcavities with PbSe quantum dots are described. The device includes suitable electron and hole transporting layers and contact layers. The measured electroluminescence at room temperature exhibits enhanced spontaneous emission. The resonant mode is observed at λ=1669 nm with a spectral linewidth of 4 nm, corresponding to a cavity Q-factor of ~420.

The PbSe QDs are also sandwiched between a metallic mirror and a DBR mirror to demonstrate coherent and directional emission at 1.55 μm. QDs are chemically treated in order to increase the electronic coupling, and electrons and holes are injected through ZnO nanocrystals and indium tin oxide, respectively. The measured electroluminescence exhibits a minimum linewidth of ~3.1 nm corresponding to a cavity quality factor of ~500 at a low injection current density of 3 A/cm^2, and highly directional emission characteristics. This electrically injected silicon based light source with a fairly narrow linewidth is one of the most promising technologies for optical interconnects.

7.1.3. Monolithically integrated GaN nanowire laser on silicon

Optically pumped lasing at room temperature in a silicon based monolithic single GaN nanowire with a two dimensional photonic crystal microcavity is demonstrated.

Catalyst-free low density (~10^8 cm^{-2}) nanowires were grown on (001) and (111) Si by plasma-assisted molecular beam epitaxy. High resolution transmission electron microscopy images reveal that the nanowires are of wurtzite structure with the *c*-axis parallel to the growth direction and that they have no observable defects. A single nanowire laser fabricated on (111) Si is characterized by a lasing transition at λ=371.3 nm with a measured linewidth of 0.55 nm. The threshold is observed at a pump (λ=266 nm) power density of ~120 kW/cm^2. The quality factor of the cavity, modal gain and the spontaneous emission factor β are estimated to be 570, ~520 cm^{-1}, and 0.08, respectively.

7.1.4. GaN nanowire polariton laser

Room temperature polariton lasing at low threshold density was achieved in a vertical microcavity containing a single GaN nanowire. The threshold density is two orders of magnitude lower than reported values for GaN-based polariton lasers. Low-threshold lasing results from stimulated scattering and accumulation of a quantum degenerate polariton population near the band minimum. In comparison, a second threshold corresponding to conventional photon lasing is also observed at a density 2700 times the polariton lasing threshold density. Reducing the lateral size of the microcavity would increase the photon-exciton coupling and further improve the optical qualities of the polariton laser. This work represents a first step in developing a new generation of ultra-low power and ultra-compact, room-temperature photonic devices based on GaN nanowire polaritons.

7.1.5. Rolled-up microtube laser with InAs quantum dots

Coherent light emission from rolled-up InGaAs/GaAs quantum dot microtubes was demonstrated at room temperature. In order to prevent carrier depletion in a thin

GaAs layer, surface passivation using ammonium sulfide is employed. Optical characteristics of the microtube with a diameter of ~6 μm and wall thickness of ~100 nm shows a threshold density of ~700 W/cm^2 and the minimum linewidth of 1.5 nm. FDTD method confirms directional emission from the inside notch, which is challenging to realize using other microcavities. Theoretical studies of the modal gain reveal that the threshold is inversely proportional to the radius of the microtube. Such novel micro- and nano-tube may emerge as a new class of nanophotonic devices for applications in chip-level optical interconnects, single photon generation, and chemical and biochemical sensors.

7.2 Suggestions for future work

7.2.1. Electrically injected GaN nanowire polariton laser

An electrically injected device is absolutely required to enhance the practicality of polariton lasers, but electrical injection of exciton and polariton states is a challenging task. As preliminary work, electrically injected single GaN nanowire light emitting diode (LED) was demonstrated. Figure 7.1(a) shows the SEM image of the fabricated device. A single GaN nanowire was laid down on SiO_2 and p- and n-type contact was defined by electron beam lithography. The measured current-voltage characteristic of the device shows a turn on at ~15 V and the electroluminescence data at an injection current of 4μA exhibits a peak around 364 nm (Figs. 7.1(b) and (c)).

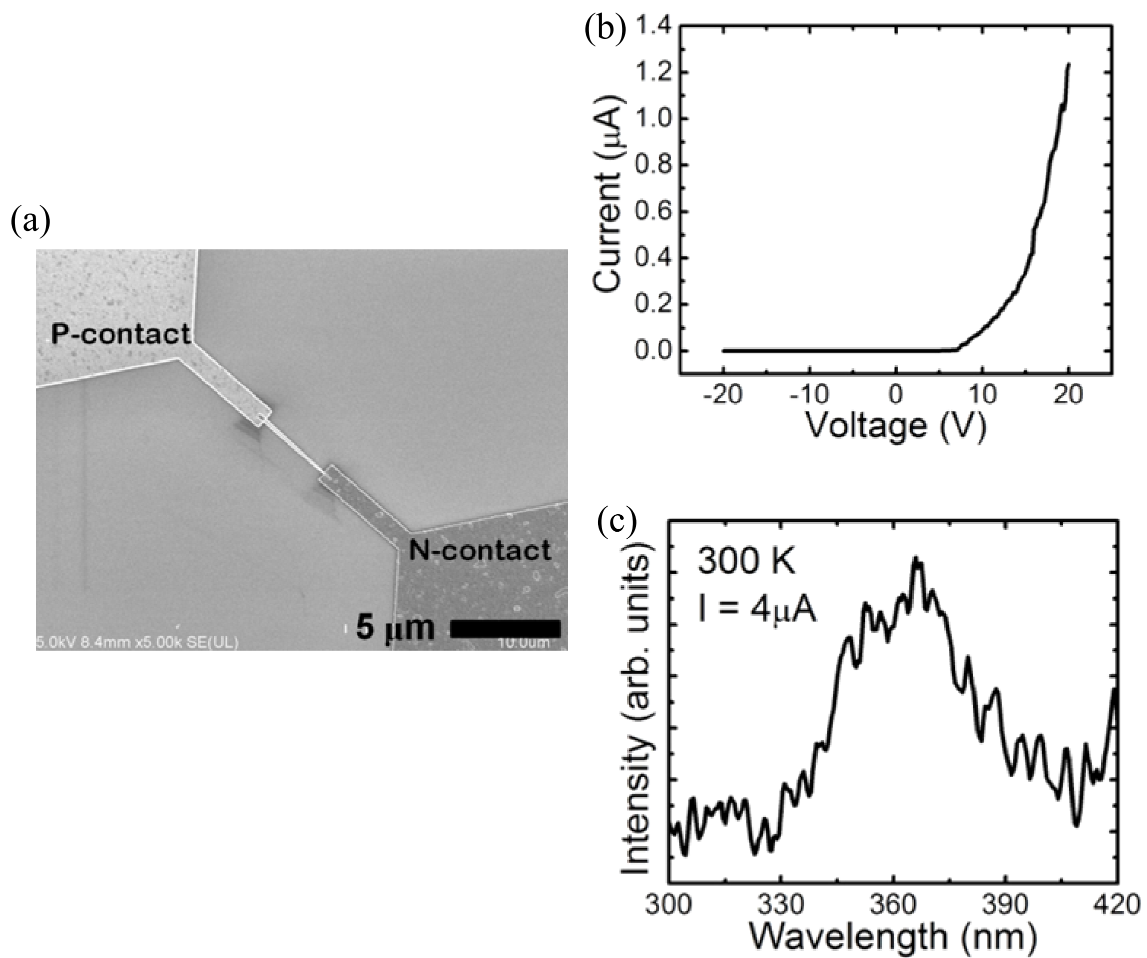

Figure 7.1 (a) SEM image of a fabricated single GaN device with contacts; (b) current-voltage characteristic of device with a turn on voltage of ~15 V; (c) measured electroluminescence at an injection current of 4μA.

After a single GaN nanowire is dispersed on top of the half cavity layers, p- and n-type contacts will be made (Fig. 7.2(a)). The mesa definition after deposition of the top DBR allows the contacts to be exposed (Fig. 7.2(b)).

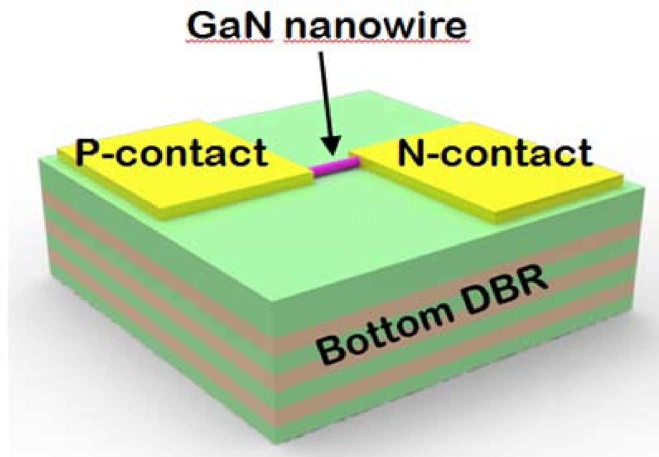

(a)

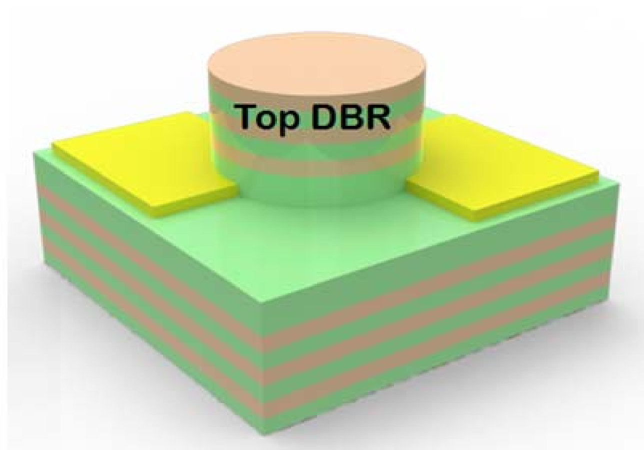

(b)

Figure 7.2 Schematic of an electrically injected single GaN nanowire polariton laser before (a) and after (b) the deposition of top DBR.

7.2.2. Electrically injected rolled-up microtube laser

Electrical injection to the rolled-up microtube needs to be investigated for practical applications such as coherent light sources. Figure 7.3 shows a schematic representation of an electrical device. Since the GaAs layer must be kept thin to fabricate a small diameter microtube, it is very challenging to incorporate p- and n-type dopants.

Hence, we will use p-type ion implantation process on one side of an n-doped GaAs layer. The schematic representation of the fabricated device is shown in Fig. 7.3(b), and it is expected that electrons can be efficiently injected into the microtube's active region and recombine with holes injected from the p-metal contact.

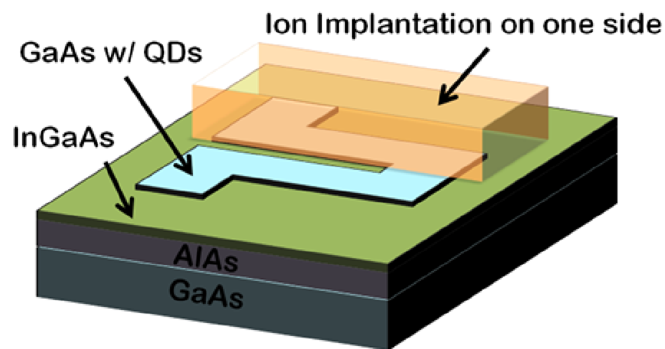

(a)

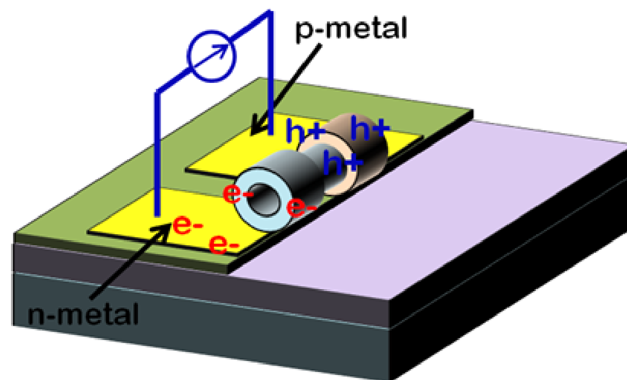

(b)

Figure 7.3 Schematic representation to fabricate an electrically operated rolled-up microtube. (a) ion implantation to dope only one side; (b) the microtube device after rolled-up.

APPENDICES

Appendix A

Purcell effect

In 1946, Edward Purcell first proposed that the spontaneous emission rate of a quasimonochromatic dipole can be controlled by using a cavity to tailor the number of electromagnetic modes to which it is coupled [104]. Cavity quantum electrodynamics (CQED) has provided a firm theoretical and experimental basis for this revolutionary concept [105]. An ability to enhance the spontaneous emission rate (Purcell effect) would open novel avenues for physics and engineering [106], e. g., the development of high efficiency light emitters.

Theoretically, the alteration of the emission rate is usually treated with Fermi's golden rule, i.e. the coupling between the atoms and the cavity is considered weak. In this so called "weak coupling regime", the cavity and the atomic emitter are in resonance, the energy exchange rate between a cavity field and an emitter is not significant so that energy decaying by emission from an atom is irreversible. Fermi's golden rule states that the emission rate is proportional to the product of the mode density (i.e. the spectral density of states) and the matrix element of the atom-field interaction.

$$\frac{1}{\tau} = \frac{4\pi}{\hbar}\rho(\omega)\left\langle\left|\vec{d}\cdot\vec{\varepsilon}(\vec{r})\right|^2\right\rangle \tag{A.1}$$

where $\vec{\varepsilon}(\vec{r})$ is the vacuum electric field amplitude at the location r of the emitter and d is

the electric dipole. $\rho(\omega)$ is the density of modes at the emitter's angular frequency and is given by a normalized Lorentzian in the cavity case.

First, we consider the free space mode density $\rho(\omega)$ and convert it to a volume-normalized mode density $g(\omega) = \rho(\omega)/V$. From classical mechanics,

$$g_f = \frac{\omega^2}{\pi^2 c^3} \tag{A.2}$$

The cavity restricts the modes to a spectral width $\Delta\omega$ and a volume *V*, which transforms the mode density into

$$g_c = \frac{1}{\Delta\omega \cdot V} = \frac{Q}{\omega \cdot V} \tag{A.3}$$

The mode density alteration caused by the cavity is thus given by

$$\frac{g_c}{g_f} = \frac{\lambda^3 Q}{8\pi \cdot V} \tag{A.4}$$

To achieve the final result, we must consider

(a) A real cavity is best described by a Lorentzian line shape function.

$$g_c = \frac{2}{\pi} \cdot \frac{1}{\Delta\omega \cdot V} \tag{A.5}$$

(b) The maximum possible enhancement is achieved when the radiating dipole, in relation to the three orthogonal axes, is oriented to experience the maximum interaction with the cavity mode. This gives an additional factor of three over the bulk case.

In total, we obtain the following expression for the cavity enhancement factor, which was first suggested by Purcell.

$$F_p = \frac{g_c}{g_f} \times 3 \times \frac{2}{\pi} = \frac{3\lambda^3 Q}{4\pi^2 \cdot V} = \frac{6}{\pi^2} \cdot \frac{Q}{V'}, \quad \text{with } V' = \frac{V}{(\lambda/2)^3} \tag{A.6}$$

A more accurate derivation by taking into account the mode degeneracy *g* and the dipole orientation leads to the following expression.

$$F_p = \frac{3\lambda^3 Q}{2\pi \cdot V} g \tag{A.7}$$

It is worthwhile to mention that the *V* is the effective mode volume, which is given by the spatial integral of the vacuum field intensity for the cavity mode, divided by its maximum value.

$$V = V_{\mathrm{mod}e}^{eff} = \frac{\int_V \varepsilon(\vec{r}) \left|\vec{E}(\vec{r})\right|^2 d^3 r}{\max\left(\varepsilon(\vec{r}) \left|\vec{E}(\vec{r})\right|^2 \right)} \tag{A.8}$$

The Purcell factor is a figure of merit for the cavity alone, which describes its ability to increase the coupling of an ideal emitter with the vacuum field, via a local enhancement of its intensity (small *V*'s) or of the effective mode density (high Q's).

Appendix B

Fabrication of photonic crystals

1. Sample preparation and cleaning

    1.1. Prepare silicon-on-insulator.

        1.1.1. The thickness of top silicon is determined based on the resonant wavelength. It needs to be thick enough to accommodate the fundamental mode of light but must not allow any higher optical mode for single mode operation.

        1.1.2. For free-standing photonic crystal microcavity, the buried oxide must be at least half of the resonant wavelength. Smaller gap will increase optical loss through the silicon substrate.

    1.2. Piranha cleaning to remove organic residues.

        1.2.1. Prepare Piranha solution (H_2SO_4 : H_2O_2 = 3 : 1).

        1.2.2. Immerse a sample in prepared solution for 20 mins.

        1.2.3. Rinse in a DI water thoroughly.

    1.3. Native oxide removal.

        1.3.1. Prepare Buffered hydrofluoric acid (BHF) solution.

        1.3.2. Immerse a sample in prepared BHF for 2 min.

        1.3.3. Rinse in a DI water thoroughly.

    1.4. Blow water on the sample with nitrogen.

    1.5. Dry the sample on 130 ºC hot plate for 2 min.

2. Silicon dioxide (SiO_2) deposition.

2.1. SiO_2 layer will be used as a etch mask to etch silicon layer. Thickness of SiO_2 must be carefully determined according to the etch selectivity between Si and SiO_2. Generally, one fourth or one fifth of silicon thickness is fine.

2.2. SiO_2 is deposited by plasma enhanced chemical vapor deposition (PECVD) at 380 ^oC.

2.2.1. 'Oxide_380' recipe in GSI PECVD.

2.2.2. Calibrate thickness with a dummy run.

3. Cleaning sample (Degreasing).

3.1. Sample is immersed in Acetone at 105 ^oC for 5min.

3.2. Sample is immersed in isopropyl alcohol (IPA) for 5min.

3.3. Blow solvent on the sample with nitrogen.

3.4. Dry the sample on 130 ^oC hot plate for 2min to remove any solvent residue.

4. Electron beam lithography

4.1. PMMA coating.

4.1.1. Thickness of PMMA must be carefully determined according to etch selectivity between PMMA and SiO2. The same thickness of PMMA with SiO2 is recommended.

4.1.2. MicroChem 950K A4 at 3000 rpm for 45 sec gives ~300 nm of PMMA.

4.1.3. Baking the sample at 180 ºC hot plate.

4.2. Electron beam lithography.

4.2.1. Photonic crystal pattern can be exposed by either dot exposure or area exposure. Dot exposure is fast but it requires a very high quality of beam adjustment. Also, it is difficult to reproduce the result. Overall, area exposure is highly recommended.

4.2.2. Accelerating voltage : 20 kV.

4.2.3. Apperture size : 10 μm.

4.2.4. Dose : 180-200 μC/cm2.

4.3. Development

4.3.1. Developer solution (IPA: MIBK = 3 : 1) must be made 1 hour prior to use.

4.3.2. Stir the sample in developer for 1min.

4.3.3. Rinse the sample in IPA for 45 sec.

4.3.4. Blow IPA on the sample with nitrogen.

4.4. Descum

4.4.1. March asher in GaAs bay is used.

4.4.2. Pressure : 200 mT.

4.4.3. Power : 30 W.

4.4.4. Time : 15 sec.

5. Dry etching SiO_2

5.1. Use Plasma Therm 790.

5.2. Recipe name : jh_sio.

5.3. Etch rate : ~320-340 Å/min.

6. PMMA removal.

6.1. Oxygen Plasma.

6.1.1. March asher in GaAs bay.

6.1.2. Pressure : 250 mT.

6.1.3. Power : 180 W.

6.1.4. Time : 180 sec.

6.2. Immerse a sample in Acetone for 5 min.

6.3. The sample is moved and immersed in a fresh Acetone again for 5 min.

6.4. Immerse a sample in IPA for 5 min.

6.5. Blow IPA on the sample with nitrogen.

7. Dry etching Si.

   7.1. Use LAM etcher (ICP RIE).

   7.2. Recipe name : POLY_ETCH2.

   7.3. Etch rate : ~120 nm/min.

8. Remove SiO2

   8.1. Prepare a dilute BHF solution (BHF : DI = 1 : 10) and DI water

   8.2. Immerse a sample in a prepared dilute BHF solution for enough time. Etch rate should be calibrated prior to use.

   8.3. Rinse a sample in prepared DI water (not in a cascade rinse). Sample must be handled very carefully.

   8.4. Repeat 8.3 three times to rinse any acid residue completely.

   8.5. Leave a sample dried on cleanroom paper. Do not use a nitrogen gun.

Appendix C

Wannier-Mott exciton

An exciton is a bound state of an electron and hole which are attracted to each other by Coulomb interaction. When an electron with charge $-e$ is excited from the valence band into the conduction band, the vacancy it leaves in the valence band can be described as a hole. A hole in the valence band has charge $+e$ and an effective mass defined by $-(\partial^2 E/\partial p^2)^{-1}$, E and p denoting the energy and momentum of the hole. A hole and an electron at $p \sim 0$ interact with each other via Coulomb interaction and form a bound pair (an exciton) analogous to a hydrogen atom where an electron is bound to a proton. However, due to the strong dielectric screening in solids and a small reduced mass, the binding energy of a semiconductor exciton is on the order of 10-100 meV and its Bohr radius is about 10-100 Å, extending over tens of atomic sites in the crystal, which is called Wannier-Mott exciton [107]. Excitons can be considered as bosons when the exciton interparticle spacing is much larger than its Bohr radius.

$$n_{exc} << a_B^{-3} \tag{C.1}$$

The electron and hole in an exciton form a dipole that interacts with electromagnetic field of light. The interaction strength with light at angular frequency ω is described by the exciton oscillator strength.

$$f = \frac{2m^* \omega}{\hbar} \left| \langle u_v | r \cdot e | u_c \rangle \right|^2 \frac{V}{\pi a_B^3} \tag{C.2}$$

$m^* = (1/m_e + 1/m_h)^{-1}$: The effectivee mass of the exciton

u_c : The electron Bloch function

u_v : The hole Bloch function

V : The Quantization volume

a_B : The Bohr radius of the exciton.

$V/\pi a_B^3$ reflects the enhancement of the interaction due to enhanced electron-hole overlap in an exciton compared to a pair of unbound electron and hole.

BIBLIOGRAPHY

[1] K. F. MacDonald and N. I. Zheludev, *Laser & Photonics Reviews* **4**, 562 (2010).

[2] Y. Vlasov, W. M. J. Green, and F. Xia, *Nat Photon* **2**, 242 (2008).

[3] P. Gourley, J. Hendricks, A. McDonald, R. Copeland, K. Barrett, C. Gourley, and R. Naviaux, *Biomedical Microdevices* **7**, 331 (2005).

[4] *Silicon Integrated Nanophotonics*. (2010). Retrieved September 11 2011, from http://domino.research.ibm.com/comm/research_projects.nsf/pages/photonics.index.html.

[5] G. B. H. von Hogersthal and J. J. Baumberg. *New mechanism for microcavity lasers at room temperature*. SPIE Newsroom (2007). Retrieved September 13 2011, from http://spie.org/x16671.xml?ArticleID=x16671.

[6] S. Reitzenstein, A. Bazhenov, A. Gorbunov, C. Hofmann, S. Munch, A. Loffler, M. Kamp, J. P. Reithmaier, V. D. Kulakovskii, and A. Forchel, *Appl. Phys. Lett.* **89**, 051107 (2006).

[7] A. Nakagawa, S. Ishii, and T. Baba, *Appl. Phys. Lett.* **86**, 041112 (2005).

[8] Y. Akahane, T. Asano, B.-S. Song, and S. Noda, *Nature* **425**, 944 (2003).

[9] S. Chakravarty, P. Bhattacharya, and Z. Mi, *Photonics Technology Letters, IEEE* **18**, 2665 (2006).

[10] J. C. Johnson, H.-J. Choi, K. P. Knutsen, R. D. Schaller, P. Yang, and R. J. Saykally, *Nat Mater* **1**, 106 (2002).

[11] F. Li and Z. Mi, *Opt. Express* **17**, 19933 (2009).

[12] R. J. Walters, G. I. Bourianoff, and H. A. Atwater, *Nat Mater* **4**, 143 (2005).

[13] S. G. Cloutier, P. A. Kossyrev, and J. Xu, *Nat Mater* **4**, 887 (2005).

[14] Z. Wu, Z. Mi, P. Bhattacharya, T. Zhu, and J. Xu, *Appl. Phys. Lett.* **90**, 171105 (2007).

[15] R. Bose, X. Yang, R. Chatterjee, J. Gao, and C. W. Wong, *Appl. Phys. Lett.* **90**, 111117 (2007).

[16] W. W. Yu, J. C. Falkner, B. S. Shih, and V. L. Colvin, *Chemistry of Materials* **16**, 3318 (2004).

[17] J. Xu, D. Cui, T. Zhu, G. Paradee, Z. Liang, Q. Wang, S. Xu, and A. Y. Wang, *Nanotechnology* **17**, 5428 (2006).

[18] J. D. J. Steven G. Johnson, *Photonic Crystals : The Road from Theory to Practice*. 1st ed. (Springer, 2002).

[19] T. Asano, B.-S. Song, and S. Noda, *Opt. Express* **14**, 1996 (2006).

[20] J. Topolancik, F. Vollmer, and B. Ilic, *Appl. Phys. Lett.* **91**, 201102 (2007).

[21] S. John, *Physical Review Letters* **58**, 2486 (1987).

[22] A. Yamilov, X. Wu, X. Liu, R. P. H. Chang, and H. Cao, *Physical Review Letters* **96**, 083905 (2006).

[23] H. Cao, Y. G. Zhao, S. T. Ho, E. W. Seelig, Q. H. Wang, and R. P. H. Chang, *Physical Review Letters* **82**, 2278 (1999).

[24] K. Y. Bliokh, Y. P. Bliokh, and V. D. Freilikher, *J. Opt. Soc. Am. B* **21**, 113 (2004).

[25] J. Pang, S. Xiong, F. Jaeckel, Z. Sun, D. Dunphy, and C. J. Brinker, *Journal of the American Chemical Society* **130**, 3284 (2008).

[26] I. Fushman, D. Englund, and J. VuCkovic, *Appl. Phys. Lett.* **87**, 241102 (2005).

[27] B. Min, S. Kim, K. Okamoto, L. Yang, A. Scherer, H. Atwater, and K. Vahala, *Appl. Phys. Lett.* **89**, 191124 (2006).

[28] C. E. Finlayson and et al., *Semiconductor Science and Technology* **21**, L21 (2006).

[29] D. F. Dorfner, T. Hurlimann, G. Abstreiter, and J. J. Finley, *Appl. Phys. Lett.* **91**, 233111 (2007).

[30] S. Hoogland, V. Sukhovatkin, I. Howard, S. Cauchi, L. Levina, and E. H. Sargent, *Opt. Express* **14**, 3273 (2006).

[31] S. H. Yen, M. C. Tsai, M. L. Tsai, Y. J. Shen, T. C. Hsu, and Y. K. Kuo, *Applied Physics A: Materials Science & Processing* **97**, 705 (2009).

[32] J. J. Choi, Y.-F. Lim, M. E. B. Santiago-Berrios, M. Oh, B.-R. Hyun, L. Sun, A. C. Bartnik, A. Goedhart, G. G. Malliaras, H. c. D. Abruña, F. W. Wise, and T. Hanrath, *Nano Lett.* **9**, 3749 (2009).

[33] W. J. E. Beek, M. M. Wienk, M. Kemerink, X. Yang, and R. A. J. Janssen, *J. Phys. Chem. B* **109**, 9505 (2005).

[34] F. Verbakel, S. C. J. Meskers, and R. A. J. Janssen, *J. Appl. Phys.* **102**, 083701 (2007).

[35] A. Wood, M. Giersig, M. Hilgendorff, A. Vilas-Campos, L. M. Liz-Marzan, and P. Mulvaney, *Aust. J. Chem.* **56**, 1051 (2003).

[36] A. D. Rakic, A. B. Djurisic, J. M. Elazar, and M. L. Majewski, *Appl. Opt.* **37**, 5271 (1998).

[37] J. M. Caruge, J. E. Halpert, V. Wood, V. Bulovic, and M. G. Bawendi, *Nat. Photon.* **2**, 247 (2008).

[38] R. D. Schaller, M. A. Petruska, and V. I. Klimov, *The Journal of Physical Chemistry B* **107**, 13765 (2003).

[39] B. L. Wehrenberg, C. Wang, and P. Guyot-Sionnest, *The Journal of Physical Chemistry B* **106**, 10634 (2002).

[40] K. A. Bertness, A. Roshko, L. M. Mansfield, T. E. Harvey, and N. A. Sanford, *J. Cryst. Growth* **310**, 3154 (2008).

[41] O. Landre, R. Songmuang, J. Renard, E. Bellet-Amalric, H. Renevier, and B. Daudin, *Appl. Phys. Lett.* **93**, 183109 (2008).

[42] C. Chèze, L. Geelhaar, O. Brandt, W. Weber, H. Riechert, S. Münch, R. Rothemund, S. Reitzenstein, A. Forchel, T. Kehagias, P. Komninou, G. Dimitrakopulos, and T. Karakostas, *Nano Res.* **3**, 528 (2010).

[43] P. Deb, H. Kim, V. Rawat, M. Oliver, S. Kim, M. Marshall, E. Stach, and T. Sands, *Nano Lett.* **5**, 1847 (2005).

[44] H. Sekiguchi, K. Kishino, and A. Kikuchi, *Appl. Phys. Express* **1**, 124002 (2008).

[45] C. T. Foxon, S. V. Novikov, J. L. Hall, R. P. Campion, D. Cherns, I. Griffiths, and S. Khongphetsak, *J. Cryst. Growth* **311**, 3423 (2009).

[46] R. Calarco, R. J. Meijers, R. K. Debnath, T. Stoica, E. Sutter, and H. Lüth, *Nano Lett.* **7**, 2248 (2007).

[47] H.-W. Lin, Y.-J. Lu, H.-Y. Chen, H.-M. Lee, and S. Gwo, *Appl. Phys. Lett.* **97**, 073101 (2010).

[48] L. Cerutti, J. Ristic, S. Fernandez-Garrido, E. Calleja, A. Trampert, K. H. Ploog, S. Lazic, and J. M. Calleja, *Appl. Phys. Lett.* **88**, 213114 (2006).

[49] W. Guo, M. Zhang, A. Banerjee, and P. Bhattacharya, *Nano Lett.* **10**, 3355 (2010).

[50] X. Duan, Y. Huang, R. Agarwal, and C. M. Lieber, *Nature* **421**, 241 (2003).

[51] S. Gradecak, F. Qian, Y. Li, H.-G. Park, and C. M. Lieber, *Appl. Phys. Lett.* **87**, 173111 (2005).

[52] F. Qian, Y. Li, S. Gradecak, H.-G. Park, Y. Dong, Y. Ding, Z. L. Wang, and C. M. Lieber, *Nat Mater* **7**, 701 (2008).

[53] R. F. Oulton, V. J. Sorger, T. Zentgraf, R.-M. Ma, C. Gladden, L. Dai, G. Bartal, and X. Zhang, *Nature* **461**, 629 (2009).

[54] C. J. Barrelet, J. Bao, M. Lonc ar, H.-G. Park, F. Capasso, and C. M. Lieber, *Nano Lett.* **6**, 11 (2005).

[55] H.-G. Park, F. Qian, C. J. Barrelet, and Y. Li, *Appl. Phys. Lett.* **91**, 251115 (2007).

[56] A. V. Maslov and C. Z. Ning, *Appl. Phys. Lett.* **83**, 1237 (2003).

[57] L. Chen and E. Towe, *Appl. Phys. Lett.* **89**, 053125 (2006).

[58] Q. Yang, X. Jiang, X. Guo, Y. Chen, and L. Tong, *Appl. Phys. Lett.* **94**, 101108 (2009).

[59] T. Kouno, K. Kishino, K. Yamano, and A. Kikuchi, *Opt. Express* **17**, 20440 (2009).

[60] A. V. Maslov and C. Z. Ning, *IEEE J. Quant. Electron.* **40**, 1389 (2004).

[61] R. D. M. John D. Joannopoulos, Joshua N. Winn, *Photonic Crystals: Molding the Flow of Light* (Princeton University Press, 1995).

[62] Ö. Duyar, F. Placido, and H. Z. Durusoy, *Journal of Physics D: Applied Physics* **41**, 095307 (2008).

[63] C. Kim, W. J. Kim, A. Stapleton, J.-R. Cao, J. D. O'Brien, and P. D. Dapkus, *J. Opt. Soc. Am. B* **19**, 1777 (2002).

[64] K. Domen, K. Kondo, A. Kuramata, and T. Tanahashi, *Appl. Phys. Lett.* **69**, 94 (1996).

[65] S.-H. Kim and Y.-H. Lee, *IEEE J. Quant. Electron.* **39**, 1081 (2003).

[66] H.-G. Park, S.-H. Kim, S.-H. Kwon, Y.-G. Ju, J.-K. Yang, J.-H. Baek, S.-B. Kim, and Y.-H. Lee, *Science* **305**, 1444 (2004).

[67] P. Mackowiak and W. Nakwaski, *J. Phys. D* **31**, 2479 (1998).

[68] B. Deveaud, *The Physics of Semiconductor Microcavities: From Fundamentals to Nanoscale Devices*, Weinheim (WILEY-VCH, 2007).

[69] H. Deng, H. Haug, and Y. Yamamoto, *Reviews of Modern Physics* **82**, 1489 (2010).

[70] C. Weisbuch, M. Nishioka, A. Ishikawa, and Y. Arakawa, *Physical Review Letters* **69**, 3314 (1992).

[71] G. Khitrova, H. M. Gibbs, F. Jahnke, M. Kira, and S. W. Koch, *Reviews of Modern Physics* **71**, 1591 (1999).

[72] A. Imamoglu, R. J. Ram, S. Pau, and Y. Yamamoto, *Physical Review A* **53**, 4250 (1996).

[73] H. Deng, G. Weihs, D. Snoke, J. Bloch, and Y. Yamamoto, *Proceedings of the National Academy of Sciences* **100**, 15318 (2003).

[74] S. Christopoulos, G. B. H. von Högersthal, A. J. D. Grundy, P. G. Lagoudakis, A. V. Kavokin, J. J. Baumberg, G. Christmann, R. Butté, E. Feltin, J. F. Carlin, and N. Grandjean, *Physical Review Letters* **98**, 126405 (2007).

[75] S. Kena Cohen and S. R. Forrest, *Nat Photon* **4**, 371 (2010).

[76] D. Bajoni, P. Senellart, E. Wertz, I. Sagnes, A. Miard, A. Lemaître, and J. Bloch, *Physical Review Letters* **100**, 047401 (2008).

[77] N. Antoine-Vincent, F. Natali, D. Byrne, A. Vasson, P. Disseix, J. Leymarie, M. Leroux, F. Semond, and J. Massies, *Physical Review B* **68**, 153313 (2003).

[78] R. Butté, G. Christmann, E. Feltin, J. F. Carlin, M. Mosca, M. Ilegems, and N. Grandjean, *Physical Review B* **73**, 033315 (2006).

[79] B. Sermage and G. Fishman, *Physical Review B* **23**, 5107 (1981).

[80] L. K. van Vugt, S. Rühle, P. Ravindran, H. C. Gerritsen, L. Kuipers, and D. Vanmaekelbergh, *Physical Review Letters* **97**, 147401 (2006).

[81] D. G. Lidzey, D. D. C. Bradley, M. S. Skolnick, T. Virgili, S. Walker, and D. M. Whittaker, *Nature* **395**, 53 (1998).

[82] G. Christmann, R. Butté, E. Feltin, J. Carlin, and N. Grandjean, *Appl. Phys. Lett.* **93**, 051102 (2008).

[83] G. Christmann, R. Butté, E. Feltin, A. Mouti, P. A. Stadelmann, A. Castiglia, J.-F. Carlin, and N. Grandjean, *Physical Review B* **77**, 085310 (2008).

[84] T. Böttcher, S. Figge, S. Einfeldt, R. Chierchia, R. Kröger, C. Petter, C. Zellweger, H. J. Bühlmann, M. Dießelberg, D. Rudloff, J. Christen, H. Heinke, P. L. Ryder, M. Ilegems, and D. Hommel, *physica status solidi (c)* **0**, 1846 (2003).

[85] J. B. Schlager, K. A. Bertness, P. T. Blanchard, L. H. Robins, A. Roshko, and N. A. Sanford, *J. Appl. Phys.* **103**, 124309 (2008).

[86] W. Guo, A. Banerjee, M. Zhang, and P. Bhattacharya, *Appl. Phys. Lett.* **98**, 183116 (2011).

[87] K. A. Bertness, A. Roshko, N. A. Sanford, J. M. Barker, and A. V. Davydov, *J. Cryst. Growth* **287**, 522 (2006).

[88] W. Guo, M. Zhang, P. Bhattacharya, and J. Heo, *Nano Lett.* **11**, 1434 (2011).

[89] A. Cavallini, L. Polenta, M. Rossi, T. Stoica, R. Calarco, R. J. Meijers, T. Richter, and H. Lüth, *Nano Lett.* **7**, 2166 (2007).

[90] F. Binet, J. Y. Duboz, J. Off, and F. Scholz, *Physical Review B* **60**, 4715 (1999).

[91] N. Peyghambarian, H. M. Gibbs, J. L. Jewell, A. Antonetti, A. Migus, D. Hulin, and A. Mysyrowicz, *Physical Review Letters* **53**, 2433 (1984).

[92] H. Deng, D. Press, S. Götzinger, G. S. Solomon, R. Hey, K. H. Ploog, and Y. Yamamoto, *Physical Review Letters* **97**, 146402 (2006).

[93] J. Kasprzak, M. Richard, A. Baas, B. Deveaud, R. André, J. P. Poizat, and L. S. Dang, *Physical Review Letters* **100**, 067402 (2008).

[94] V. Y. Prinz, V. A. Seleznev, A. K. Gutakovsky, A. V. Chehovskiy, V. V. Preobrazhenskii, M. A. Putyato, and T. A. Gavrilova, *Physica E: Low-dimensional Systems and Nanostructures* **6**, 828 (2000).

[95] C. Deneke and O. G. Schmidt, *Appl. Phys. Lett.* **85**, 2914 (2004).

[96] T. Kipp, H. Welsch, C. Strelow, C. Heyn, and D. Heitmann, *Physical Review Letters* **96**, 077403 (2006).

[97] M. Hosoda and T. Shigaki, *Appl. Phys. Lett.* **90**, 181107 (2007).

[98] K.-S. Suh, J.-L. Lee, H.-H. Park, C.-H. Kim, J.-j. Lee, and K.-S. Nam, *Materials Science and Engineering: B* **37**, 172 (1996).

[99] Y. Takuma, M. Miyagi, and S. Kawakami, *Appl. Opt.* **20**, 2291 (1981).

[100] Y. H. Cheng and W. G. Lin, *Opt. Lett.* **14**, 1231 (1989).

[101] V. Ramaswamy and P. G. Suchoski, *J. Opt. Soc. Am. A* **1**, 754 (1984).

[102] A. Sakamoto and M. Sugawara, *Photonics Technology Letters, IEEE* **12**, 107 (2000).

[103] H. D. Summers, P. Rees, D. R. Matthews, G. T. Edwards, M. R. Brown, M. Cundin, and J. Dominguez, *Selected Topics in Quantum Electronics, IEEE Journal of* **13**, 1222 (2007).

[104] E. M. Purcell, *Phys. Rev.* **69**, 681 (1946).

[105] H. Yokoyama, *Science* **256**, 66 (1992).

[106] E. F. Schubert, N. E. J. Hunt, M. Micovic, R. J. Malik, D. L. Sivco, A. Y. Cho, and G. J. Zydzik, *Science* **265**, 943 (1994).

[107] E. Hanamura and H. Haug, *Physics Reports* **33**, 209 (1977).